People's Democratic Republic of Algeria

Ministry of Higher Education and Scientific Research

Kasdi Merbah University Ouargla UKMO

THESIS

Faculty of Applied Sciences

Department of Process Engineering

in fulfillment of the requirements of an

LMD Doctorate Degree

Specialty: Energy Process

Submitted by **Miloudi Raouia**

Supervised by

Pr. Zerrouki Djamal

Investigation and Design of Materials for Energy Applications

Chennouf Nasreddine	**Professor**	**Ouargla University**	**Charman**
Zerrouki Djamal	**Professor**	**Ouargla University**	**Supervisor**
Mansouri Khaled	**MCA**	**Ghardaïa University**	**Examiner**
Khane Yasmina	**MCA**	**Ghardaïa University**	**Examiner**
Chaouki Mourad	**MCA**	**Ouargla University**	**Examiner**
Zoubidi Nawal	**MCA**	**Ouargla University**	**Examiner**

2024/2025

REMERCIMENT

The initial thanks are for Allah for everything I have known or didn’t realise that he has hidden for my highest good. Thanks to my mother and the supervisor Zerrouki Djamal, and my bestie Siham Dehmani for the support and the patience to continue my path, asking for your reward from God.

Special thanks to the supervisor, The Professor Zerrouki Djamal, the director of DIRS laboratory, who never hesitates to share his knowledge and expertise, ideas, and time, and for implanting in me the seed of ambition and encouraging the prosperous displine, thank you for standing in laboratory for a numerous time to helpe me in my exprements, thank you for been my supervisor, I have learned a lot things from you.

Deepest gratitude to the review committee that accepted to evaluate my thesis, distinct thanks to Professor Chennouf Nasreddine for accepting to be the committee president, and for the care that he gave me.

I sincerely appreciate the foreign jury, Dr. Mansouri Khaled and Dr.Khane Yasmina, for accepting to be part of the committee and enduring the travel to be present.

Distinct thanks to my favorite professor, Dr. Chaouki Moured, for being my examiner, and a particular thanks to Dr. Zoubidi Nawal for accepting to be a reviewer.

I would like to thank the scientific community for helping me finish my thesis, the process engineering chiefs' department, Dr. Tabchouch, and Pr. Manouche for the countless facilities they offer, and for the welcome they have.

Thanks to the civil engineering department, especially Mr. Kchired and Dr. Hachem, for giving me entry permission to the beton laboratory and for the similes that never hesitate to share.

I am most grateful to the professors from Tunisia for their help and knowledge.

From Malaysia, my sincerest thanks to the professors for the facilities that were given to me and the very warm welcome, never forget the laboratories responsible for mechanical and science.

Thanks a ton to my friends Soumia, Slah, Imen, and Bilal, as well as the members of the DIRS laboratory, Abdslem, Sara, and Dhiya.

ABSTRACT

Thermal regulating microparticles were successfully fabricated, and three classes of polymer were selected, alginate, polyvinyl alcohol, and sheep wool powder, depending on their bio-source and non-toxic behavior. In the purpose of ascertaining the morphology efficiency in the preservation of the phase change material, different methodology effectuates, the encapsulation technique through a microfluidic system accomplished to produce mononuclear capsules of Alginate-PCM, in situ polymerization by conventional emulsion executed to produce microspheres alginate/PCM and PVA/PCM, the shape stabilized technique carried out to produce homogenous matrix wool-PVA-alginate/PCM, wool-alginate/PCM.

The enhancement of thermal stability by the incorporation of highly stable materials is achieved through the addition of calcium carbonate and calcium silicate inside the alginate polymer, while the titanium dioxide nanoparticles are integrated successfully into the PVA polymer.

All the performed samples were investigated for their compatibility, thermal stability, energetic efficiency, and thermal conductivity.

Keywords: PCM, Encapsulation, thermal stability

ملخص

تم تصنيع جسيمات دقيقة مُنظِّمة للحرارة بنجاح، وتم اختيار ثلاثة أنواع من البوليمرات، بناءً على مصدرها الحيوي وسلوكها غير السام: الألجينات، وكحول البولي فينيل، ومسحوق صوف الأغنام. ولغرض التأكد من كفاءة مورفولوجيا المواد في حفظ مادة تغير الطور، تم تطبيق منهجيات مختلفة، منها تقنية التغليف باستخدام نظام ميكروفلويدي لإنتاج كبسولات أحادية النواة من AlG/PCM والبلمرة في الموقع باستخدام المستحلب التقليدي لإنتاج كريات دقيقة من ALG/PCM و PVA/ PCM.تقنية تثبيت الشكل لإنتاج مصفوفة صوف متجانسة من wool-PVA-alginate/PCM، wool-alginate/PCM .

ويتم تعزيز الاستقرار الحراري من خلال دمج مواد عالية الاستقرار من خلال إضافة كربونات الكالسيوم وسيليكات الكالسيوم داخل بوليمر الألجينات، بينما يتم دمج جسيمات ثاني أكسيد التيتانيوم النانوية بنجاح في بوليمر الكحول فينيل . تم فحص جميع العينات المُجراة من حيث التوافق، والاستقرار الحراري، والكفاءة الطاقية، والتوصيل الحراري.

الكلمات المفتاحية : مادة تغير الطور، التغليف، الاستقرار الحراري.

LIST OF FIGURES

LIST OF TABLES

Table of Contents

INTRODUCTION

Fossil fuels are essential as a source of energy, but due to their negative effect on the environment, especially climate change, a search for alternatives is required. Renewable energy sources are effective substitutes, particularly natural sources such as sunlight, wind, rain, or regenerated biowaste material. One of the innovative solutions is to reutilize the energy that is already used. Thermal energy storage (TES) technologies have the potential to make better use of existing heat through waste heat recovery, reducing losses, and shifting.

A Thermal energy store is a means of storing and releasing renewable heat until it is required.

Phase Change Materials (PCMs) are a latent heat thermal energy system that exploits the latent heat associated with a phase transition. Latent heat energy storage is an attractive approach because it provides high energy storage capacity despite requiring a small volume.

In this regard, many materials can be identified as phase change materials based on their transition. Solid-liquid phase change materials are widely used depending on the beneficial energy feedback compared to the extent to which they are exploited.

The drawback of the solid-liquid PCM is the leakage of the material during the transition phase, which is combined with heat absorption. The encapsulation method is a promising technology used to sequester the PCM and prevent it from leaking during the occurrence of the PCM cycle. This technology not only enhanced PCM preservation but also provided a protection barrier in the case of harmful agents. Extensive research was carried out in this field to develop a suitably designed encapsulation for specific applications. Organic PCMs are widely used for their inherent properties, and the large temperature range and diversity of their absorbed capacity, the low thermal conductivity, and the instability issues pose a hurdle for their selection.

The thermal properties enhancement is the optimum solution to regulate the PCM instability; nevertheless, the conductivity behavior. The integration of highly stable particles is one of the promising solutions not only for the PCM but also for incorporating in shallow incorporation. In general, the assortment of optimum PCM preservatives is challenging according to the numerous standard qualifications, but still origin an indispensable criterion.

Alginate is a biomaterial extracted from algae. It is known to be non-toxic, inert, and, most importantly, does not require a complex procedure for its use, unlike many other materials, various studies used alginate differently, (Tian et al., 2020) used alginate as a shell for PCM

capsules, (H. Wang et al., 2022) integrated the alginate micro-encapsulating rejuvenator to enhance the self-healing of asphalt, and widely used as bio shell for a medical purpose (Cao et al., 2024) fabricated complex of alginate- $CaCO_3$ for encapsulating lactoferrin.

Polyvinyl alcohol is a synthetic material that has crucial properties and is a target of many researchers, Weil et al. (Wei & Yang, 2023) fabricated a self-healing PVA polymer using boron nitride polydopamine, (J. Li et al., 2013) encapsulated the PVA-PCM through the spinning method, (Tomar et al., 2014) studied the PVA as a degradable agent, (Surkatti et al., 2024) Demonstrate the effectiveness of PVA in wastewater treatment, while improving its properties to eliminate harmful chemical compounds (Yuan et al., 2016).

This study is an attempt to design PCM microparticles using different techniques, which are presented in five chapters described below.

The first chapter presents an acknowledgment about the energy storage method, the different type of PCM and their classification, the shells that are used to enhance the phase change material stability, and the proper mechanisms to design impeccable capsules.

The second chapter focuses on the fabrication of microparticle alginate-PCM by an ionic crosslinking method using calcium chloride. In this regard, two types of capsules were designed: mononuclear capsules through a microfluidic system and microspheres using the conventional technique of emulsion. The double shell technique was used to enhance the stability and improve the PCM preservation, while calcium carbonate and calcium silicate were used for the purpose of intensifying the stability, depending to their high stability.

In the third chapter, a PVA-PCM microsphere was fabrication through the in situ polymerization method using the technique of monodispersed microspheres, driven by boric acid as a crosslinker. The thermal stability of the pristine material was enhanced by the incorporation of the titanium dioxide nanoparticles with different fractions.

The fourth chapter displays the fabrication of microparticles of wool powder-PCM through the shape-stabilized method. at this point, a chemical-mechanical procedure is carried out to convert the raw material (sheep wool) to powder. An improvement of wool-PCM was accomplished through the integration of the saturated wool-PCM into a polymeric matrix. two types of polymers were used: alginate and the combined mixture PVA-Alginate.

The fifth chapter was a study of the thermal gain from the preformed microparticles for this purpose, the samples were integrated into separated gypsum matrices depending on the studied case and subjected to heat flux to trigger the transition behavior of the encapsulated

PCM, two trajectories followed, in the laboratory to simulate the performance into a controlled environment, and in outside in reel environment to investigate the reel performance on harsh conditions.

Chapter 1. BIBLIOGRAPHY

1.1 Energy storage methods

These energy storage methods are crucial for improving efficiency, enabling energy conservation, and supporting renewable energy integration. The different forms of energy that can be stored include mechanical energy, such as that stored in springs or rotating flywheels; electrical energy, which can be stored in batteries, capacitors, or superconducting magnetic systems; and thermal energy, which is stored in various materials through heating or phase changes, such as in thermal storage systems that utilize phase change materials (PCMs).

1.1.1 Mechanical energy storage

Mechanical systems for energy storage can store energy in gravitational form, storage, hydropower, compressed air, and flywheels. These technologies can be used for large-scale service energy storage, while flywheels are more suitable for transitional storage. Storage is carried out when inexpensive off-peak power is available, e.g., at night or on weekends. The stored energy is delivered when power is needed because of an insufficient supply from the base-load plant.

1.1.2 Electrical storage Energy storage

Storing electrical energy through batteries is a viable option. By connecting the battery to a source of DC. When the battery is discharged, the chemical energy is converted back into electrical energy.

Potential applications for batteries include utilizing off-peak power, load leveling, and storing electrical energy generated by wind turbines or photovoltaic systems. The most common types of storage batteries are lead-acid, nickel-cadmium batteries, and lithium batteries.

1.1.3 Thermochemical energy storage

Thermochemical systems depend on the energy that is absorbed and released when molecular bonds are broken and reformed during a completely reversible chemical reaction. In this context, the amount of heat stored is determined by the quantity of storage material, the endothermic heat of the reaction, and the degree of conversion.

1.1.4 Thermal energy storage

Thermal energy storage can be stored as a change in the internal energy of a material through sensible heat, latent heat, thermochemical methods, or a combination of these.

1.1.4.1 Sensible heat storage

In sensible heat storage (SHS), thermal energy is stored by increasing the temperature of a solid or liquid. An SHS system takes advantage of the material's heat capacity and the temperature change that occurs during the charging and discharging processes. The amount of heat stored depends on the specific heat of the medium, the temperature change, and the quantity of storage material used.

1.1.4.2 Latent heat storage.

Latent heat storage (LHS) involves the absorption or release of heat when a storage material changes its phase, such as from solid to liquid, liquid to gas, or vice versa. Latent heat thermal energy storage is particularly attractive due to its high energy storage density and ability to maintain a constant temperature during the phase change material's phase transition (PCM). The phase changes can occur in solid-solid, solid-liquid, solid-gas, or liquid–gas.

1.2 Phase change materials (PCM)

Latent heat storage materials are substances that store thermal energy during phase changes, specifically when a material transitions from solid to liquid or from liquid to solid. This state change is referred to as a phase change. Initially, these solid-liquid phase change materials (PCMs) behave as storage materials by increasing in temperature through heat absorption. However, unlike conventional (sensible) storage materials, PCMs absorb and release heat at approximately constant temperature.

1.2.1 Phase change material properties

To be effective as latent heat storage materials, certain desirable thermodynamic, kinetic, and chemical properties are essential. Additionally, economic factors and the availability of these materials must be considered. The phase change material (PCM) selected for designing thermal storage systems should possess the following key thermophysical, kinetic, and chemical properties.

1.2.1.1 Thermal properties

When selecting a Phase Change Material (PCM) for a specific application, it is essential to consider several factors:

The Phase-Transition Temperature, the operating temperature for heating or cooling, should align with the PCM's transition temperature.

Latent Heat of Transition, a higher latent heat is preferable, particularly on a volumetric basis, as this helps minimize the physical size of the energy storage system.

Thermal Conductivity, good thermal conductivity is important as it enhances the charging and discharging processes of the energy storage.

1.2.1.2 Physical properties

The ideal conditions for phase equilibrium include favorable properties such as high density, minimal volume change, and low vapor pressure. Maintaining phase stability during freezing and melting is crucial for effective heat storage. A high density is desirable as it allows for the use of smaller storage containers. Additionally, small volume changes during phase transformation and low vapor pressure at operating temperatures help mitigate containment challenges.

1.2.1.3 Chemical properties

Long-term chemical stability. Compatibility with materials of construction. No toxicity. No fire hazard. The degradation of PCM quality can be caused by loss of water of hydration, chemical corrosion and decomposition, or incompatibility and interaction with materials of construction. PCMs should be non-toxic, non-flammable, and non-explosive for safety.

1.2.1.4 Kinetic properties

No supercooling is essential for achieving a sufficient crystallization rate. Supercooling has been a problematic issue in PCM development, especially for salt hydrates. If supercooling exceeds a few degrees, it can interfere with effective heat exchange.

1.3 Classification of PCMs

There are four types of phase change materials (PCMs): organic, inorganic, metallic, and eutectic. When selecting a material to be used as a PCM, the most important properties to consider are its high thermal energy storage capacity, melting temperature, heat of fusion, thermal conductivity, density, and the source of the material.

1.3.1 Organic solid-liquid PCMs

This type of phase change material (PCM) is classified into two categories: paraffin and non-paraffin. The main advantages of these materials include their chemical and thermal stability, non-corrosiveness, recyclability, and lack of subcooling. However, there are drawbacks to using organic PCMs, such as their flammability, low thermal conductivity, and a phase change enthalpy that is lower than that of other types of PCMs. The most commonly used organic PCMs are paraffin and fatty acids.

1.3.1.1 Paraffin phase change material

Paraffins mainly consist of straight-chain alkanes, represented by the formula CH3–(CH2)n–CH3. The crystallization of these compounds releases a significant amount of latent heat. Both the melting point and the latent heat of fusion increase with chain length. Due to their availability over a wide temperature range, paraffins qualify as effective materials for latent heat storage. However, for cost considerations, only technical-grade paraffins are typically used as phase change materials (PCMs) in latent heat storage systems. Paraffins are safe, reliable, predictable, relatively inexpensive, and non-corrosive. They are chemically inert and stable at high temperatures, and they possess good nucleating properties. Despite their advantages, paraffins have some drawbacks, including low thermal conductivity, incompatibility with plastic containers, and moderate flammability.

1.3.1.1 Non-paraffin PCMs, Fatty acids

Non-paraffin organics are a diverse category that includes fatty acids, esters, alcohols, and glycols. Some of these compounds possess properties suitable for latent heat storage. Fatty acids are a type of carboxylic acid characterized by a long hydrocarbon chain containing carbon atoms (ranging from 10 to 30) and hydrogen atoms, with the general formula CH3(CH2)2nCOOH. These acids feature a carboxyl group (COOH) at the end of the chain. Thanks to this functional group, fatty acid-based phase change materials (PCMs) are non-toxic,

have low corrosion activity, and exhibit both chemical and thermal stability. Additionally, they can be derived from natural products instead of fossil fuel sources. Fatty acids can be either saturated or unsaturated. Unsaturated fatty acids tend to have lower melting points because their molecular structure allows for closer intermolecular interactions. They can also exist in cis and trans configurations, with the intermolecular interactions in these configurations being weaker than those found in saturated fatty acids.

1.3.2 Inorganic PCM

They are classified into three categories: hydrates salt, salts, and metals. These materials generally have fewer advantages compared to organics. While they possess higher phase change enthalpy and their heats of fusion do not degrade with cycling, they also have significant drawbacks. These include issues such as corrosion, subcooling, phase segregation, lack of thermal stability, and phase separation.

1.3.3 Metals

This category includes low-melting metals and their eutectics. These metals have high thermal conductivity, good electrical conductivity, low vapor pressure, and low heat of fusion per unit weight, but high heat of fusion per unit volume.

1.3.4 The eutectics

Eutectic mixtures are formed from combinations of chemical compounds or elements that share a single chemical composition and solidify at a lower temperature than any other mixture made from the same components. These combinations can be organic–organic, inorganic–inorganic, or inorganic-organic. Various eutectic mixtures are available for use as phase change materials (PCMs), making them ideal for cooling applications.

1.4 Microencapsulation

Microencapsulation is a process in which particles are surrounded by a coating material or integrated into a uniform or varied matrix. The core can be in either a liquid or solid state, while the shell acts as a protective container, shielding the core from external influences. Microcapsules can come in various shapes, ranging from regular geometries to irregular forms. This technique is highly effective for preserving substances and provides a physical barrier between the core and the shell material.

1.4.1 Types of shell

A variety of different polymers, both natural and synthetic, can be used as wall materials in microencapsulation to control the release of substances under specific conditions. The materials used for the shell coating must meet certain requirements. The polymer should be able to form a thin film that is cohesive with the core material, tasteless, pliable, and stable. It should also be chemically compatible and non-reactive with the core material, as well as soluble in aqueous media or solvents. Additionally, the polymer needs to provide desired coating properties, such as strength, flexibility, impermeability, optical properties, and stability. The film thickness can vary significantly based on the surface area of the material being coated and other physical characteristics of the system. Furthermore, the shell coating material should be non-hygroscopic, have medium to low viscosity, and be cost-effective.

1.4.2 Morphology of PCM

The core/shell system is crucial in the fabrication of microcapsules. The shell's primary function is to protect the core, while the core's role is to contain the active material. This process depends on the core material and the method used for the fabrication of the shell. The types of capsules can be found as:

1. Mononuclear (Core/Shell): A single core is wrapped in a continuous shell material.

2. Polynuclear: Multiple cores coated with a continuous shell material.

3. Matrix Encapsulation: The core material is homogeneously distributed throughout the shell material.

4. Multi-Film: A continuous core is coated with multiple layers of continuous shell material.

1.5 Encapsulation method

1.5.1 Physical Methods

Physical methods like spray cooling, spray drying, and fluidized bed processes cannot produce smaller microcapsules.

1.5.2 Chemical Methods

Interfacial polymerization, in situ polymerization, complex coacervation, phase separation, and suspension-like polymerization are methods that can produce smaller encapsulated PCM particles.

1.5.2.1 In situ polymerization

The process typically involves combining two immiscible liquids without adding any reactants to the core material. Instead, all the polymerization occurs in the continuous phase, which distinguishes it from interfacial polymerization which takes place between two phases. The process generally begins by creating an oil-in-water (O/W) emulsion. Next, a prepolymer mixture is prepared and added to the emulsion to encapsulate the core material particles. Finally, the process concludes with washing and drying the resulting sample.) emulsion. Then, a prepolymer mixture is prepared and added to the emulsion to encapsulate the core material particles. The process concludes with washing and drying the resulting sample.

1.5.2.2 Interfacial polycondensation

An in situ technique called interfacial polycondensation is used to create a polymer microcapsule wall at the interface of two phases, each of which contains appropriate reaction monomers initially, the organic core material dissolves a multifunctional monomer. After that, this mixture is distributed in an aqueous phase containing a mix of protective colloid stabilizers and emulsifiers. To aid in the creation of a polymer shell, the mixture of monomers is then introduced to the aqueous phase.

1.5.2.3 Suspension polymerization

Several crucial steps are involved in the suspension polymerization process. Initially, the organic phase dissolves the polymer monomer. The monomer molecules separate and precipitate from the core materials after the production of an emulsion. Solid shells are created as a result.

1.5.2.4 Complex coacervation

Complex coacervation includes a response between two or more sorts of polymer materials with oppositely charged crosslinks to copolymer shells. The common preparation comprises three stages carried out beneath ceaseless disturbance as follows. To begin with, coating fabric is dispersed in water to create a stage division coacervation, and after that, a center fabric is

included in the arrangement to deliver O/W emulsion. The moment stage involves adding another colloid arrangement charged with oppositely electricity into the O/W emulsion, and after that altering the pH number of the arrangement appropriately. The third organize wraps it off with the cooling down of the mixture, microencapsulation, and collecting of the MEPCM. The most restrictive of this approach is the trouble in scaling up the method.

1.5.2.5 Sol-gel method

The term “sol-gel” is a truncation of “solution-gelling” and signifies a preparation by which, to a great extent, inorganic materials are synthesized. The method is based on a rule whereby an arrangement experiences a move to a gel characterized by a boundless three-dimensional arranged structure spreading consistently throughout the fluid medium.

1.5.2.6 Solvent extraction/evaporation method

The solvent extraction/evaporation method can be used to encapsulate inorganic PCMs by first incorporating the bioactive compound, then forming microdroplets, removing the solvent, and finally harvesting and drying the particles.

1.6 Applications of MEPCM

Applications for microencapsulated phase change materials in the textile industry have been developed and are still expanding. MEPCM textile materials have been the subject of numerous studies. In Constructing To improve the thermal comfort of lightweight buildings and save energy, phase change materials have been used in construction.

1.7 Characterization of the prepared particles

1.7.1 Morphology characterization

The sizes and the morphology of the prepared particles were investigated using the photography apparatus. A field emission scanning electron microscope coupled with an energy-dispersive X-ray (EDX) was used to investigate the surface morphology and the cross-section. The SEM images were obtained with an acceleration voltage of 10 to 15 kV and with high-resolution image quality.

1.7.2 Fourier-transform infrared (ATR-FTIR) spectroscopy

The FTIR spectra were obtained using an Agilent Cary 630 spectrophotometer equipped with a diamond crystal iATR reflectance cell and a DTGS scanning over the wavenumber range of 4000–400 cm-1 at a resolution of 4 cm^{-1}. The beads were applied to the surface of the crystal and then pressed into the crystal head. A background scan of ambient air was run before each scan. Scans were recorded with the spectroscopic software Spectrum (Micro Lab). Spectra were background corrected for ambient air. The software Spekwin32 was used for spectrum analysis.

1.7.3 Differential scanning calorimetry (DSC)

Dynamic DSC scans were performed using a TA Instruments Q100 differential scanning calorimeter, and all measurements were carried out in a nitrogen atmosphere at a heating or cooling rate of 10 ℃ / min with the weight of the specimen being about 6 mg. The heating scan was carried out from 10 ℃ to 50 ℃

1.7.4 Thermogravimetric analysis (TGA)

TGA was performed on a TA Instruments Q50 thermal gravimetric analyzer under a nitrogen atmosphere. The specimen with a mass of about 10 mg was placed in an aluminum crucible and then ramped from room temperature up to about 500 ℃ at a heating rate of 10 ℃ / min.

1.7.5 Thermal acquisition

The temperature fluctuation of the internal and external faces was recorded by using K-type temperature sensors with an accuracy of -/+ 0.1°C. The measurement data was continually recorded using a data logger (PCT T 1200 model).

Chapter 2. ALGINATE MATRIX

Alginates are linear copolymers composed of (1 → 4)-linked α-L-guluronic (G) and β-D-mannuronic (M) residues of varying sequences depending on the organism and tissue from which it is isolated. The chains are composed of a random sequence of M- and G-blocks that are interspersed with regions of alternating MG blocks whose monad, diad, and triad frequencies are known. Alginates, in general, are stiff molecules due to the rigid six-membered sugar rings and restricted rotation around the glycosidic linkage. Electrostatic repulsion between the charged groups on the polymer chain further contributes to the rigidity of the chains. Chain stiffness is known to depend not only on ionic strength but also on alginate composition, increasing in the order MG < MM < GG. (Hecht & Srebnik, 2016).

2.1 Strategy of Sample Design

The samples were divided into two main categories: Alginate Capsules and modified Alginate Capsules. Alginate capsules were optimized by adding 30% mineral particles. In this experiment, two trajectories were applied to obtain different capsule structures: microcapsules generated by the microfluidic technique and microspheres generated by conventional oil-water emulsion (Figure 1). To produce uniform samples, an alginate solution of 2% (w/v) was added as a continuous phase in an alginate bead, and for the modified particles 0.64 % of (w/v) sodium carbonate (Na_2CO_3) and sodium silicate (Na_2SiO_3) were added separately to the first prepared solution (2% of alginate), to acquire three continuous phases. Parallel, semi-synthetic glyceride wax was fixed as the core; PCM. For further use and to better understand the effects of the incorporated minerals, Shells without PCM, hybrid microspheres at 1% and 1.5 % were fabricated.

2.1.1 Elaboration of Microcapsules Alginate

A microfluidic system was used to obtain capsules with a continuous inner phase and an outer shell surrounding the interior material with specific characteristics controlling the proportion of shell/core fraction, diameter, and fabrication rate. Different Alginate/PCM ratios were selected. The fabrication process consists of three main steps:

- First shell fabrication:

The alginate/PCM droplets were modeled by extrusion of two immiscible solutions previously placed into separate syringes through the coaxial device, as illustrated in (Figure 1); the inner

Figure 1. Scheme illustrates the systems used in the fabrication process.

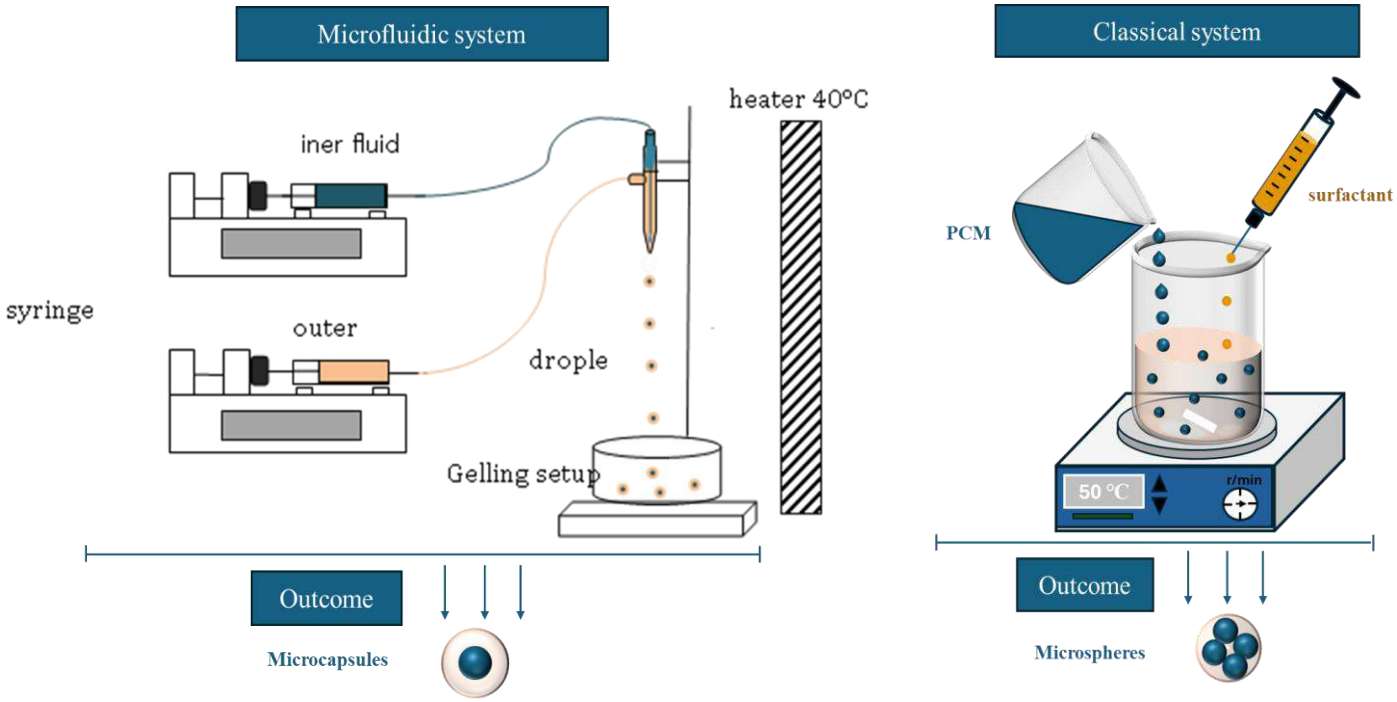

solution was injected inside the central needle, designed to have a diameter of 1 mm, while the second solution was extruded into the outer needle, which was 2 mm, where the flow rates of the solutions were controlled with a pump syringe. The droplets were collected at a height of 10 cm in a gelling bath of calcium chloride. To ensure the fluidity of PCM, a heat plaque was integrated to adjust the process temperature to 40°C. The generated droplets were induced at a gradient gelling batch: 30 min at 2.5% (w/v), 5% for 30 min, and finally into a 12 % $CaCl_2$ solution for at least 30 min, as shown in (Figure 2).

- The second shell assembly:

At the end of the gelation process, the formed microcapsules were collected by filtration and dipped into their continuous or heterogeneous solution for 1 min. The framework of the double-shell capsules is shown in (Figure 3). The immersed microcapsules were transferred to the container containing the calcium chloride gelling agent, following the same order of concentration as described above for the first shell.

Figure 2. the procedure followed in the fabrication process

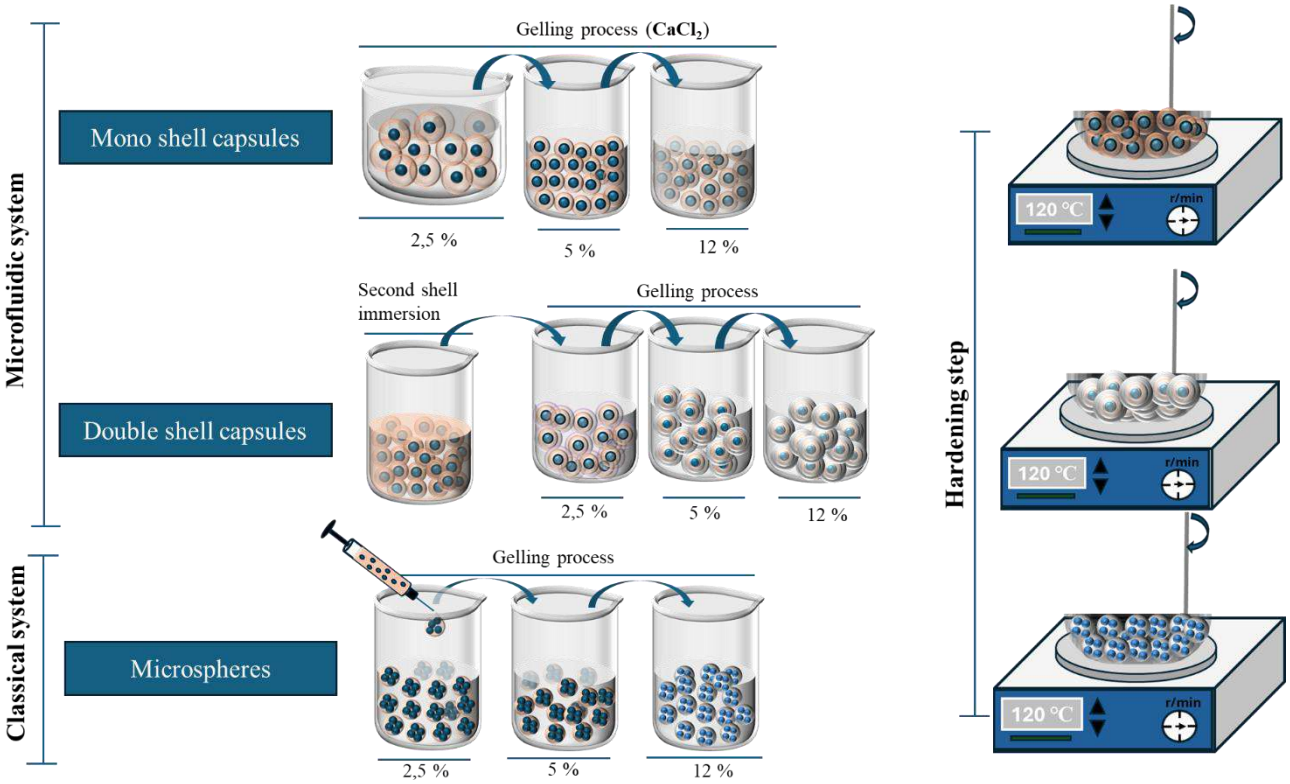

- The hardening step:

All the prepared microcapsules were consolidated using a heat stainless steel plate at 120 °C under continuous rolling to guarantee identical heat treatment distribution. This process takes about 15 minutes to complete and evaporates the excess water inside the formed samples.

2.1.2 Elaboration of Microspheres Alginate

The major contrast factor between the two methods is the nucleation of the PCM in the first-designed microcapsules and the dispersion in the second; otherwise, the same procedure was effectuated. Emulsion (O/W) was prepared by dispersion of the melted oil in heated alginate solution under continuous stirring, The PCM/Alginate microspheres were stabilized by incorporating the non-ionic emulsifier (Figure 1). The emulsion of 60/40 % (w/w) alginate/PCM was extruded using a syringe into a $CaCl_2$ container. All the procedures are similar to Microcapsules, from the aging step to the second shell assembly and heat treatment.

Figure 3. Diagram of the fabricated samples.

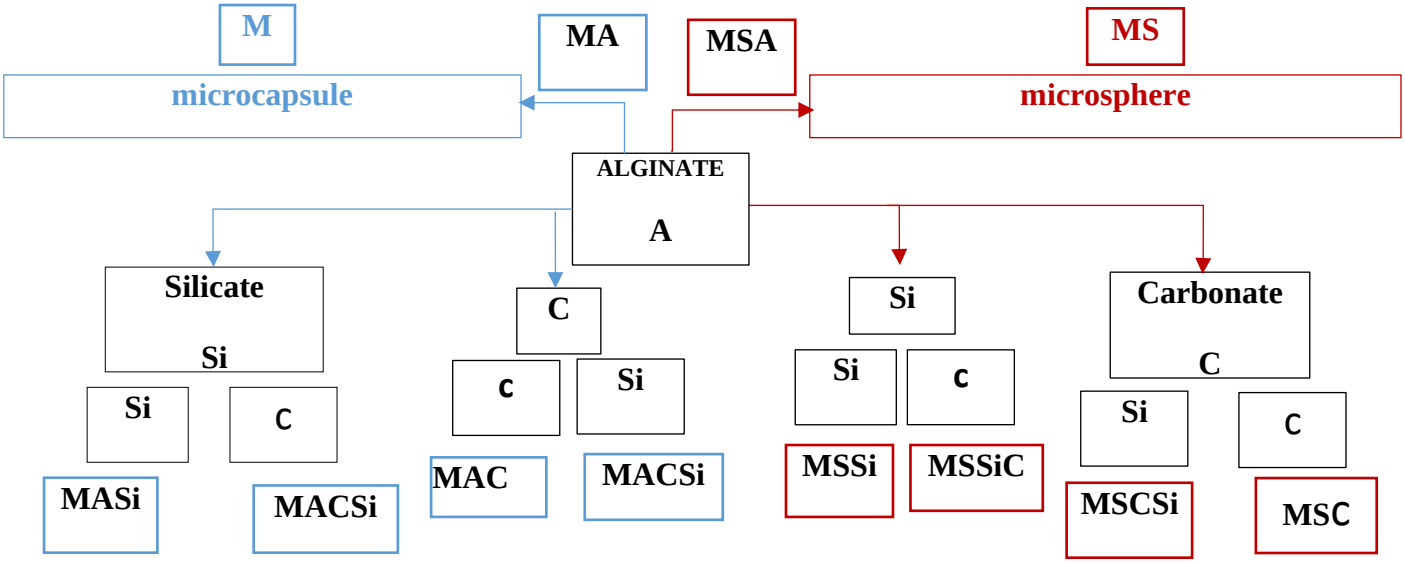

2.1 Morphological Aspect

The prepared microcapsules were investigated using a photograph camera and microscopy. For deep structure understanding, a scanning electron morphology was carried out. In the first instant after the droplet was immersed in a gelling container comprising surfactant as recommended to obtain a homogeneous shape (Figure 4, a(b), c) the forces between the viscous surface tension and the drag forces compensate and promote a deep penetration, (Davarcı et al., 2017) (Chan, 2011)The superficial transparent film was fabricated and became white and dense with aging time.

This phenomenon demonstrates the ionic crosslinking of alginate with calcium chloride and precisely with the calcium cation (Figure 4, a(c)). The hydrogel bead obtained from the initial coating was fragile and soggy (Figure 4(a)), It is worth noticing that the capsule shearing indicates the presence of liquid inside the bead (case of microcapsule). As a result of dipping the bead in a continuous solution, the second shell gradient emerges onto the surface of the first coat and expands with the soaking time. Indeed, the new layer involves a crosslinking step to obtain an ultimate microcapsule with an intense white color and a rigid, dense form (Figure 4, a (d)).

Good mechanical and thermal properties require a transition from hydrogel to glass form. The intensification is based on evaporating the excess water entrapped inside the gel under heat

treatment. The overview emphasizes shrinkage and alters the color from white to brown, identical to the original color of dissolved alginate before the final solid state (Figure 4, a(e)).

Under microscale, the samples are intact (Figure 4, c) with different surfaces, and the silicate as the outer shell is rough and heterogeneous, as confirmed by intense white agglomeration (Figure 4, b). The sample that exposed the carbonate as a surface is rough and heterogeneous

*Figure 4.**a**; (a) microscopy image in the early stage of crosslinking 1st, (b) microscopy image of mono shell microcapsule, (c) transparency photo of; 1- MASiSi 2-MACC 3-MACSi (left to right), (d) hydrogel bead image of MASiSi, (e) consolidate image of MASiSi. **b;** SEM image of microcapsule surface. **c;** microcapsule SEM image. **d;** double shell alginate microcapsule. **e;** Sem image of MASiSi. **f;** image of MACSi.*

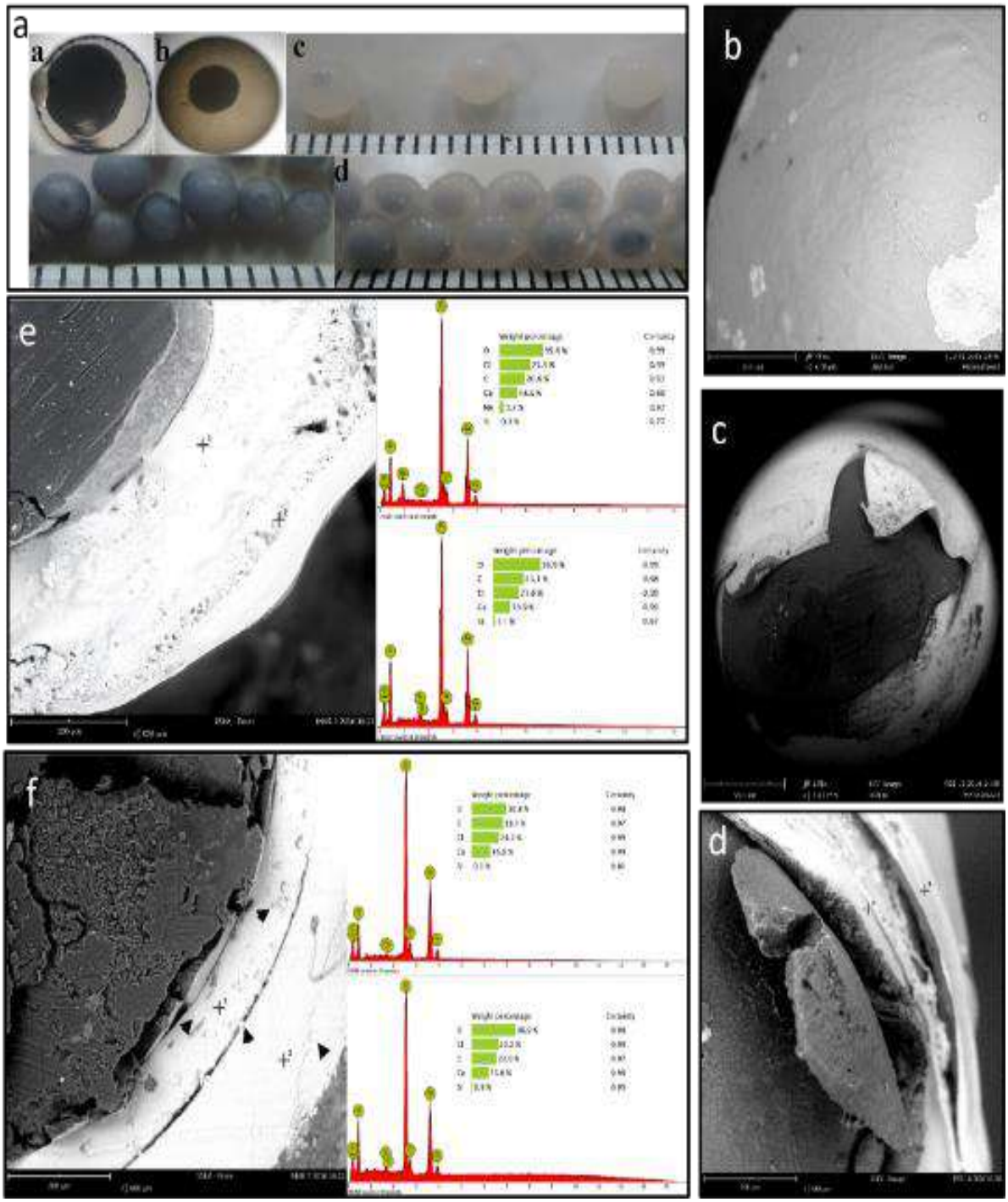

due to the distribution of small spheres on the surface, also inside the polymer, as shown in Figure 4, f).

To visualize the bead structure and confirm the PCM encapsulation inside the polymer shell, a cross-section of the prepared capsules is required. The (Figure 4, d) shows two superposed sectors slightly separated, and at the same time, the (Figure 4, e) presents a double shell without space between them. This phenomenon is ascribed to the heat treatment that occurs from outside to inside so the outer shell was induced directly, elucidating rapid phase transition, especially since the inner shell was rigid compared to the superficial, which highlights the dilating crosslinking time of the interior coat yielding partially stiff state hinders the interconnect to the new shell (second shell).

2.2 Compatibility study of polymer PCM samples

The chemical investigation of the performed samples was carried out using the FTIR method. To conceive the influence of mineral incorporation and the alteration made by the PCM encapsulation, shells and microcapsules were analyzed to give an overview of the fabrication process.

The (Figure 5, a) Display the profile of PCM, the alginate shell, and the microcapsule alginate MA. It is obvious that the microcapsule preserves the peaks of both constituents, which accentuate the compatibility of the shell presented in alginate and the core in PCM.

From (Figure 5, b), a broad band between 3710 cm^{-1} and 2982 cm^{-1} related to the stretching vibration of hydrogen bond of the hydroxyl groups OH, 2932 cm^{-1} is the stretching vibration of CH bonds on the six-membered ring attributed to the eggshell structure formed by Ca^{2+} crosslinking with the GG structure which highlited in alginate shell profile SA in (Figure 5, a). Moreover, bonds at 1014 cm^{-1} are attributed to a stretching vibration of C-O-C, β-1,4-glycosidic bond connecting two fragments (Fu et al., 2019), 1073 cm^{-1} corresponds to C-O stretching, 1592 cm^{-1} and 1420 cm^{-1} are attributed to symmetric and asymmetric COO^- stretching vibration (Barbut & Harper, n.d.-a). 812 cm^{-1} indicates M block residues (Q. Fan et al., n.d.), particularly

the sulfate group of the galactan unit as mentioned by (Kavoosi et al., 2018), 935 cm^{-1}

Figure 5. FTIR, a. MA microcapsule, b. comparison of different microcapsules, comparison of different shell.

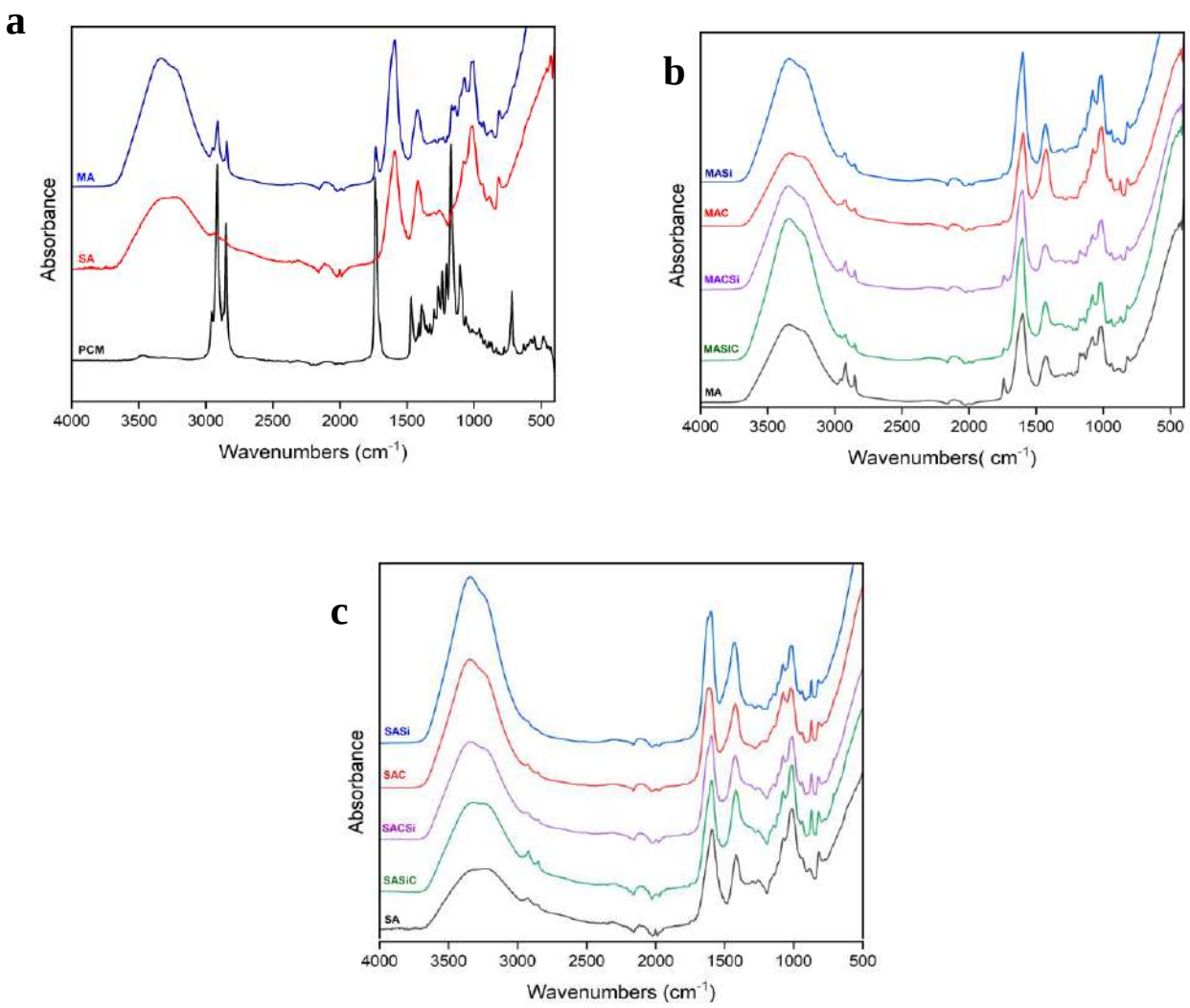

corresponding to C-O stretching vibration of 3,6-anhydro galactose (C-O-SO_3) on C4 of galactose (Barbut & Harper, n.d.-b). The peaks around 2849 $cm^{-1,}$ 2914 $cm^{-1,}$ 1741 $cm^{-1,}$ 1138 $cm^{-1,}$ and cm^{-1} appear in some curves ascribed to PCM existence as observed in PCM spectra in (Figure 5a). In the fingerprint of MAC a small sharp peak at 875 cm^{-1} out-plane deformation mode of CO_3^{2-} in calcite crystal, reveals the growth of carbonate (X. Li et al., 2009a) (Xie et al., 2010). It is worth noting in (Figure 5c) that tiny peaks at 711 cm^{-1} and 775 cm^{-1} appear in the spectrum shell of SAC and SASiC, SACSi, respectively, related to the in-plane deformation mode of CO_3^{2-} in calcite crystal (X. Li et al., 2009b) and in-plane deformation mode of CO_3^{2-} in vaterite crystal (Cao et al., 2024), despite disappearing from MAC, and all microcapsule curves contain carbonate particles.

The peaks appearing in the MASi sample at 891 cm^{-1} are associated with Si-C vibration, 961 cm^{-1} corresponds to Si-OH bending vibrations, and 1110 cm^{-1} is attributed to Si-O-Si

asymmetric stretching vibrations. these absorbances indicate the formation of calcium silicate particles, these vibrations are less intense in MASiC and MACSi. (Kusuktham et al., 2014) (Krautwurst et al., 2018) (Islan et al., 2015)

In the shell spectrum (Figure 5, c), all the bonds rise to higher frequencies in microcapsule spectra, indicating more interaction with the enhanced crosslinking time; the shell particles had a lower crosslinking ratio compared to the PCM/shell samples.

2.3 Thermal behavior and stability of the preformed specimen

The thermal stability of the capsules was evaluated using thermogravimetric analysis, under azote gas at a rate of 10 °C/min, (Figure 6) illustrating the alginate microcapsule degradation mechanism. The microcapsule behavior includes five phases, the first decomposition step of

Figure 6. TGA of a. microcapsule samples, b. microsphere samples.

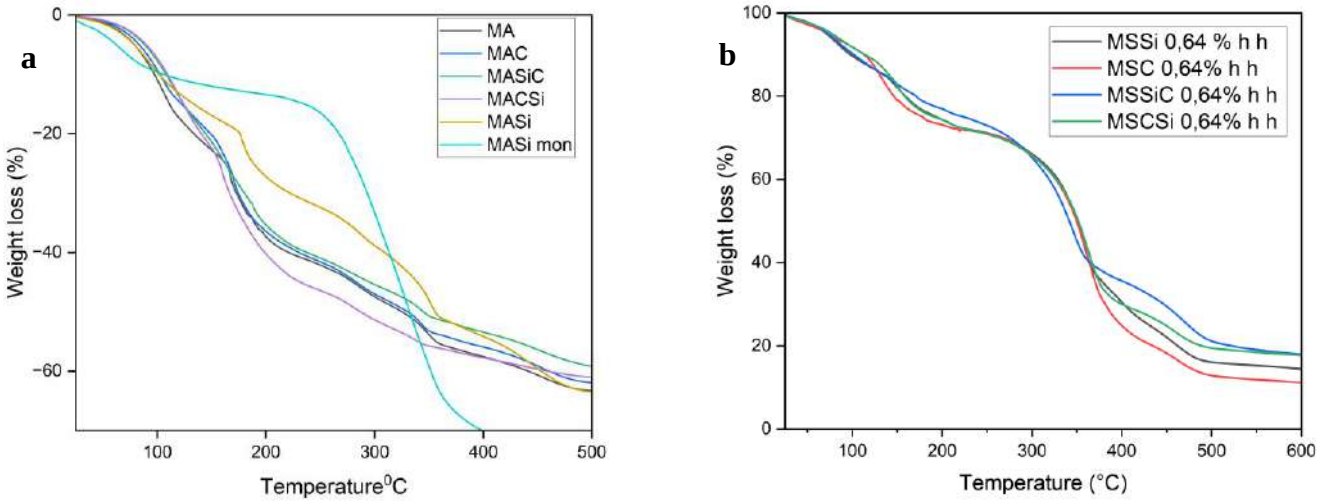

MASi at 164 °C corresponds to the dehydration process accompanied by glycosidic bonds destruction and fabrication of calcium carbonate, the damage yields 18 % in weight loss, in the three stages to 362 °C a complex alginate decomposition takes place, advanced glycosidic pyrolysis and formation of anther intermediate, go along with PCM evaporation, the fused steps result in 50 % of capsule destruction, The last stages presented more degradation of the prefabricated intermediate to more stable phase generally mineral oxide as calcium oxide, carbon dioxide, calcium hydroxide. The pyrolysis in all the phases releases carbon dioxide and evaporated water (Zhang et al., 2011) (Liu et al., 2014) (Lian et al., 2011). The mono shell of

silicate-alginate microcapsule (MASi mon) shows a different degradation manner, with a loss of 13.6 % at 210 ℃ and a big slope of 65 % at 223℃, emphasizing water evaporation at first and alginate decomposition with PCM evaporation in the second.

The mon-shell alginate-silicate thermogram shows enhancement in the thermal stability of the single-shell compared to the double-layer (MASi), due to the large amount of PCM in the hole capsule. The PCM extended the degradation temperature of capsules, which is confirmed in (Figure 6. a).

As mentioned above, the delay in the decomposition of the single layer conforms to the high ratio of PCM, and this phenomenon isn't well defined at the double microcapsule shell due to the faint PCM fraction, thus at high loading in microspheres (Figure 6), The evaporation of PCM in MSSi was attenuated at 245℃ while adapting 210℃ in MASi mon, which indicates that the thermal stability enhancement of PCM is related to the shell thickness.

The modified alginate acts differently, fitting the incorporation of minerals, concerning microcapsules, the silicate-alginate MASi postpones the degradation mechanism and offers stability to the native alginate polymer, which is presented as the higher stable sample with a delay of 10℃. The MAC and MASiC illustrate a slight enhancement to alginate compared to MASi, meanwhile, the MACSi reduces the stability of alginate and exhibits lower degradation temperature in all samples prepared by microencapsulation.

The microspheres demonstrate a uniform degradation plateau with a slight impact due to the mineral integration.

It can be noted that the MASi is the most stable sample, and the rest of the microcapsules have different degradation temperatures with a variable weight loss. Interestingly, beyond 362 ℃, all the samples have identical behavior, contradicting the earlier stages. The main reason for the differences is the presence of nanoparticles; thus, the performance changes caused by the decomposition of the minerals at low temperatures, a similar assumption is presented in (Németh et al., 2018).

To investigate the influence of the immersion time on the stability of microspheres, an MSSi sample with 0.64 (w/v) was fabricated under the initial concept of h/h crosslinking step; at the same time, another microsphere was immersed for 7 days in a crosslinking bath to emerge

Figure 7. TGA study of a. the effect of the immersion time, b. the effect of the third shell

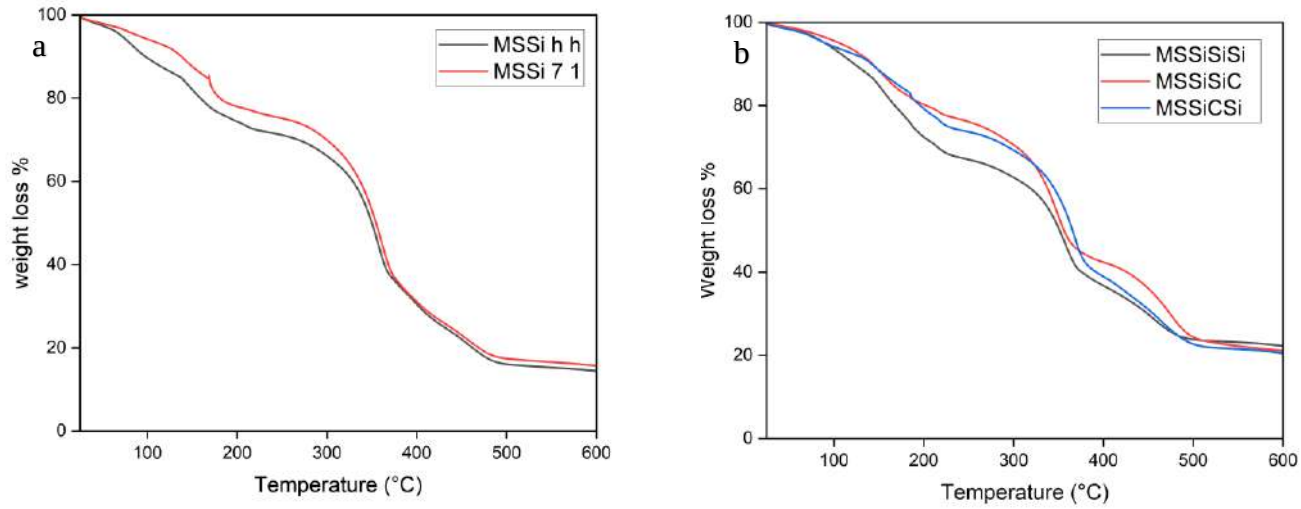

The first shell. The second layer is formed by being submerged for 1 day. The obtained microsphere is mentioned MSSi 7/1. (Figure 7) displays an improvement in thermal stability, with the onset degradation temperature raised from 120℃ to 135℃ This improvement indicates that immersion time is a crucial factor in the bead fabrication, not only as a mechanical enhancer treatment as shown previously, but as a thermal improver.

The residue from the pyrolysis of samples exhibits stability in flame retardancy due to the high amount of residue found in the final treatment, especially in the double shell. The third shell was elaborated to understand the coating process efficiency, 0.64 %(w/v) is fixed, and the same protocol was imposed to produce the new layer. The silicate microsphere was selected for its stable behavior in the early experiment. (Figure 7) exposes the change in attitude correlating to the sequence of layers. The MSSiSiSi reveals the lowest stability, while the other samples display a slight difference in thermal resistance.

An attempt was made to conceive the relationship between concentration and crosslinking, which affects the physique and thermal properties. MSC of 0.64%, 1%, and 1.5% were fabricated and induced to heat flow, of samples illustrated in (Figure 8). The optimum fraction concluded from the experiment is 1%; an increase in the concentration above this value hinders the intensification stability. As shown in a curve, the specimen of 1.5% imposes an inverse attitude, the included portion instead of maintaining the formed particle reverses it and reduces the stability to be inferior to one percent enhancement.

Figure 8. a. TGA study of concentration influence, b. comparison of different thermogram.

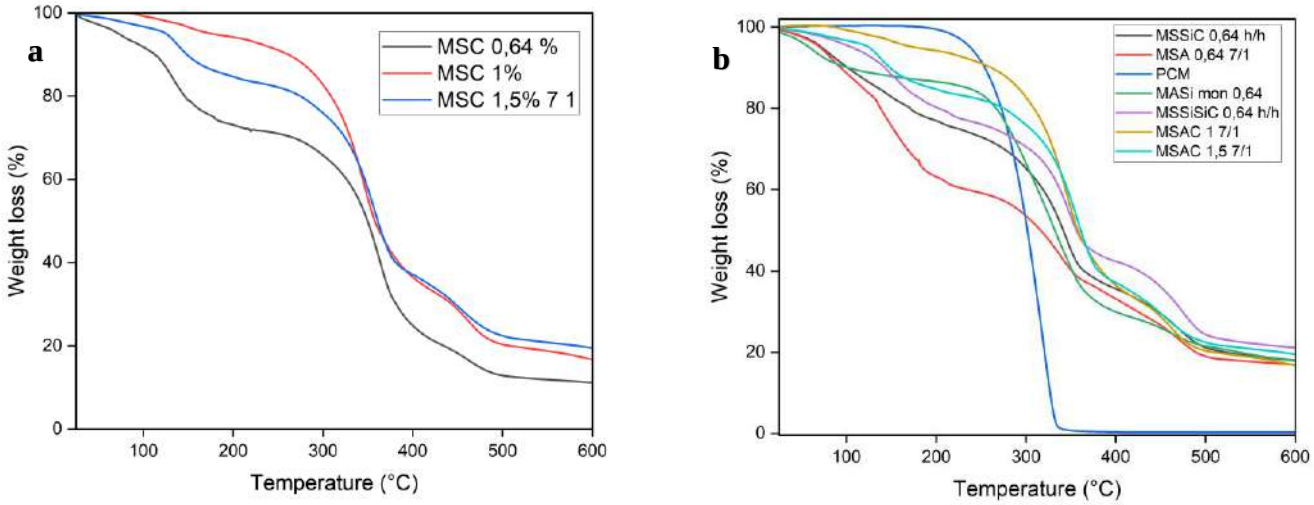

Thermal gravimetric analysis was carried out to investigate the enhancement of minerals incorporation, the concentration effect, the immersion time efficiency, and the duplicate shell on the thermal stability. (Figure 8) present the thermal behavior of the pre-formed specimen, given a wide understanding of the most important factors. As shown in the thermogram, the MSAC 1% 7/1 (Alginate-CaCO3) is the most stable sample, and the MSAC 1.5 7/1 is placed as the second one; MSSiSiSi exhibits less stability. From this classification, a concentration of 1% is the optimal portion. Extending the crosslinking time was recommended, especially for forming the first shell, until 7 days are necessary. for completing the process, the second layer needs one day of crosslinking time, this condition is suitable for generating a durable particle.

The appropriate concentration is a crucial factor in the stability escalation, enlarging the protective layer is effective in certain conditions, and is fixed as a supportive element. This comparison ensures that the layering increases the preservation of the PCM inside the capsules compared to a single coat. This phenomenon is more intense with escalating the shell.

2.4 Performance investigation of the new latent heat materials

The DSC thermographs of PCM and microcapsules are shown in (Figure 9), and the analytical data are displayed in (Table 1).

Figure 9. DSC thermogram of MA, MACSi, PCM, MASi, MSAC 1%.

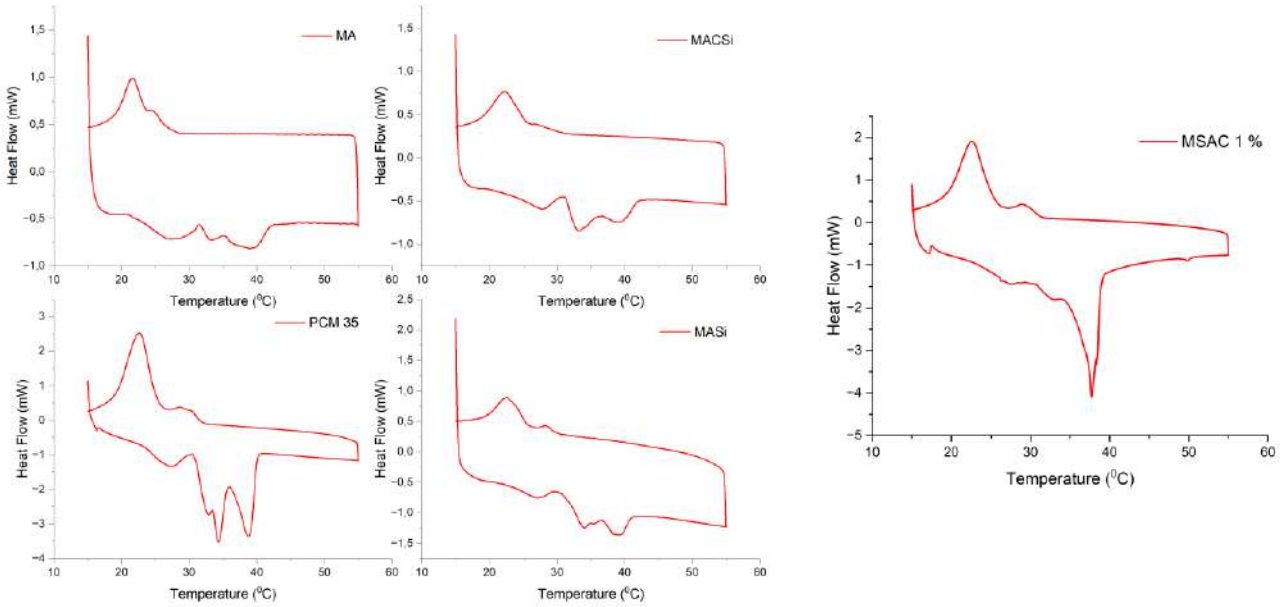

Sample	Melting phase			Crystallization phase			Ratio (%)	E (%)
	T_{onset} (°C)	T_{peak} (°C)	ΔH_m (j/g)	T_{onset} (°C)	T_{peak} (°C)	ΔH_s (j/g)		
PCM	30.10	34.19	62.73	25.25	22.67	66.84	/	/
MA	31.78	39.54	5.01	24.39	21.69	12.6	7.98	13.57
MASi mon	30.86	37.58	30.19	26.67	22.86	41.86	48.12	55.52
MACSi	37.38	37.38	4.80	26.22	23.41	10.42	7.65	11.73
MSAC1%	36.73	37.60	39.97	25.46	22.65	43.98	63.71	64.7

Table 1. DSC analysis of microcapsules of alginate.

The shell material calcium alginate does not exhibit a thermal behavior in the tested temperature range, the stored energy reveals the PCM capacity.

The PCM has specific characteristics compared to the rest of the material. The transition range temperature and the heat energy storage are the main properties. The encapsulation process remodels the PCM and alters its behavior in different ways depending on the selected material that is used as a barrier.

The PCM melting temperature at the first transition is 30.10℃, the MASi mon shell and the alginate shift the temperature around 1℃, while MACSi and MSAC 1% affect the melting process and delay the transition by 7℃. The crystallization temperature reveals a slight alteration by 1℃.

On the other hand, the enthalpy of PCM in the melting and recrystallization phases is 62.73 j/g and 66.84 j/g, respectively. The prepared samples demonstrate variable values that expose differences in the loading process. In heat absorbance, the MSAC 1% shows a high capacity in heat storage at 39.97 j/g, whereas MASi exhibits 30.19 j/g, contradicting these samples, the stored energy in MA and MACSi is insufficient. For a better understanding of the sample storage capacity, the PCM performance of the microcapsules was necessary. The encapsulation ratio (R), and the encapsulation efficiency (E) are estimated through the DSC measures within the equation below:

$$R = (\Delta H_{m,cap} / \Delta H_{m,pcm}) * 100$$

$$E = (\Delta H_{m,cap} + \Delta H_{c,cap}) / (\Delta H_{m,pcm} + \Delta H_{c,pcm}) * 100$$

$\Delta H_{m,\,cap}$, $\Delta H_{c,\,cap,}$ melting, and crystallization enthalpy of the capsule.

$\Delta H_{m,\,PCM}$, $\Delta H_{c,\,PCM}$ melting, and crystallization enthalpy of the PCM.

Based on the encapsulation ratio results, the weakness of the absorbed energy in MA and MACSi is related to the low fraction of PCM. It is worth noting that the microcapsule's first shell is carried out by a microfluidic technique with a fabrication ratio of 0.02/0.4, and the second is formed by dipping in the alginate solution, Meanwhile, the microspheres fabricated by the emulsion process include 40% of melted PCM.

A logical explanation of this outcome is related to encapsulation efficiency that depends on core/ shell fraction, forming mono-shell capsules doesn’t reduce the energy of PCM as much as the duplicated layer, which enhances the particle barrier and produces a thick material that surrounds the core, and as consequence affected directly the prefixed PCM portion. Another reason to take into account is the oil leakage from the bead surface in the fabrication step due to shrinkage phenomena that extrude amount of the PCM out of the gel in both techniques but pronounced in the emulsion method and that happened before forming a continuous surface barrier, also might due to the PCM release in heat treatment step, during the evaporation of entrapped water inside the gel, small fraction wasted before the phase transition and the

rearrangement of structure, and this confirmed the oil found in hot plat and shiny capsules in heat treatment, an identical result reported by (Fundueanu et al., 1998) (Németh et al., 2015).

Considering that the feeble melting enthalpy is related to the low-loaded PCM in the fabrication process and taking into account the description above about the loss of PCM during the preparation process, the enthalpy record indicated that the shell of microcapsules did not affect the performance of the phase change material.

2.5 Thermal conductivity measurements of the fabricated matrix

Thermal conductivity is a crucial parameter for materials characterization. The steady-state technique is usually used to measure the thermal conductivity of bulk materials. A thermal conductivity apparatus coupled with a steady-state technique was used. The measurement principle is based on transferring the heat flux through a bundle item, taken after reaching a stable temperature, and showing no change in reading with time. Where the specimen is sandwiched between two cylindrical stainless-steel bars, the area of the studied sample should be the same as the bar to maintain uniform thermal transfer. The cascade was arranged between a heat chamber at the top, controlled by an ampere and a volt meter, and a water-cooling system at the bottom. This framework is insulated to prevent heat loss.

Thermal conductivity equation (K) :

$$K = \frac{Q * L}{A * \Delta T}$$

Where: Q ($w.m^2$) is the heat flow.

L (m) is the sample length.

A (m) is the sample surface area.

ΔT (k) is the temperature difference of the sample.

The amount of heat passing through the system is identical, with no loss of energy

$Q_{bar} = Q_{sample} = Q_{water,}$ the heat flow of water is given:

$$\mathbf{Q = m*Cp*\Delta T}$$

Where: m is the mass flow rate, 0.0 20 $Kg.s^{-1}$, the quantity of water used for the cooling.

Cp is the heat capacity of water 4.187 ($J.kg^{-1}.k^{-1}$).

ΔT is the temperature difference of water before and after the cooling process.

The thermal conductivity enhancement is stated as follows:

$$K_{enh} = K_{com} / K_{const}$$

K_{com} is the thermal conductivity of the composite, while K_{const} is the thermal conductivity of the constituent.

Inciting the small geometry of the capsules, a matrix of gypsum and samples was carried out of each capsule (Figure 10), and the specification measure of the stainless-steel cylinder was respected. The PCM matrix is engineered to have a high value of PCM near saturation state, while the other capsules are designed to have a fraction close to 40%. The MA presents 44% of the matrix weight, The MACSi matrix is generated to have 40%, 39% is the MAC fraction, and 41% MASi, except for MASi, which was created at 29%.

Figure 10. Procedure of matrix realisation.

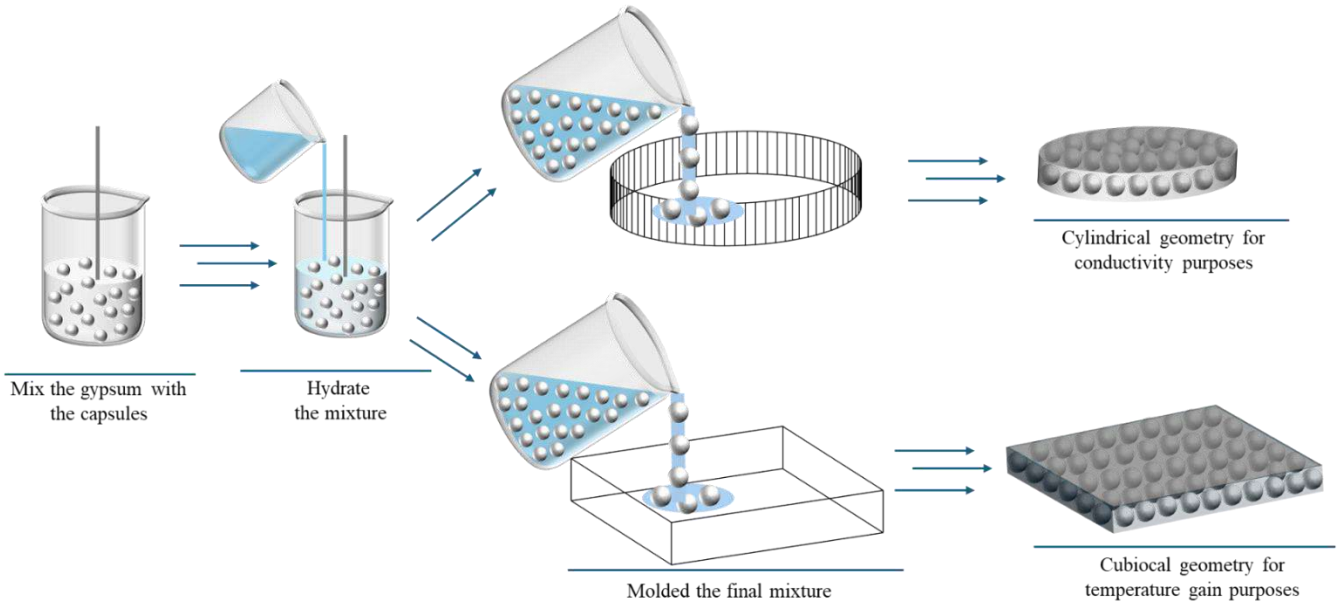

(Figure 11, a) Present the thermal conductivity of the matrix made by incorporating the microcapsules. The measuring strategy is based on the attitude of PCM under heat treatment.

Figure 11. the variation of thermal conductivity of, a. microcapsules, b. microspheres.

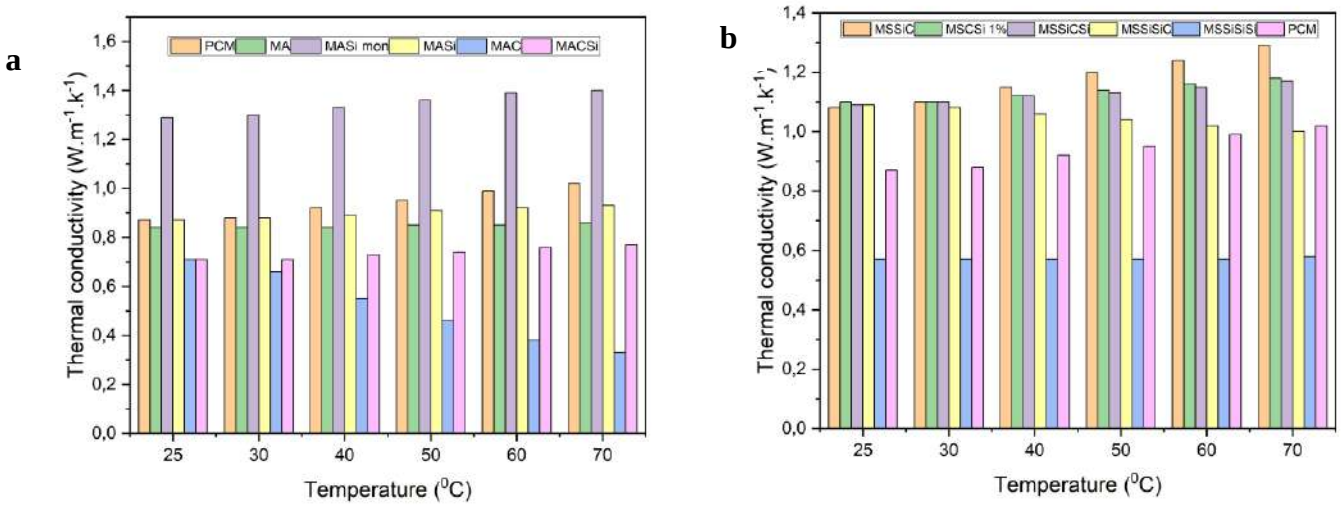

The measurement was accomplished at room temperature to investigate the effect of PCM in the solid state. On the other hand, a batch of high temperatures was applied to ensure the transition phase of PCM to the melt state and examine the change in the matrix.

At 25°C, the samples exhibit low thermal conductivity, referring to the PCM matrix value of 0.87. The MASi mon matrix alters the trend and demonstrates a high value of 1.29. As the temperature increases, all samples display similar behavior, characterized by a conductivity improvement with a slight shift to a higher value. However, the MAC matrix contradicts this behavior and decreases with rising temperature. (Table 2) represents the calculated thermal conductivity enhancement, the MASi mon improves the thermal conductivity of MA by 2 times, considering the low fraction of (MASi 29%), and MASi ameliorates the polymer by one time. The rest of the samples reduce the thermal conductivity of the bulk. Depending on the results of K_{enh}, the calcium silicate particles escalate the heat transfer within the alginate polymer at a minimum by one time to a double effect in a single shell. The calcium carbonate, as data shows, hinders the alginate polymer's conductivity. Regardless of whether MASiC has both particles, the matrix reduces the general bulk, but the enhancement does not cease as temperature increases, contrary to MAC, which displays a continuous decrease proportional to the temperature.

Temperature	Kenh					
℃	**25**	**30**	**40**	**50**	**60**	**70**
MA/PCM	0.96	0.95	0.91	0.89	0.85	0.84
MASi mon/MA	1.53	1.54	1.58	1.6	1.63	1.62
MASi/MA	1.03	1.04	1.05	1.07	1.08	1.08
MAC/MA	0.84	0.78	0.65	0.54	0.44	0.38
MASiC/MA	0.84	0.84	0.86	0.87	0.89	0.89

Table 2. Thermal conductivity enhancement of Alginate microcapsules.

(Figure 11, b) present the thermal conductivity of the matrix microspheres. The same strategy was applied to identify the conductivity in the solid state, as well as the activation energy in the melting phase. The measurement was executed at room temperature to investigate the effect of PCM in the solid state. On the other hand, a batch of high temperatures was applied to ensure the transition phase of PCM to the melt state and examine the change in the matrix.

The MSSiC 1% (7/1) Matrix is built by 37% of microspheres, and 39% of MSCSi 1% (1/7) is integrated into the matrix. The portions of the triple shell microspheres of MSSiSiSi, MSSiCSi, and MSSiSiC in their matrix are given by order 34%, 30%, and 38%.

At 25℃, the samples show high thermal conductivity compared to the PCM matrix. The MSSiSiSi displays a low value of 0.57. As the temperature increases, the specimens demonstrate random behavior. The MSSiC, the MSCSi, and the MSSiCSi columns elucidate a conductivity improvement with a shift to a higher value. However, the MSSiSiC matrix contradicts this behavior and decreases with rising temperature. A settled behavior exposed by MSSiSiSi under heat treatment broke at 70℃ by 0.01 escalation (Table 3) Represents the calculated thermal conductivity enhancement, the MSSiCSi improves the thermal conductivity of MA by 1.20 times. MSCSi and MSSiC ameliorate the polymer at one and a half. Contradictory the sample of MSSiSiC reduces the conductivity of the matrix. And as described before, the specimen of MSSiSiSi sequestrates the heat treatment and remains in a stable phase.

Temperature °C	Kenh					
	25	**30**	**40**	**50**	**60**	**70**
MSSiC1%(7/1)	1.28	1.3	1.36	1.41	1.45	1.5
MSCSi 1%(1/7)	1.3	1.3	1.33	1.34	1.36	1.37
MSSiSiSi	0.67	0.67	0.67	0.67	0.67	0.67
MSSiCSi	1.29	1.30	1.33	1.32	1.35	1.36
MSSiSiC	1.29	1.28	1.26	1.22	1.2	1.16

Table 3. Thermal conductivity enhancement of alginate microspheres.

2.6 Durability study of Alginate microcapsules

The thermal cycling test was performed to evaluate the chemical stability of the capsules during the freezing and melting processes. The microcapsules MASi and MAC were heated above their melting point and subsequently cooled. We employed Attenuated Total Reflectance Fourier Transform Infrared Spectroscopy (ATR-FTIR) and Scanning Electron Microscopy (SEM) to investigate the chemical and morphological alteration of cycling.

After completing 100 melting–freezing cycles, (Figure 12) presents the SEM coupled with EDX images of the microcapsule cross-section. Based on the micrograph, it is obvious that the core is nucleated and surrounded by a clear layer without any mark of PCM release or evaporation. On the other hand, the microcapsule preserves its sphericity, as shown by no deflection caused

Figure 12. SEM image of MAC after 100 cycles.

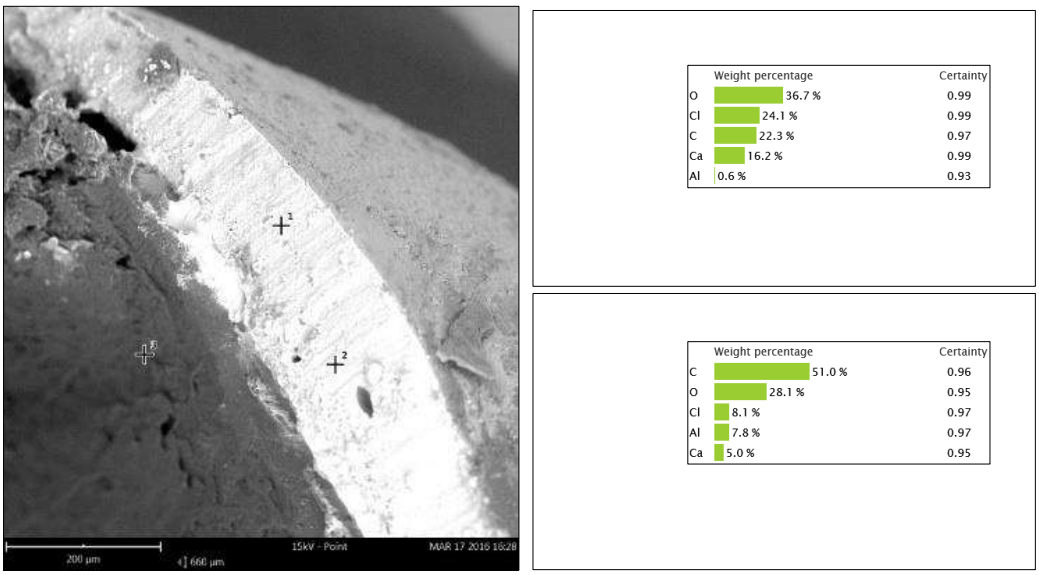

by the progressive rapid cycles, concluding that the MAC has high thermal performance.

(Figure 13) illustrates the spectra obtained before and after the cycling test of the MASi microcapsule, displaying identical absorbance peaks with a difference in intensity, no new peaks appear or disappear, which confirms that the microcapsules remain stable without any chemical degradation.

Figure 13. FTIR of MASi sample after 100 cycles.

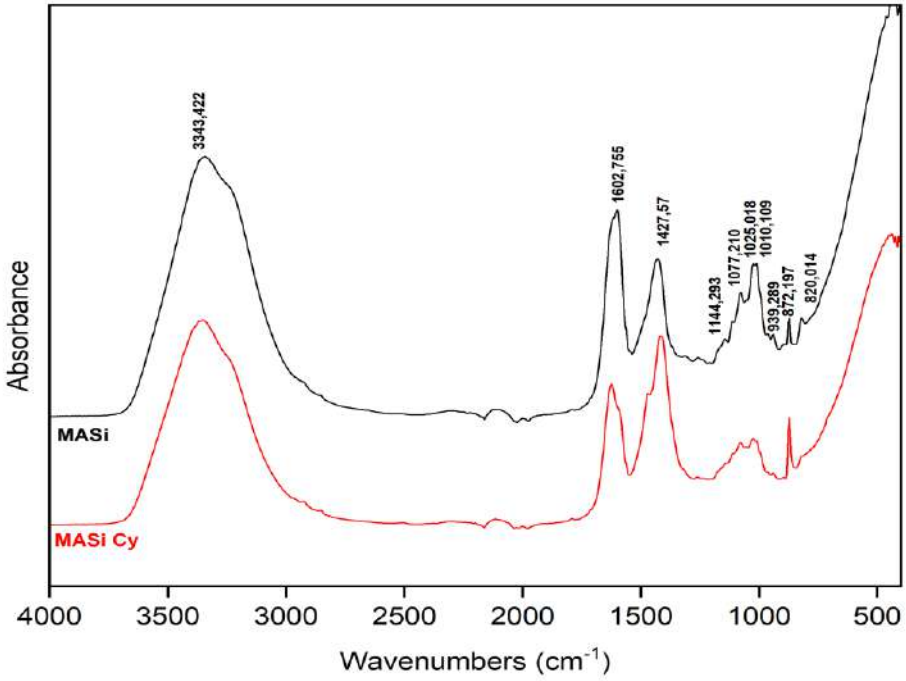

2.7 Results and Discussion

The alginate encapsulation through extrusion ionic crosslinking method using calcium chloride is executed in two trajectories: a microfluidic system to produce a mononuclear capsule (microcapsules), and through emulsion, to generate microspheres. The fabrication mechanism is visualized over the diffusion setting method (Figure 14) The moment the generated drop traverses the calcium chloride solution, a spherical intact barrier continuously increases with time due to the electrostatic forces between the calcium cations and the negative carboxylate groups in the sodium alginate (W. Wang et al., 2024) which was identified by a progression of white opacity on the surface as described before, the cation has a binding affinity to G sequences, forming a heat-stable three-dimensional gel network (Ramdhan et al., 2019) where

the binds capacity of calcium load four G units bestows an “egg-box” gel structure as a result of bringing the chains closer and forming a less permeable surface.

Figure 14. illustrative stages of alginate fabrication mechanism.

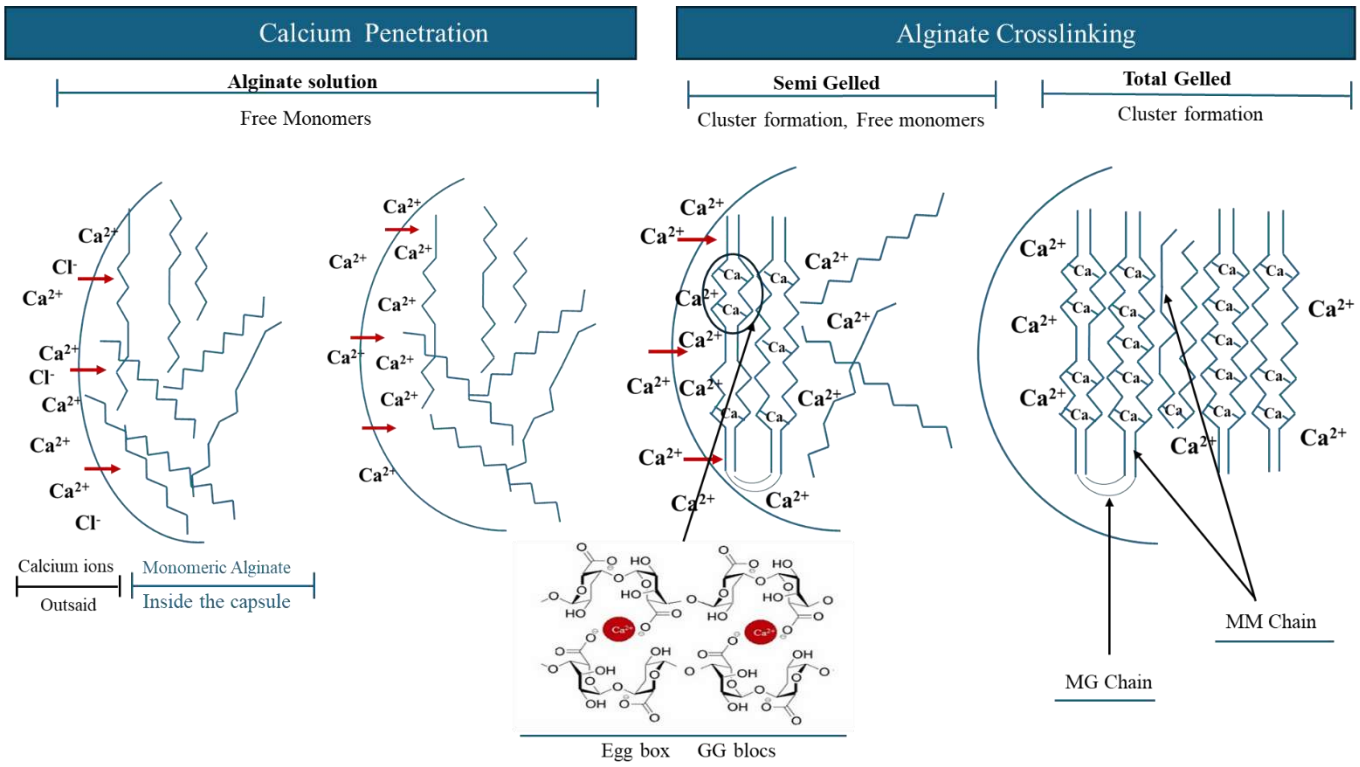

The enlargement of the formed belt indicates the calcium diffusion from the crosslinking solution to the core droplet.

The maturation process needs more time to generate a hard bead, which confirms the soggy form and the presence of liquid inside the bead in the early stage. The same observation was recorded by (Ayarza et al., 2017a). The gelation mechanism is based on the formation of a calcium alginate network layer by layer, which requires a high amount of linking agent that provokes, as a result, a fast crosslinking rate and results in a compact superficial layer that hinders calcium penetration to bind the free alginate moieties, the same observation found by (W. Wang et al., 2024). The optimal condition to fabricate a homogenous calcium alginate bead structure was the aim of many researchers. The alginate concentration of 15 to 25 g/l with a respective fraction of 4:5 calcium chloride was the ideal range between fragile networks that affected the mechanical strength and suppressed strength that affected the loaded element in the encapsulation case. On the other hand, the literature highlighted the issue of excessive

calcium consumption in bath linking which impeded the latter formed bead, particularly in large quantities. In this work, we optimize the experiments, taking into account the described above, 2 % (w/v) alginate solution was selected to moderate a strength gel construction and maintain the mobility of calcium within the initiate reticulation, a calcium chloride batch with gradual concentration designed to ensure the calcium diffusivity and sustain the penetration ability through the alginate solution to form a gel in the first step and preserve the calcium availability in the maturation process to enhance their integration and remain the osmotic equilibrium.

The delayed crosslinking time of the first shell (droplet gelation) enhances the stability and persuades the adsorption of the outer shell. The fabrication mechanism of the outer shell emphasizes two processes. A superficial layer emerges immediately after dipping the bead in the alginate solution, ascribed to the diffusion effect of calcium ions from the polarized sites inside the preformed inner shell (first shell) (Németh et al., 2015) (Bienaimé et al., 2003) whereas the layer expands into soaking in calcium chloride solution after retrieving the bead from the alginate sol. The suitable thickness of the final layer is related to the dipping time in the alginate solution.

Previous research described the complete gelling process by plateau term, the majority of the results found that 10 minutes is sufficient time to reach the plateau stage (Ayarza et al., 2017a; Németh et al., 2018), and for the large scale (centimeter), 110 minutes is enough. (Bienaimé et al., 2003) Rreported on the existence of positive charges inside the gel bead; these results are endorsed by the wide knowledge of calcium alginate gel porosity. We assume, that the incorporation of minerals enhances the mechanical properties by occupying the space inside the gel and thinning the void by the growth process in the polymer taking the privilege of the big radius of minerals, a comparison alginate binding study with different divalent cation embraces the hypothesis (Bajpai & Sharma, 2004), extending the maturation period expanding the particle size, and protruding the water, the thermogravimetric analysis affirmed this hypothesis the increased mineral loading decreases the weight loss concerned the evaporation water, the same outcome shown by (Cao et al., 2024). Identical efficiency is found in prolonging the maturation time, which reduces the water quantity inside the capsules. This result is demonstrated in the TGA, which illustrates the effect of immersion time.

In the case of hybrid alginates, the same mechanism was observed (Figure 15), the first thin

Figure 15. Illustrative stages of modified alginate fabrication mechanism.

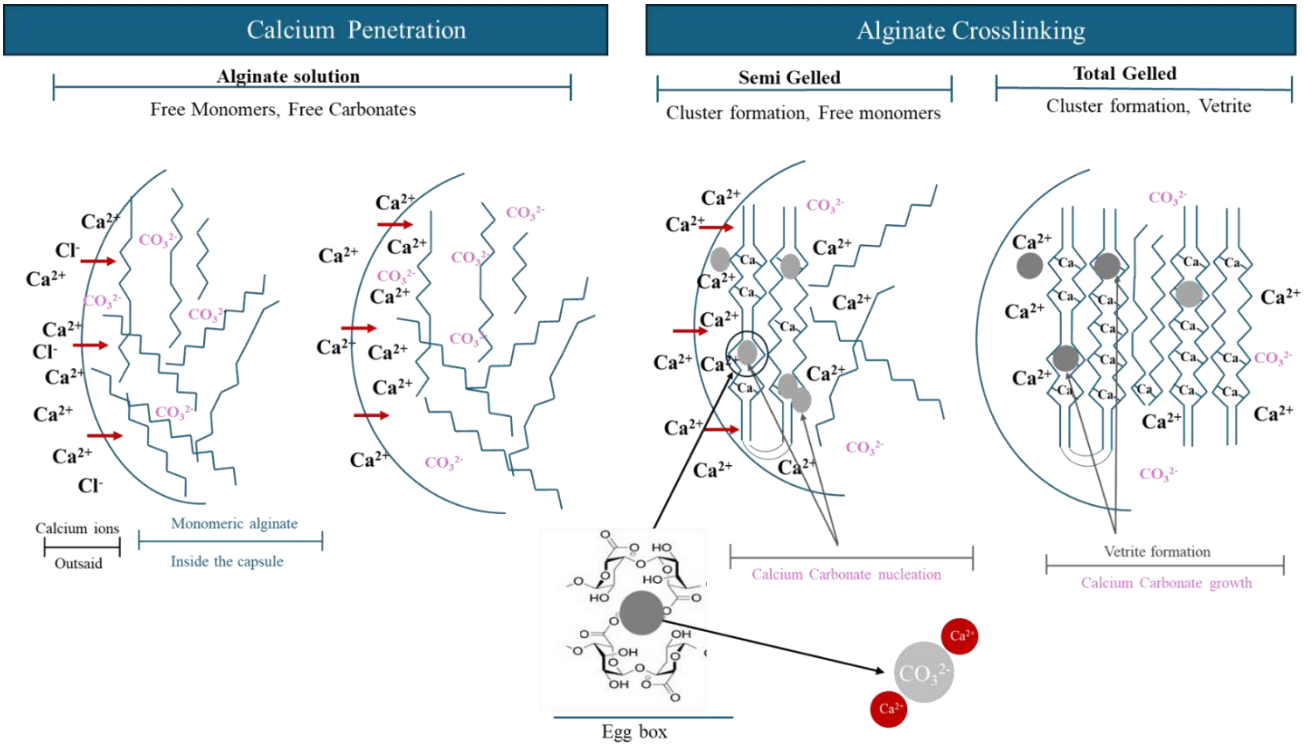

layer due to the diffusion of the compounds toward each other, the minerals and the alginate moieties migrate to the droplet surface at different rates and trends at the frontiers of the globule, attracted by the gathering of cations at the surface, meanwhile, the calcium cations penetrate in the inverse trajectory from the gelling solution to the droplet's center (Bienaimé et al., 2003)**,** (Ayarza et al., 2017b) (Wu et al., 2011).The opposite diffusion is ascribed to the desire to reach the osmotic equilibrium in the bulk solution.

In the advanced crosslinking stage, the behavior of diffusivity changes due to a thick membrane formed gel. Cause the smaller radius, the calcium cation penetrates between the chelators to interact with the unoccupied binding-free sites in the carboxylate and mineral surfaces as well (Serrano-Aroca et al., 2018) (Zhao et al., 2012). The preformed alginate layers sequester the minerals inside the network (Cao et al., 2024) (Wu et al., 2011) due to the high affinity toward the calcium cation and the high interaction between them compared to the minerals which effectively retarded their growth, as a consequence of the entrapment of minerals in the network, the range of particles size has undergone the space available between the chelators. This phenomenon explains the condensed superficial layer compared to the middle zone, which is clear in minerals existence within the coat; the high reflection seen in the upper zone in each

shell gradually decreases to the bottom, as found before in SEM results. (Serrano-Aroca et al., 2018) (Zhao et al., 2012).

Two hypotheses concern crystal growth inside the gel. The sequestrated minerals interact with the calcium, nucleate, and grow inside the space between the chelators. From another perspective, clarify the impact of free alginate moieties that give rise to the minerals adsorbed onto the unbounded sites.

Based on FTIR results, the minerals fingerprint region displays a low intensity, exhibiting the lack of presence of crystals, considering that 30% of bulk polymer is minerals at the beginning of the process, this outcome heralds that the low absorbance ascribed to the alginate reticulation that acts as barriers in growth mechanism, indicates the need of more time for accomplish the precipitation reaction of minerals and that confirmed by results of prolonging the maturation time as illustrated in the TGA analysis of comparison the soak of MSSi h/h to MSSi 7/1. The SEM micrograph of the MACSi section shows spherical geometry and agglomeration particles in the inner shell, ascribed to calcium carbonate crystals. The variety of crystal morphology indicates the posed hypothesis, the unique crystal displays the fabrication of carbonate crystal without any interference, while the aggregate particle geometry elucidates the adsorption process.

The knowledge of calcium carbonate precipitation comprises, at the beginning of the process, only the amorphous nanoparticles that were formed, which became the nuclei for the crystallization of vaterite. In normal conditions, in the final phase, the vaterite transformed into a more stable form of calcite or aragonite. It is widely known that calcite has cubic morphology, either prismatic a spherical imprint.

The SEM micrograph displays contradictory results to knowledge, exhibiting a spherical shape after a long period of maturation, indicating that the vaterite spherulite dominates in a saturated environment. (Yu et al., 2014) mention in high calcium settings, the precipitation tends to form the vaterite class, (Kosanović et al., 2017) explains that the supersaturation level above the vaterite solubility hinders the dissolution of vaterite, which is the first step in recrystallization of calcite; meanwhile, another reason is affirmed by (Sovova et al., 2021) demonstrating that the ordinary transformation sabotages under 20 °C, as proved by vaterite domination in FTIR and SEM analysis in this study.

On the other hand, the agglomerate was detected in the SEM micrograph displaying an adsorption phenomenon, which interprets the interaction possibility between the alginate

carboxylate group and free sites on calcium carbonate particles, we assume in the reticulation process, the networks sequestrate the unbounded carbonate ions, which favorize the nucleation and expose an agglomerate geometry, which leads to the low presence of minerals reflected in FTIR analysis. At the basic level, the preformed bound blocks the growth sites of the particles and hinders the crystallization of calcium carbonate.(Kawano & Koyama, 2024) (J. Li et al., 2009)An identical outcome was concluded by (Olderay et al., 2009), which assumed a mechanism consisting of two steps. In the first phase, the alginate induced the vaterite seeds to stick together, followed by a growth step to fill the gaps between crystals.

According to FTIR, the peaks appear in MAC found in all microcapsules containing carbonate addition. The presence of vaterite and calcite reveals a transformation from a polymorph structure of calcium carbonate to a more stable form, explained by the appearance of calcite, and the remaining initial form, vaterite spherulite, indicates incomplete dissolution. In this case, we assume that the agglomerate in the SEM micrograph tends to be calcite prismatic with a spherical imprint.

The FTIR of MASi and all microcapsules contains an addition of sodium silicate, displaying bands revealing the silylation process. (Kusuktham et al., 2014)Suggests the shifting in the OH bond exposes interaction between the calcium silicate precisely; the divalent ion, side group on the surface, and carboxylate groups. SEM micrograph reinforces this outcome by surrounding the microcapsules with opacity whitening compared to the rest designed microcapsules, the same phenomenon was found by (Kusuktham et al., 2014; Wu et al., 2011) (Kusuktham et al., 2014).

During the maturation, the shrinkage of capsules was continuously observed to achieve water-insoluble hydrogel, this phenomenon was related to the increasing of alginate bounding and can be explained by the syneresis process (Velings & Mestdagh, n.d.), while the electrostatic attraction extruded the water from the gel networks due to bringing the polymer chains close together, and decreased the internal void. The syneresis impairs the repulsion forces that maintain the stretching conformation of deprotonated carboxyl groups to charge the space between them by absorbing water to reach the osmotic equilibrium. (W. Wang et al., 2024), (Zhao et al., 2012).

The porosity of calcium alginate diminishes with the rise in calcium. (Pathak et al., 2010), which confirmed the absence of leak PCM in the maturation step, a cause of the high reticulation that minimizes and fills a large space between chelators and reduces the free carboxylate, which is the main reason for porosity via the absorption process as described in

osmotic equilibrium (Sriamornsak et al., 2008), addition to the calcium efficiency, (Aslani & Kennedy, 1996) Highlight the drying process as an effective factor to reduce porosity.

The drying process is a crucial parameter, particularly the strength bead, the treatment slope rapidly from the water evaporation mechanism to the diffusional model, owing to bounded hydrogen water to oxygen at the 2nd and 3rd position in the pyranose ring of alginate during the beginning of the drying and assesses high energy to strip the water, (Vargas et al., 2018), (Németh et al., 2015)Consolidated the fabricated PCM microspheres by a high alginate concentration under 120℃ for 15 minutes.

In the current study, heat treatment at 100℃ for 15 minutes was preferable to adapt the alginate glass transition of the hydrogel gel bead and prevent the decomposition of alginate or damage to the minerals surrounding the bead.

The drying process favors the shrinkage of the bead, which, as a consequence, affects the porosity in the hydrogel texture. The water is retained in an unlinked state, free water, and could be found in a bounded form. The heat treatment induces the uncoupled water to squeeze and evaporate; in this case, instantaneously, the interior structure rearranges and gets closer to filling the void after water release, and that explains the vapors and the diameter reduction of consolidated capsules compared to the hydrogel bead, as shown (Figure 4). This phenomenon is clearer with a gradual temperature rise. It is important to mention that bound water needs more energy to extract and thus might damage the texture and start the decomposition phase, as demonstrated in TGA curves. (Bajpai & Sharma, 2004) Postulated that the drying mode and heat treatment affect the porosity to different degrees. (S. Kim et al., 2019)Established at low heat treatment, 40℃ the calcium alginate bead exposes pore structure and is less seen with high temperature at 70℃, while at 100℃, it illustrates a compact, homogenous distribution network, the same results found in the SEM micrograph.

(Németh et al., 2018) Asserted that the high PCM loading can be reached by enveloping the core with a thin layer, but criticized later as unstable mechanically, and mentioned that the highest fraction that can be confined is 40% in stable microspheres. (Fundueanu et al., 1998) Assigned that the low alginate concentration provokes the shell porosity and affects the entrapment of PCM. Which impacts the loading efficiency as a consequence.

In this study, we prepared hybrid alginate samples with high thermal stability at high PCM loading without observing any leakage, which indicates a practical capsule for integration.

Chapter 3. PVA POLYMER EFFICIENCY

PVA is an atactic polymer obtained by free radical polymerization of vinyl acetate and successive hydrolysis. The hydrolysis of poly (vinyl acetate) (PVAc) does not convert all the acetate groups into hydroxyl groups but gives rise to PVA polymers with a partial degree of hydrolysis that depends on the extent of the reaction. The properties of PVA are strongly influenced by the degree of hydrolysis (De Rosa et al., 2014)

3.1 Preparation of PVA microspheres

The samples were generated by extrusion of conventional oil-water emulsion using an in situ polymerization technique (Figure 16). The beads were prepared in different compositions to obtain PVA and modified PVA microspheres. The hybrid PVA was synthesized by gradually adding titanium dioxide nanoparticles (TiO_2).

The PVA gel was prepared by dissolving the polymer powder in distilled water to obtain a concentration of 7.5 % (w/v) at 90 °C until forming a homogenous gel.

Figure 16. Fbrication procedure of PVA and modified PVA.

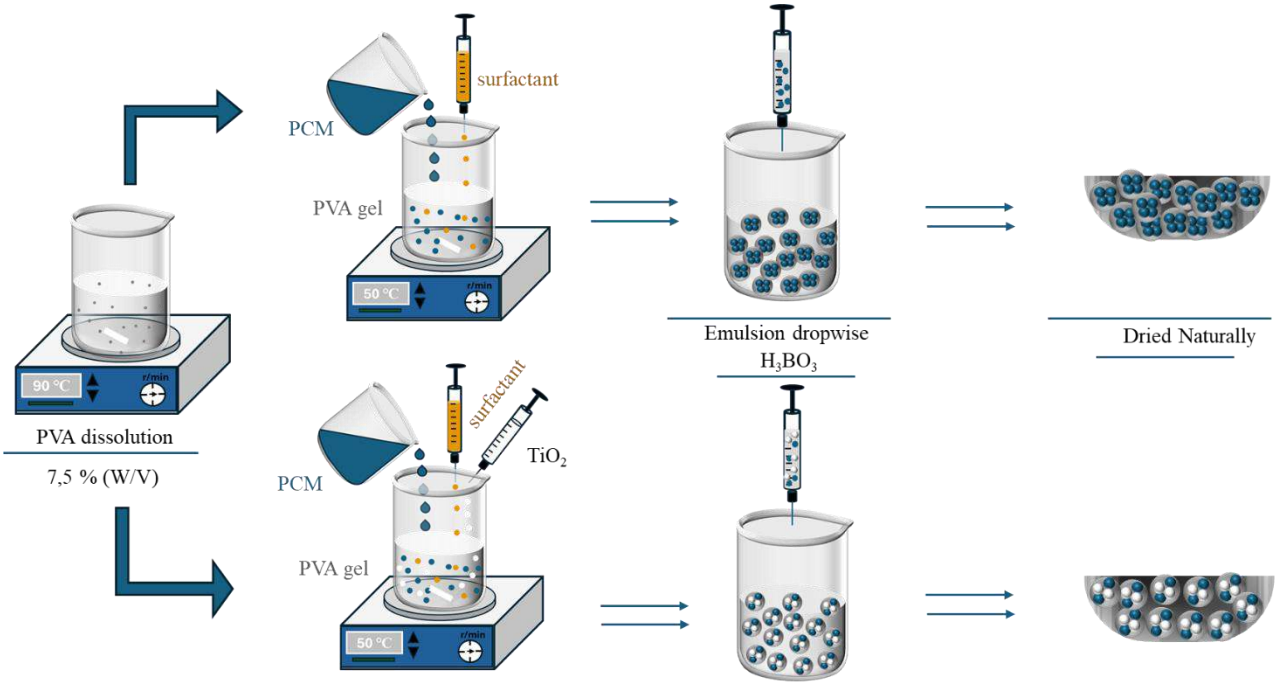

The mechanism was designed to fabricate a homogenously dispersed microspheres, the procedure started by dropping the melted PCM oil in the previously prepared PVA gel under

continuous stirring, the bulk solution was stabilized by adding a surfactant, and the emulsion of 60/40 % (w/w) PVA/PCM was squeezed out using a syringe into a saturated boric acid bath; realizing a concentration of 5 % (w/v) at ambient temperature.

The process was executed in a heated environment to ensure the PCM fluidity. The modified microspheres were fabricated following the same procedure using PVA nanoparticle gel by incorporating 2, 5, 8, 10, and 17 % (w/w) of titanium dioxide into the prepared PVA gel. In this case, the emulsion fraction was changed, and the PCM ratio was fixed, while the new fraction of PVA included the TiO_2 ratio. Thus, 60 % of the continuous phase consists of the PVA amount and nano TiO_2. The obtained beads were collected after aging for further analysis.

It is worth noting that three types of PVA beads were produced in this study labeled as follows, the precursor or the crosslinked PVA gel (SP), the microsphere PVA/PCM or the pristine (MSP), and the modified PVA/PCM by titanium dioxide nanoparticles integration which laybled, the hybrid (MSPTi x%) while (x present the fraction of TiO_2)

3.2 The performed samples aspect morphologically.

The prepared microspheres are investigated using a scanning electron microscope to better understand the microscale structure of the prepared samples. At the beginning of the fabrication mechanism, the spherical droplet was plunged into a crosslinking solution, a fragile bead was fabricated and developed to a solid state, along with prolonging the crosslinking period.

Decreasing the elasticity and increasing the strength, the transition from gel to solid form demonstrates the ionic crosslinking of PVA with boric acid.

The SEM micrograph in (Figure.17), illustrates the different structures of the performed samples, (a) the image exposes the morphology of the PVA bead devoid of PCM (SP), the bead exhibits a network with a range of pores, meanwhile the PVA microspheres (MSP) reveals a compact aspect with fissures as shown in (b) image, and the last micrograph demonstrates the alter of nanoparticles addition, the titanium dioxide displays an agglomeration of hexagonal structure.

Figure.17 SEM micrograph presente cross section of, a. SP, b.MSP, c. MSPTi.

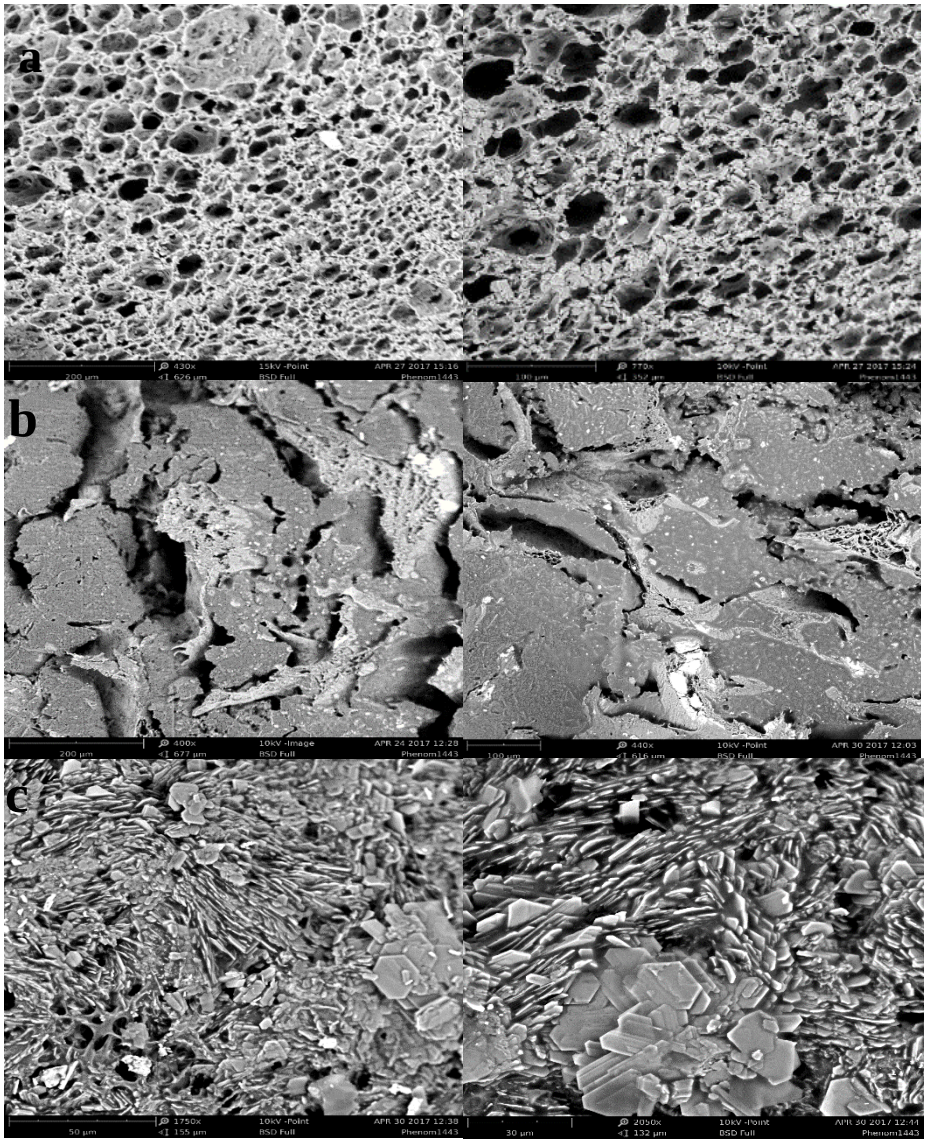

The cross-section of the three types of beads (Figure.17) allows us to comprehend a side of the fabrication process. The PVA polymer (a) exhibits a reticulated structure with a range of micropore sizes, the precursor structure arrangement presents a perfect environment to support the loaded PCM, (b) shows that the PCM remains embedded inside the channels of the network, and exhibits a compact surface with low fissures. Meanwhile, the incorporation of nanoparticles in the case of MSPTi 2 % assesses a heterogeneity to the final texture revealed by titanium agglomeration, the nanoparticles cluster blocks the void of the polymer network.

3.3 Compatibility study of PVA PCM microspheres

The chemical characterization was visualized using ATR-FTIR spectroscopy. The specters of PVA bead (SP), PCM, and microsphere PVA/PCM (MSP) were taken to compare and localize the alteration made by the polymerization using boric acid, and the performance of the fabrication process on the encapsulation efficiency of PCM. Whereas the infrared MSPTi 2 profile gives an insight into the comportment of titanium dioxide in the presence of polymeric membranes.

Figure 18. FTIR of, a. MSP and MSPTi 2, b. the interaction between PVA and PCM.

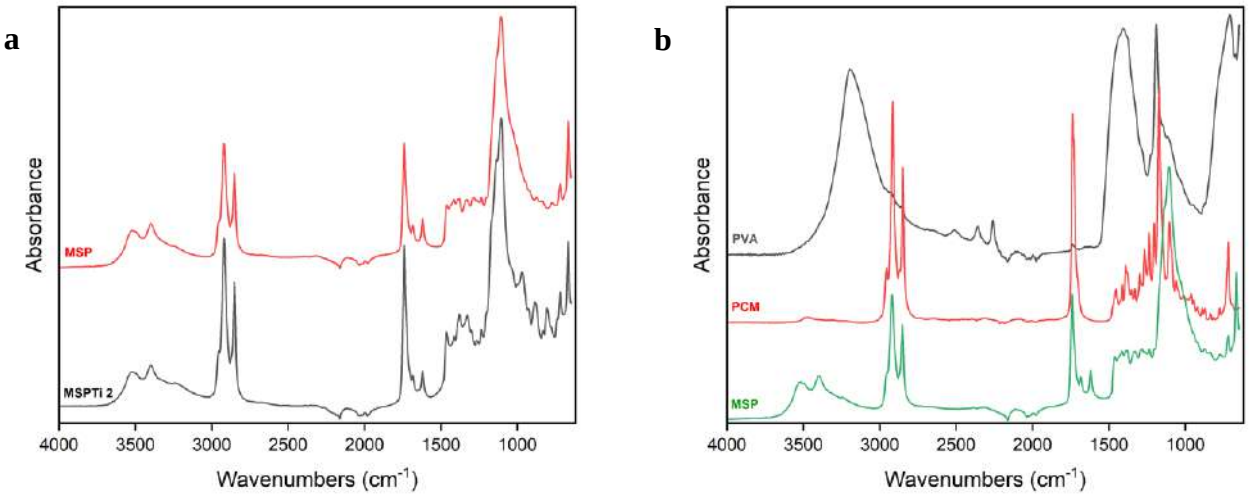

It is notable from (Figure 18. b) The profile of MSP beads is quite similar to the sum of SP and PCM bead spectra with band shifting.

Ain absorption bands of MSP bead can resume in, a small band with two heads presenting OH stretching vibration between 3700 cm^{-1} and 3200 cm^{-1}, and the vibrations at 2913 and 2847cm^{-1} reveal a C–H alkyl stretching asymmetric and symmetric respectively (Zhou et al., 2021) (Lee et al., 2010), whereas the intensity at 1735 cm^{-1} displays C=O vibration of the acetate group, the residues from the polymerization process (Ghorbel et al., 2019), and (Koysuren et al., 2012) mentioned that the vibration related to the newly formed PVB (PolyVinyl Borate) is the outcome of PVA and boric acid reaction, and might be due to the loaded PCM as illustrated in (Figure 18,b), it is widely known that the bonds at 1684 cm^{-1} 1621 cm^{-1} correspond to C═O vibration which is attributed to the esterification of hydroxyl groups in an acidic environment,

(Ahmad et al., 2013)mentioned the binary bond, 1461cm^{-1} and 1379 cm^{-1} indicate the bending of CH_2 vibrations, which reinforce by (Habiba et al., 2017) explaining that the vibration owing to C-H wagging coupled with OH bond, (Sakarkar et al., 2020)demonstrated 1330 cm^{-1} corresponding to CH_2 vibration, when (Lambertini et al., 2024) identified it to the appearance of the new link B-O, the intrinsic results of the prosperous reaction of PVA and boric acid can be summarized in the emergence of the bonds at 775 cm^{-1} and 667 cm^{-1} which were attributed to the B-O-H bending vibrations (Lambertini et al., 2024) (Park et al., 2022) while the second refers to B-OH of solid stat according to (Sun et al., 2020) , and to 1285 cm^{-1} 1130 cm^{-1} were corresponding to stretching bands of B-O-C (Chen et al., 2016) (Koysuren et al., 2012) , it is worth noting that the latter frequency is combined with the 1107 bond, resulting a broad bond with two highs. (Shawgi et al., 2017) declared that the existence of B–O–C bonds confirms the chain cross-linking of PVA with Boric acid.

The comparison of the MSP profile with the MSPTi 2% spectrum shows identical characteristics beyond 1000 cm^{-1}, mentioning the shift toward the high intensity for OH stretching by 8 cm^{-1} and by 4 cm^{-1} for the CH_2 bond, meanwhile, the 1326 cm^{-1} vibration exhibits a shift toward a lower frequency than the neat microsphere. However, the imprint region displays absorbance of new peaks assumed to be related to titanium dioxide. (Salimian et al., 2021) denote the 969 cm^{-1} as the indicator of titanium dioxide nanoparticles, according to (Prosanov et al., 2018) 887 cm^{-1} is B–O–H vibration in a solid state, whereas 805 cm^{-1} reveals the Ti-O-H stretching band (Liu et al., 2015) (Ahmad et al., 2013), a small bond at 708 cm^{-1} attributed to Ti-O-Ti stretching band as mentioned by (Ghorbel et al., 2019).

3.4 Thermal behavior and stability of PVA and hybrid PVA

Thermal stability is a crucial parameter in the durability and sustainability investigation of new materials manufacturing. (Figure 19.a) illustrates the thermal behavior of the MSP and its compounds SP as well PCM under heat treatment, to conceive the effect of each constituent on the final microsphere performance, The PCM illustrates one single slope around 182°C, whereas the SP bead exhibits two degradation phases, the first is according to dehydration of water molecule and the formation of polyene structures with loss of 20 % (Lambertini et al., 2024) (D. Wang et al., 2024) and the second reveals the temperature of PVA decomposition while polyene structures continuously pyrolysis to moieties aliphatic structures (Dodda et al., 2015) and exhibit slow degradation compared to PCM behavior, the gradual decrease referring

to a high amorphous structure (Dodda et al., 2015), which started at 296°C and progress it until 500°C. The MSP illustrates a degradation profile combined with the attitude of the two compounds, which follows the SP act degradation, meanwhile, tends to decompose sharply as PCM at 263°C since it presents a high fraction. The water molecules removal step partially disappears from MSP, which conforms to the FTIR result of decreasing the absorbance of water bonds in MSP compared to SP.

The comparison of the MSP and the modified PVA with a cascade of TiO_2 incorporation is demonstrated in (Figure 19. b). In general, the decomposition of samples has a similar profile with a slight enhancement depending on the titanium dioxide fraction. The most stable sample, performed with the incorporation of 5 %, despite the high thermal stability, which prolongs the

Figure 19. TGA of, a. MSP, PCM and SP, b. the influence of TiO2 on PVA polymer.

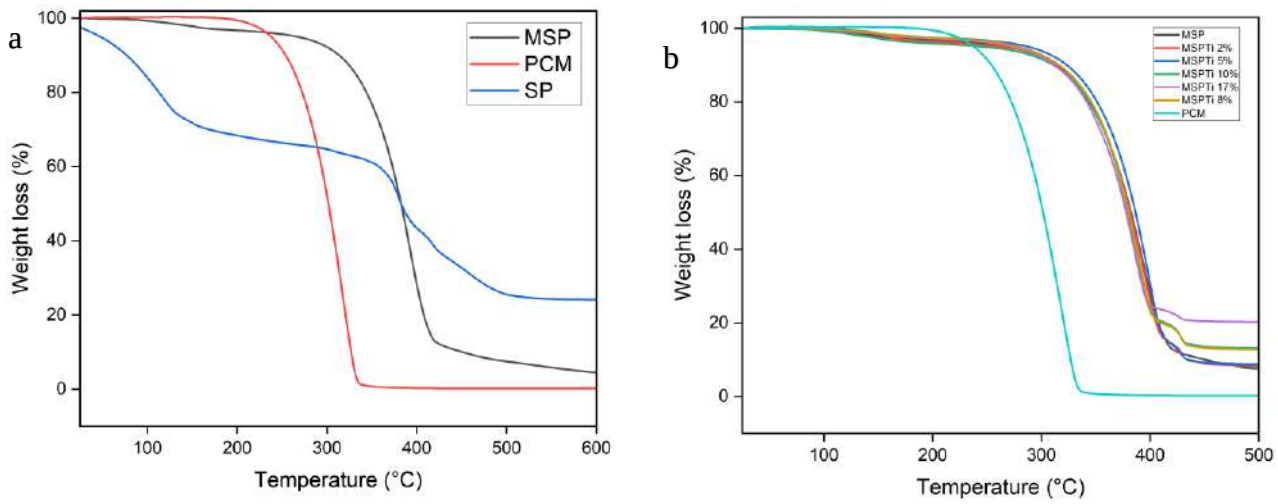

degradation to 274°C, showed the lowest residue after pyrolysis, around 8.7%. The MSPTi 2% had a mere result as 5% with degradation at 272°C and similar residue (8.7%), the rest of the microspheres were damaged at temperatures of 268°C, 263°C, 261°C, respectively corresponding to MSPTi 10%, MSP, MSPTi 8%, MSPTi 17%.

The incorporation of nanoparticles has a random behavior, in which the highest stability comes from 5 and 2% of the titanium dioxide addition, while the 17% could affect the polymer stability and produce a fragile network due to the low amount of PVA polymer in the mixture. Meanwhile, the understandable results of the 10 and 8% fractions in the thermogram show that 10% addition exhibits more stability to the microsphere than the 8% portion, with a delay of 8°C. The residues of the modified samples were mostly higher than the pristine microsphere because of the inorganic incorporation of titanium dioxide nanoparticles (Ren et al., 2015).

3.5 Performance investigation of the performed samples

The DSC thermographs of PVA microspheres are shown in (Figure 20), and (Table 4) presents the analytical data including, the calculated melting and freezing latent heat values by integration of the peaks of DSC thermograms, the temperatures of the melting and recrystallization according to the first transition Tonset, the temperatures of the transition of the whole material as known by the peak temperature, and the calculated PCM ration accompanied by the encapsulation efficiency. Even so, the PVA polymer and titanium dioxide nanoparticles do not show any thermal behavior in the studied temperature range; the record of the stored energy reveals the PCM potential.

As is widely known, the PCM can absorb energy under heat treatment accompanied by a state

Figure 20. DSC thermogram of MSP, MSPTi in different ratios.

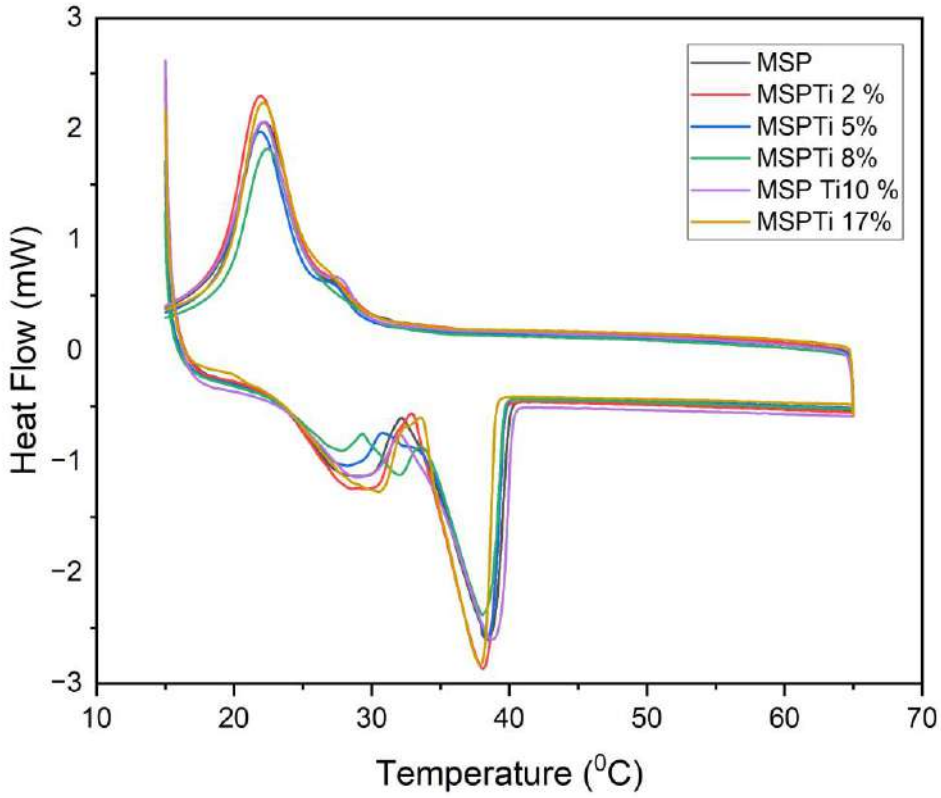

transition from solid to liquid in a specific temperature range, the stored energy per unit of weight identifies as melting enthalpy, oppositely at the range which the temperature under the melting stat, the PCM release the absorbed energy and rearrange to the initial state, this

phenomenon known as recrystallization, while the free energy identifies as recrystallization enthalpy. In the PCM material mixture, the designed model alters the PCM characteristic at different levels, depending on the nature of the elected material.

The first transition of PCM is set to a melting temperature of around 32.77°C. Meanwhile, all the performed samples exhibit a shift in the transformation peak of PCM toward a higher temperature. The increase is a reflection of nanoparticle addition. The maximal delay by 2°C is set in MSPTi 8%, while MSPTi 2% reveals a slight alteration in the melting temperature of PCM.

(Table 4) illustrate the enthalpies of PCM and the preformed samples. PCM reflects a melting and recrystallization energy of around 138.62 j/g and 78.53 j/g, respectively. The microspheres exhibit a diverse value that exposes a difference in the loading process; the fraction of titanium dioxide controls the change in the enthalpies. In the melting phase, the MSPTi 2% shows a high stored energy of 58.72 j/g, followed by the sample that is enhanced by 5%, beyond a defined portion, as much as the load in the nanoparticle, as much as the capacity reduces. The hybrid PVA samples of a further 5% demonstrate a lower absorbance capacity compared to the intrinsic microsphere.

The performance investigation of the microspheres was necessary to clarify the variability of the recorded enthalpies. The encapsulation ratio (R) and the encapsulation efficiency (E) are calculated using the DSC measures given below:

$$R = (\Delta H_{m,cap} / \Delta H_{m,pcm})*100$$

$$E = (\Delta H_{m,cap} + \Delta H_{c,cap})/(\Delta H_{m,pcm} + \Delta H_{c,pcm})*100$$

$\Delta H_{m,\,cap}$, $\Delta H_{c,\,cap,}$ melting, and crystallization enthalpy of the capsule.

$\Delta H_{m,\,PCM}$, and $\Delta H_{c,\,PCM\ are}$ attributed to the melting and the crystallization enthalpy of the PCM.

The ratio results reveal the main reason for inequality in storing energy, the decrease of the absorbed energy in hybrid samples by order 2, 5, 8, 10, and 17 % MSPTi corresponds to the reduction of the PCM portion. The encapsulation ratio displays that the enhancement of PCM loading related to the incorporation of nanoparticles by 2 and 5%, after these fractions, the effect is inverted to be harmful to the storage ability. The phenomenon can be explained by the fabrication process, as an increase in the number of nanoparticles, which affects the crosslinking process, and its rise goes on contradictory to the reduction of polymer fraction

which was responsible for the reticulation process, all these factors delay the polymerization, process which conducts to lose PCM proportional to the integrated titanium dioxide.

Based on the DSC results and the estimated PCM fraction, the polymer PVA is an optimal material for PCM encapsulation due to the low alteration of the PCM efficiency, especially in the case of nanoparticle integration, which enhances the polymer performance, increases the loaded PCM, and ameliorates the energetic absorbance capacity.

Sample	**Melting phase**			**Crystallization phase**			**PCM performance**	
	T_{onset} (°C)	**T_{peak} (°C)**	**ΔH_m (j/g)**	**T_{onset} (°C)**	**T_{peak} (°C)**	**ΔH_s (j/g)**	**R(%)**	**E (%)**
PCM	32.77	34.19	138.62	25.25	22.67	78.53	/	/
MSP	33.24	38.38	53.40	26.13	22.22	61.21	43.13	56.64
MSPTi 2%	33.09	38	58.72	25.8	22.04	69.70	47.47	63.5
MSPTi 5%	33.77	38.36	55.43	25.62	21.97	65.62	44.77	59.82
MSPTi 8%	34.13	38	50.83	26.08	22.55	65.75	41.05	57.61
MSPTi 10%	33.57	38.73	50.03	25.78	22.15	55.46	40.63	52.27
MSPTi 17%	33.62	37.82	43.67	25.83	22.21	58.12	35.27	50.30

Table 4. DSC analysis of microspheres MSP and MSPTi.

3.6 Thermal conductivity measurements

A thermal conductivity apparatus coupled with a steady-state technique is used to measure the thermal conductivity of bulk materials. The principles and equations are described in the previous Alginate chapter.

Instigate the small geometry of the preformed microspheres and to adjust the superficial contact between the apparatus and the microspheres, a matrix is modeled to adapt the surfaces of the cascade heater in the apparatus. The PCM matrix is engineered to have a high value of PCM near saturation state, while the other microspheres are designed to have a fraction of 33.7, 28.03, 28.29, 26.04, 31.78, and 27.55% assigned by order to MSP, MSPTi 2%, MSPTi 5%, MSPTi 8%, MSPTi 10%, MSPTi 17%.

Figure 21. thermal conductivity of PVA and modified PVA..

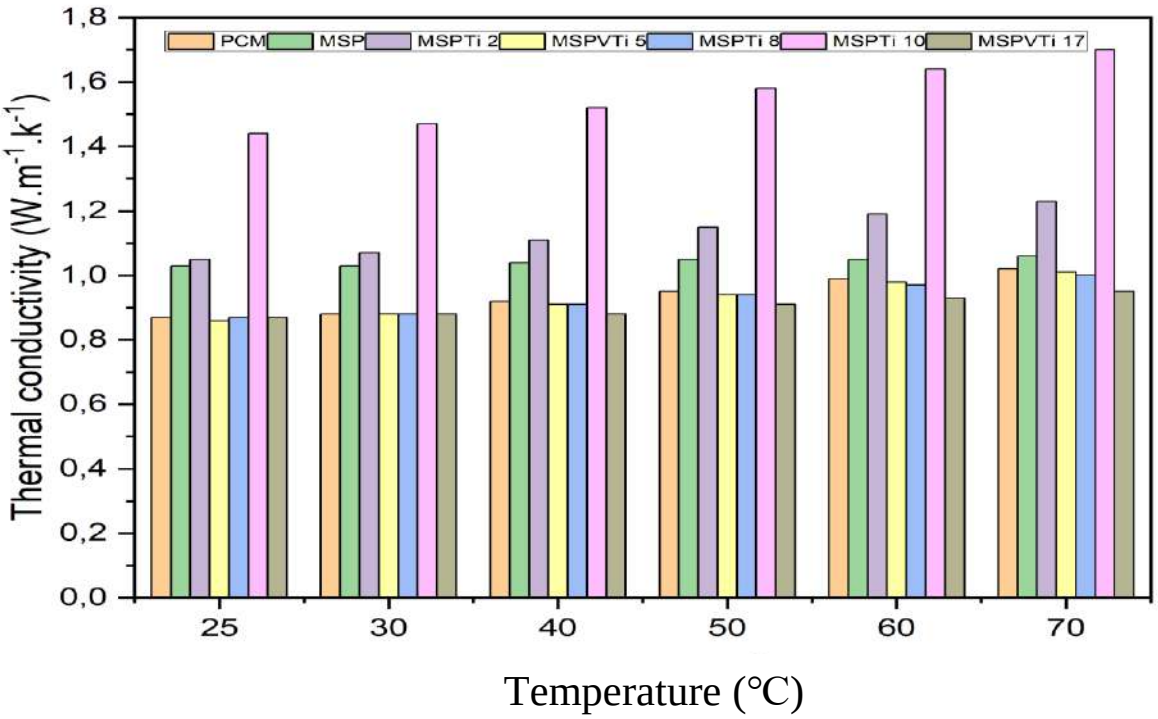

(Figure 21) present the thermal conductivity of the matrix designed by integrating the preformed samples as described above. The variety of the reading is based on the portion of microspheres inside the matrix, which gives a perception of the transfer behavior of the samples under heat treatment.

The measurement was accomplished at room temperature to investigate the effect of PCM in the solid state. On the other hand, a batch of high temperatures was executed to ensure the transition phase of PCM to the melt state and examine the change in the matrix.

At 25°C, the thermal conductivity records show notable diversity. The PCM matrix, along with MSPTi at 5%, 8%, and 17% exhibits nearly identical conductivity values close to 0.87 W/m·K. In contrast, MSP and MSPTi at 2% demonstrate higher conductivity, with values of 1.03 and

1.05 W/m·K, respectively. The highest conductivity is observed in MSPTi at 10%, which reaches 1.44 W/m·K.

All the matrix displays a similar profile as the temperature increases, as a consequence of the conductivity enhancement. Beyond 30°C, the rate of enhancement increases at different regimes compared to the faint rise measures at lower temperature; however, MSP, and MSPTi 17% reveal different behaviors that refer to the slow change in the thermal conductivity under heat treatment. The thermal conductivity enhancement is shown in (Table 5).

Temperature °C		**Kenh**					
		25	**30**	**40**	**50**	**60**	**70**
MSP	**(33.70)**	1.18	1.17	1.30	1.1	1.06	1.03
MSPTi 2%	**(28.03)**	1.20	1.21	1.20	1.21	1.20	1.20
MSPTi 5%	**(28.29)**	0.98	1	0.98	0.98	0.98	0.99
MSPTi 8%	**(31.78)**	1	1	0.98	0.98	0.97	0.98
MSPTi 10%	**(27.55)**	1.65	1.67	1.65	1.66	1.65	1.66
MSPTi 17%	**(26.04)**	1	1	0.95	0.95	0.93	0.93

Table 5. Thermal conductivity enhancement microspheres PVA.

The samples majority exhibit an improvement in the PCM thermal conductivity at room temperature except for MSPTi 5%, above 30°C, the coefficient enhancement of hybrid microspheres decreases indicating the change in the PCM stat that is accompanied by heat absorbance. However, the MSP acts.

Differently to the hybrid matrix, and delays the decrease of the coefficient to 50°C, mainly due to the high fraction of PCM.

3.7 Results and Discussion

The polyvinyl alcohol encapsulation is carried out using the in-situ polymerization technique with an extrusion method using boric acid as a crosslinker. The fabrication process is executed with a target of generating a single microsphere by dropping the stable emulsion into concentrated boric acid. The purpose of the saturated acid is to trigger the boron diffusivity

within the emulsion droplet, by providing a charged environment wreathing the emulsion pebble, and ensuring a sufficient amount to compensate and endure the instantaneous consumption during the polymerization process.

Figure 22. Mechanism of PVA fabrication.

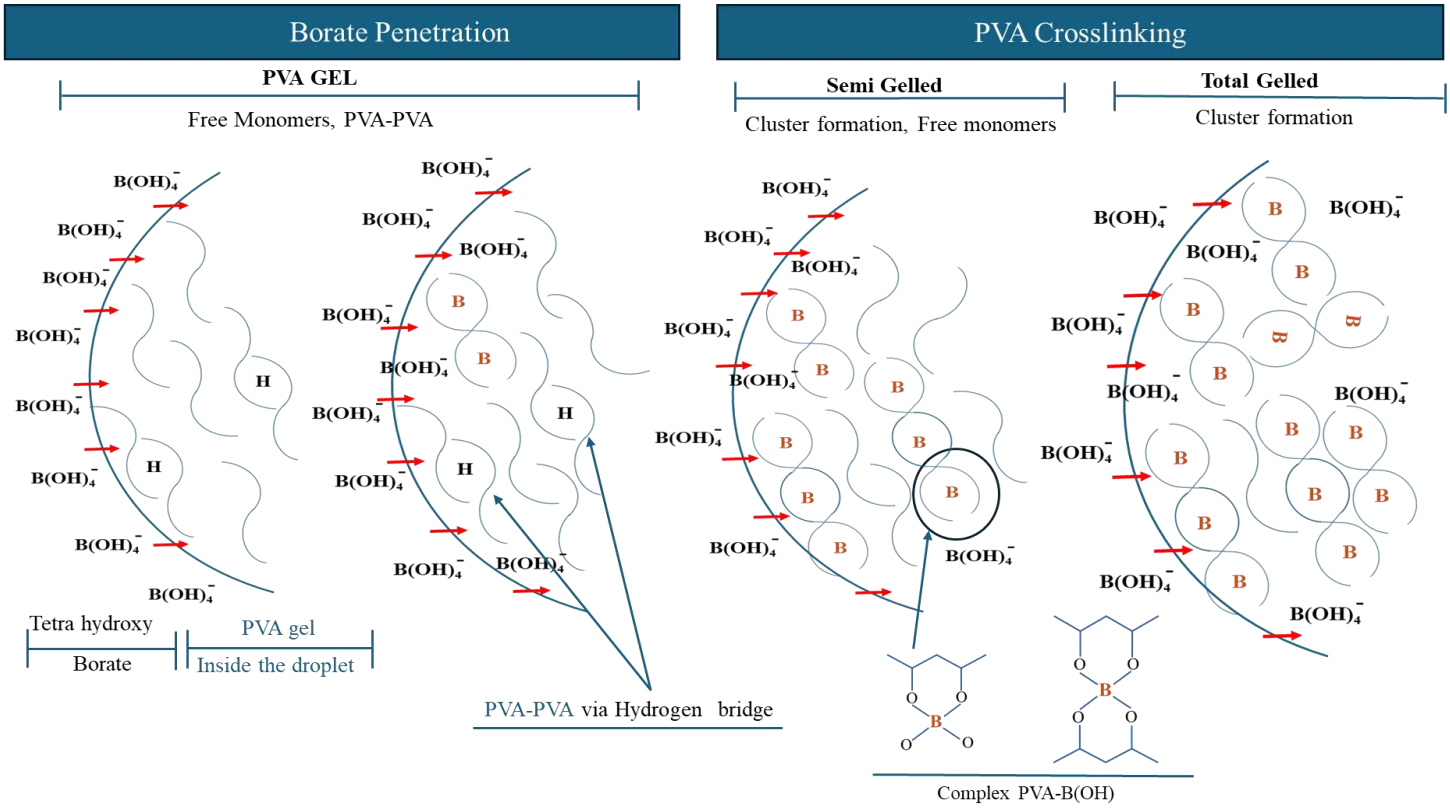

The emulsion obtained from the mixture of PVA and PCM, concomitant with the thermal fabrication conditions, tends to become thicker. This phenomenon might be due to the diverse origin of the PVA and PCM, which could explain the change in the viscosity of PVA gel, and more particularly induced by the nature of the PCM, which is a fatty acid of mono, di, and triglycerides complex that mainly fabricate of a direct esterification process between the fatty acids and glycerol, the latter element is widely studied as a plasticizer in PVA membrane fabrication. In the condensation phase, the emulsion pebble strengthens along with the polymerization time elucidating the trajectory of crosslinking which begins from the surface of the emulsion droplet to the core, thus ensuring the linkage of boron with the active sites of the emulsion constituents, (Hashimoto & Furukawa, n.d.) denoted, the polymerization as a lent process that requires 24 hours to achieve the reticulation of PVA. Herein, the linkage

is confirmed in (Figure 12), which illustrates the accomplishment of the condensation process. This outcome reveals the penetration of the boron into the bead emulsion, the diffusion was guided by the small radius of the crosslinking agent, and the porosity of the PVA gel. The linkage process in this study is the outcome of three possibilities: the intramolecular of the PVA chain, the intermolecular of PVA moieties, and the interaction between the boric acid and PVA, and could be counted, the possibility of interaction between the PVA chains and nanoparticle titanium dioxide in the hybrid microspheres.

The characteristic absorptions of the preformed microsphere MSP (Figure 18) Confirm the interaction between the PVA and H_3BO_3 by the emergence of the B–O–C bond as described before and validated in other research findings, while in the profile of MSP, the bond C–O–C at 1030 cm^{-1} was missing compared to the PVA cross-linked profile in the literature, (Koysuren et al., 2012) Clarify the absence of this frequency in the fabrication of the polyvinyl borate, referring to the conversion of the C–O–C bond to B–O–C, and conclude that the enhancement of PVB assembly affected the PVA characteristics. (Dodda et al., 2015) Emphasizes the insufficient presence of the C–O–C bond to the reduction of hydroxyl intensity, referring to the relation between these two types of link, the same outcome is explained by (Kotoky & Dolui, 2004) conclude that the incorporation of silica alters the absorbance frequency of OH, which proves the linkage through the polar hydroxyl group by a hydrogen bond. The same phenomenon is pronounced in this study, especially the decrease in the absorbance of the OH group in the MSP spectrum compared to the SP.

The crosslinking of the PVA and the boric acid interacts at two levels in the physical process, which is managed by the anion exchange membrane due to the hydroxyl group on PVA and the boric acid through hydrogen bond, and in the chemical process, which results from a covalent liaison. The physical interaction is a spontaneous process acquired without any intervention, contrary to the chemical, which is triggered mostly by a catalyst or under annealing treatment. (Choe et al., 2024) reported that the addition of hydrochloric acid affects the water portion on the final product of PVA-BOH by 55% compared to the precursor, which creates compact PVA moieties that enhance the interaction between the polymer and the crosslinking agent. (Lambertini et al., 2024) Studied the fabrication of crosslinked PVA polymer through the intervention of boric acid at ambient temperature, the FTIR specter of the preformed sample exhibits the presence of BOH liaison which confirmed the accomplishment of the crosslinking process, while BOC frequency appeared in (Shawgi et al., 2017) research, where the PVB hydrogel was formed by blending the PVA polymer with boric acid, the process was carried

out in a hot environment under 80℃. Both studies accentuate the impact of heat treatment on promoting intermolecular interaction, (Filippo et al., 2015) allude to the same results, explaining the emergence of the C–O–Ti bond in the PVA-TiO_2 FTIR specter to the heat treatment process, incentivizes the junction of hydroxyl groups in titanium dioxide and the PVA gel, through extracting water molecule, which widely known as dehydration process.

The FTIR spectrum of the hybrid microsphere shows a shift or reduction in absorbance of some frequencies after the addition of titanium dioxide compared to the pristine microsphere and exhibits new absorbance bonds. The alteration made by the incorporation of titanium dioxide indicates an interaction between the nanoparticles and the PVA gel. (Surkatti et al., 2024) indicating that the affinity of PVA and oxide metal referred to the interaction between the hydroxyl group and the oxide boundary of the nanoparticle, (Choe et al., 2024) mention the strong interaction between the Ti-OH groups on the surface of TiO_2 nanoparticles with the hydroxyl groups on the PVA moieties. (Habiba et al., 2017) Interpreted the shrinkage of the CH_2 absorbance bond according to 1375 cm^{-1} frequency to the linkage of titanium dioxide to the active sites of the polymeric membrane, which effectuated over the OH link. All these studies confirm the hypothesis of the interaction between the nanoparticles and the PVA polymer.

The cross-section microgram of MSPTi (Figure.17) shows an agglomeration of titanium dioxide, which reveals the heterogeneity of nanoparticle dispersion.

Conceive to the stirring process and the faint portion in the sample, the nanoparticle cluster behavior might be attributed to their affinity toward each other or a reflection of exterior forces that sequestrated the titanium dioxide. (Sakarkar et al., 2020) Settled that the high PVA concentration affects the dispersity of titanium dioxide and referred to 7,5 % as an optimum

Fraction to maintain the homogeneity of the membrane, herein the suppress network that hinders the uniformity was excluded lean on to this study, while (Habiba et al., 2017) highlighted the impact of the Van der Waals forces in the agglomeration of titanium dioxide particles which prohibit the dispersity and display a cluster onto the surface of the samples, (Koysuren & Koysuren, 2018) explaining the aggregated TiO_2 structures as an assembly of dozens of nanospheres, and this phenomenon shows the affinity of the TiO_2 nanoparticles toward each other. (J. J. Kim & Choi, 2021) describes this phenomenon as a compilation of a layered structural arrangement of the different titanium dioxide types (Jordan et al., 2016) mentioned that there is no specific reason for the self-assembly of rutile to generate a multilevel branched structure, meanwhile, alluding to the effect of the acidic environment on triggers the

collapse of the nanoparticles and forming a layered arrangement, and confirming the entanglement and branching of the titanium dioxide even at low concentration in highly acidic environments revealing a complex crystallographic interconnected.

Figure 23. Mechanism of modified PVA fabrication.

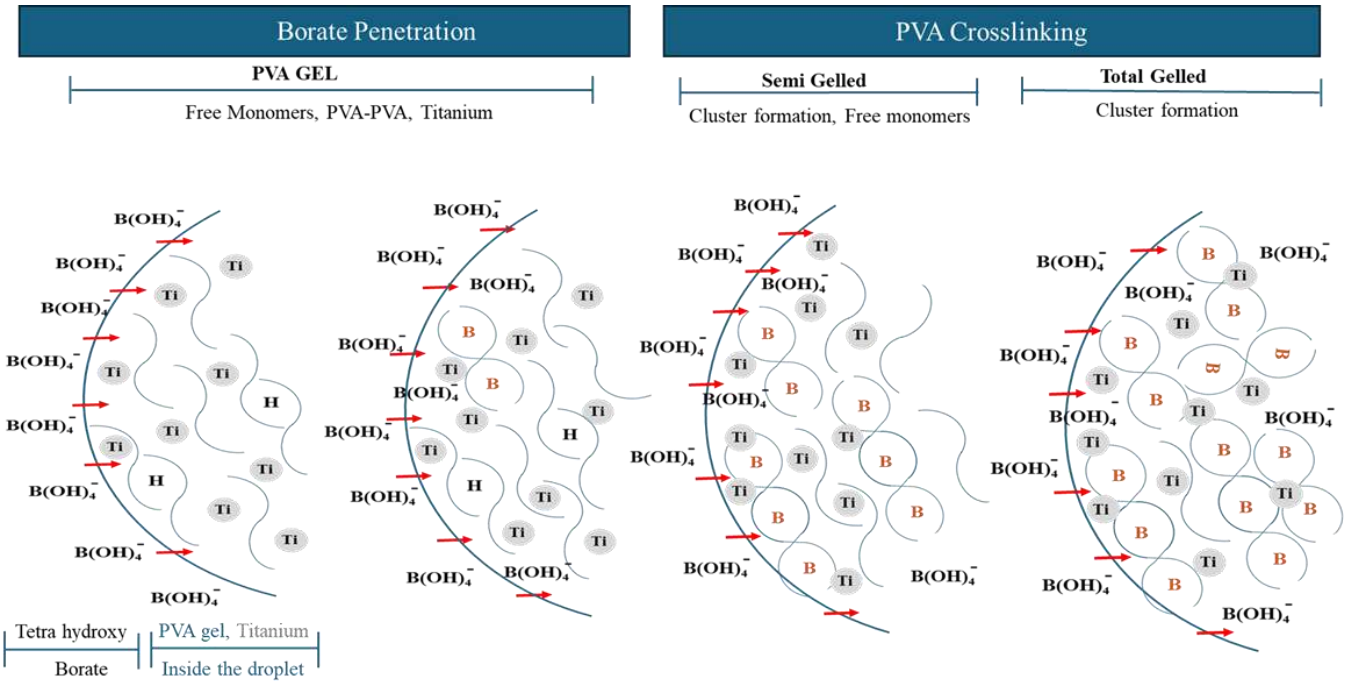

On the other hand, (L. Li et al., 2021) Investigate the effect of water in the PVA gel, referring to the Intera and intermolecular, which are inversely proportional to the water fraction. The rise in the water portion (>5wt %) hinders the self-interaction of the PVA chain and reduces the hydrogen interaction between the PVA moieties by replacing PVA-PVA hydrogen bonds with PVA-water hydrogen bonds, based on this research the intramolecular PVA, and the intermolecular interaction between the PVA chains was eliminated in this study as a consequence of high water fraction takes in account the selected PVA concentration of 7 (wt/v), which encourage a stretching conformation of polymer molecules thus to the low amount of connected chains.

Depending on the aforementioned, the mechanism of fabrication of MSP begins with the interaction of PVA and the hydroxyl group of water during the dissolution process which instantaneously changes to interact with the boric acid due to the high affinity toward the hydroxyl group and the fragility of the hydrogen bond between the polymer and the water, the reaction between PVA and H_3BO_3 involves the hydroxyl groups on the molecule of PVA

reacting with H_3BO_3, the complexing agent engages in polar bonding through hydrogen bond and formed a covalent bond promote by the heat treatment, which affects the elasticity phenomenon and improve the strength of preformed microspheres as result to reducing the mobility of PVA chains (Park et al., 2022), on the other hand, the hybrid microspheres has a different arrangement, the intermolecular interaction of PVA and a water molecule is hindered by the incorporation of titanium dioxide nanoparticles, and the crosslinking progression promotes the bridge behavior (Surkatti et al., 2024) between the metal and the polymer due to their ability to react through the hydrogen bond, the new cluster minimizes the space between the PVA molecules, and enhance the performance of PVA reticulation after inducing it to the boric acid for an optimal period, herein, the diffusivity of the saturated boric acid reinforces the unreacted titanium dioxide to withdraw into the microsphere center and agglomerate making macro-crystallographic aggregate.

The thermal investigation of prepared specimens by TGA analysis shows an enhancement in the stability of the hybrid microspheres MSPTi (D. Wang et al., 2024) compared to the pristine sample MSP for a certain level of reinforcement, while the gradual rise after a defined portion drastically affects the behavior of composite samples. The addition of titanium dioxide is selected due to its high thermal stability, the optimum fraction of nanoparticles acts as a bridge between the PVA chains and forms a long compact chain that fortifies the sample and increases the required energy that triggers the chains movement (Ahmad et al., 2014), while the increase in the nanoparticles portion to a certain level affects the structure of the polymer and hinders the polyvinyl alcohol intermolecular moieties that affect the reticulation and enhance the aggregates, which directly perturb the stability. Herein, the suitable metallic fraction that shows a thermal consistency in the TGA examination is MSPTi 5%.

Nevertheless, the comparison of the SP sample to the pristine MSP, depending on TGA results, shows a decrease in the decomposition temperature of MSP in contrast to the precursor prepared without the PCM addition (SP), and owing to the fact that the reduction in stability is related to the low PVA fraction chains which are proportional to the degree of reticulation, and since 40% of emulsion is PCM, the decrease in their stability is acceptable considering the PCM as inert compound and have low thermal stability. On the other hand, the precursor shows continuous degradation until the decomposition temperature, this phenomenon is attributed to the amorphous structure caused by the reaction of acid boric with PVA polymer, which hinders their crystallinity, in other words, prevents the self-interaction of PVA and as a consequence increases the domination of amorphous assembly (Dodda et al., 2015) (Park et al., 2022).

However, the MSP and MSPTi exhibit a constant profile before reaching the degradation step; the steady behavior indicates high crystallinity (Koysuren & Koysuren, 2018), Based on the previous description, we could consider the MSP and the MSPTi more stable than SP.

The thermal storage capacity was investigated using the DSC apparatus, revealing the same pattern as thermal stability. The hybrid microspheres attributed to 2 and 5% of TiO_2, have higher storage according to the melting enthalpies compared to the rest of the samples including the pristine specimen MSP, despite the reinforced samples showing delay on the onset temperature which increased by rising the amount of titanium dioxide, the microspheres that sequestrated more than 5% of metallic nanoparticles show a weak capacity inferior to the MSP, concluding that the incorporation of nanoparticles is inversely proportional to the storage capacity after 5%. Concerning the crystallization enthalpies, the hybrid samples of 8% show divergence behavior in the energy release, which was found to be higher than the pristine sample compared to the results of the melting enthalpy, which revealed inferior absorbance energy versus the non-modified microsphere. This critical behavior gave MSPTi 8% the privilege to enhance the encapsulation efficiency to exceed the MSP performance. In general, the melting enthalpy is related to the nature of the sheath and the amount of PCM in the sample, the PCM ratio gives a perception of the performance of the fabrication method. Depending on the results of (Table 4), the PCM ratio is in line with the melting enthalpies, thus authenticating the enhancement properties of microspheres by nanoparticle addition, referring to the effective fraction for a high PCM encapsulation according to integration of 2% of nanoparticles, followed by the 5% fraction then tracked by the non-modified sample, as mentioned before the elevation of titanium dioxide of more than 5% decreases the enthalpy and as a consequence reduces the ratio of the PCM.

In thermal stability, the hybrid specimen of MSPTi with 5% exhibits higher consistency versus the sample of 2%, while in the storage energy, the microsphere of 2% shows more capacity compared to the enhanced sample of 5%, generally the energy storage related to the amount of PCM loaded and to the fabrication process, herein, the two samples produced at the same mechanism, thus the difference is in the polymerization process, as described before the titanium dioxide instigate the bridge behavior with PVA moieties which accelerate the condensation mechanism and prevent the loose of the core during the fabrication process and at the same time enhance the thermal stability of the microsphere by enrich the crystallinity of sample, this outcome is reinforced by the results of the crystallization enthalpies which rise gradually by rising the nanoparticle amount until 8% and confirmed by the TGA profile of

hybrid samples of 5% and 2%, depending on the aforementioned, the decrease in the PCM ratio in MSPTi 5 sample is related to the decrease in the PVA chains regarding to the fabrication method, so the increase in the incorporation of the nanoparticle assess the decrease in the PVA fraction, as result the incorporation of TiO_2 by 5% could enhance the thermal stability and the enthalpy of crystallization because both of them depend on the crystallinity, at the same time as result of the low PVA moieties the sequestration of the PCM decrease since the majority of the PVA make bridge with the nanoparticles.

Chapter 4. WOOL MATRIX

4.1 Preparation of wool powder

Sheep wool fiber is widely known to be difficult to grind and requires high energy to break into small fragments. The endurance to breakage exposes the high mechanical resistance and elongation at break. Indispensable pretreatment is involved to facilitate the mechanical process and reduce the cost.

4.1.1 Wool powder preparation

The dried wool fiber underwent several washing cycles with distilled water, was chopped into spinets, and treated with hypochlorite solution at 0.5% concentration for different soaking periods, 2, 4, 7, 9, 14, and 24 days, at the end of treatment the immersed fibers dehydrated to eliminate the excess of moisture after rinse it again with pure water.

Figure 24. Wool powder process.

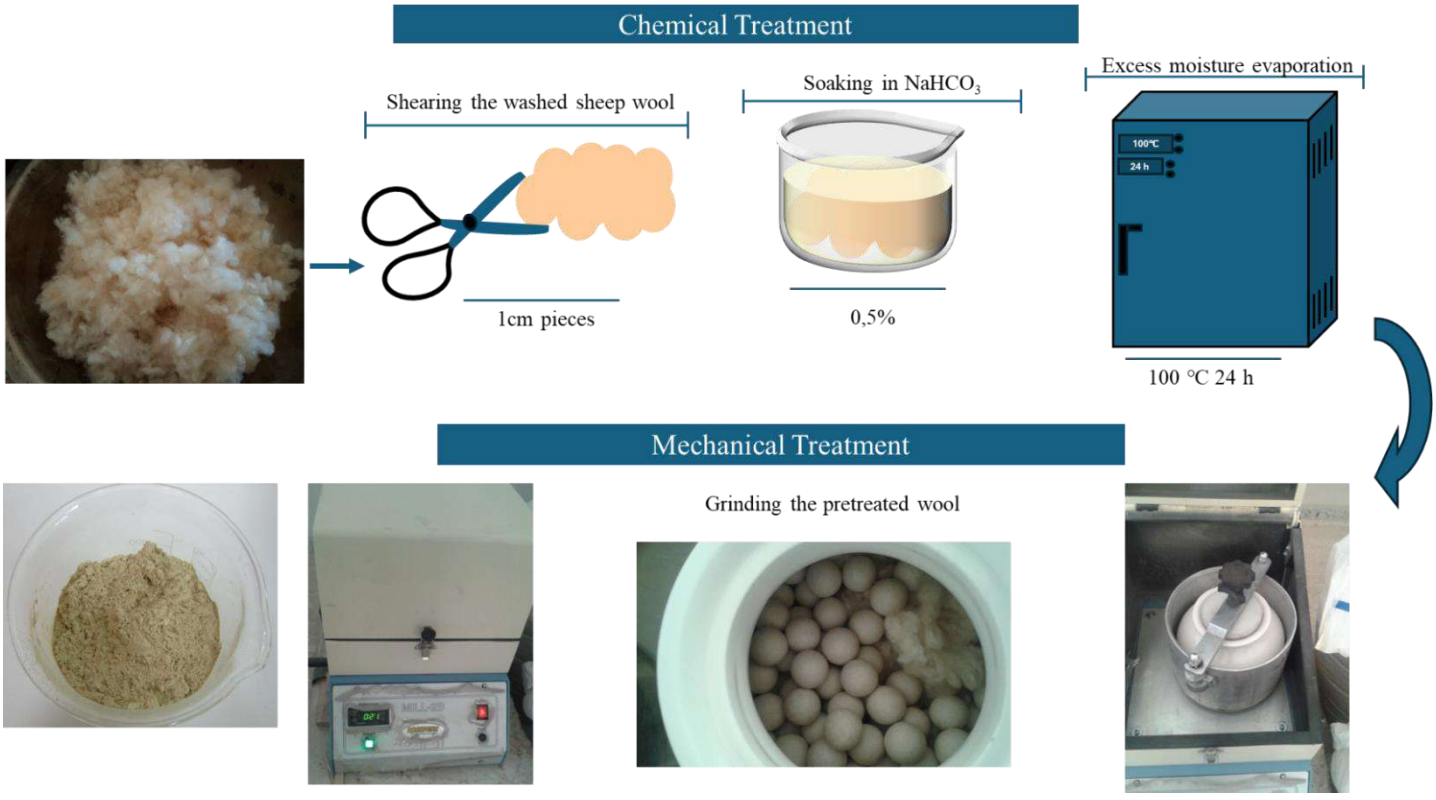

The powderization process of treated spinets is carried out using a ball mill apparatus, The mechanism is based on crashing the material in a sealed container between the collided balls

during the rolling process, the procedure was carried out for 4 minutes and repeated four times to prevent the damaging of the wool by the rising of temperature during balls collision and to ensure the manufacturing of the small size of wool, the process illustrated in (Figure 24). It is worth noting that the hypochlorite used in this study is a commercial bleaching agent. In Algeria territory the concentration is articulated by chlorometric degree (°Chl), and to simplify the work, the conversion to active chlorine (c.a) is effectuated following the equation below:

1°Chl = 0.3 % c.a

4.1.2 Shape-stabilized wool

The wool particles are fabricated using the shape-stabilized method. The procedure is based on integrating the modified wool (wool powder) into a polymeric mixture (Figure 25). Three types of specimens were fabricated. The control sample was obtained by entrapping the PCM into the wool powder to obtain dispersed saturated particles, this type noted under the label WP.

Figure 25. Procedure of the shape stabilized wool particles.

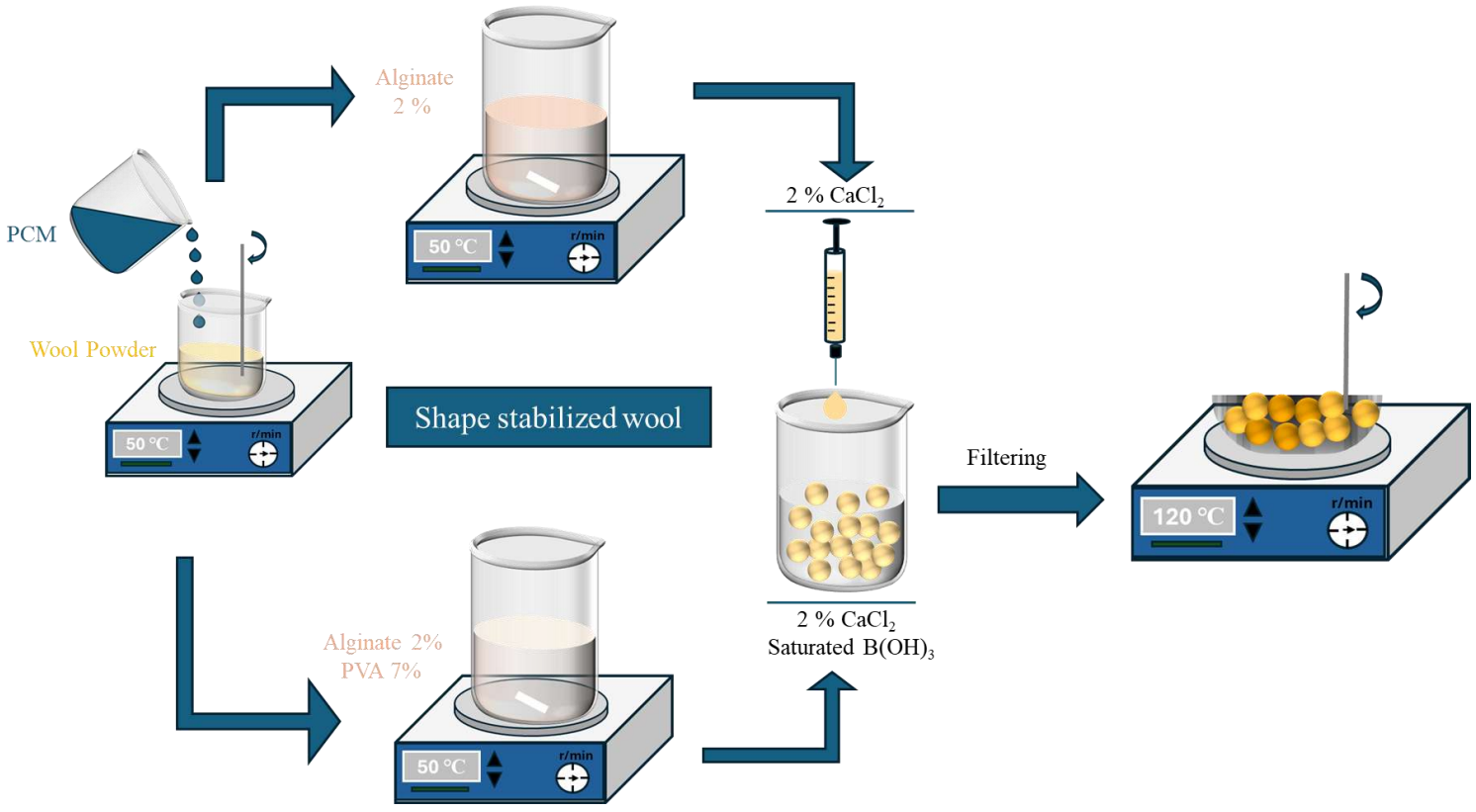

The second type was prepared by integrating the wool and the PCM into an equal extent of sodium alginate at a concentration of 2 (w/v) and PVA at a concentration of 7(w/v), the final

stabilized shape is accomplished after hardening the emulsion into a crosslinking bath of an equal portion of saturated boric acid and calcium chloride at a concentration of 2 % (w/v), a spherical morphology received by extruding the emulsion through a syringe into the crosslinking agent overnight to ensure the reticulation process, the final product labeled WPPA. The last group was obtained in the same procedure, by blending the wool and the PCM into alginate polymer at a concentration of 2%(w/v), the process was based on dropping the mixture by a syringe into calcium chloride at a concentration of 5 % (w/v), the preformed sample noted as WAP. The material fraction is similar, which is around 22 % for PCM and around 11% for wool powder. The powder wool used in the preparation of particles is collected after 7 days of treatment. it is worth noting that the powder can absorb double its weight.

The final step was to subject the preformed samples to a heat treatment to eliminate the excess water and consolidate the wool particles. The technique consisted of heating the hydro particles to 100 °C for 10 minutes.

4.2 Morphology

The (Figure 26) shows the preformed wool powder (a) of the collected fiber after 7 days of immersion.

Figure 26. photographic image of, a. the powder sheep wool, b. hydro-stabilized shape wool, c. dried stabilized shape wool.

The sample appears yellow which demonstrates the impact of the chemical treatment, despite the majority of the sample having spherical-like geometry while a certain amount maintains a micro-fibrous morphology with length equal to or inferior to 1 mm, the micro-fibrous affects the dispersity of the sample and instigates the affinity between the micro-powder, this phenomenon could be controlled through sieving technic or repeating the grinding mechanism to restrict un optimum size and achieve homogenous particles. The hydro wool particles (b) have spherical geometry with a range of diameter varied from 4 to 5 mm, this morphology lost concomitant with heat treatment and the particles collapse at themselves to adjust and occupy the inner space of the evaporated water, thus the particles transform to aggregate form, the alteration in shape induced by the evaporation indicate a significant water fraction, resulting a reduction on the diameter where the dried particles expose 3 mm.

4.3 Chemical properties of the powdered wool and the native fiber

The chemical characterization was investigated using ATR-FTIR spectroscopy. The specters displayed in (Figure 27. a) were performed to identify the chemical transformation that permeates the wool transition from the elongated shape in the fiber form to the micro powder, the configuration of the wool fiber, the chemically treated fiber, and the wool powder exhibited some differences.

Figure 27. FTIR of, a. wool fiber and powder, b. wool/PCM particle.

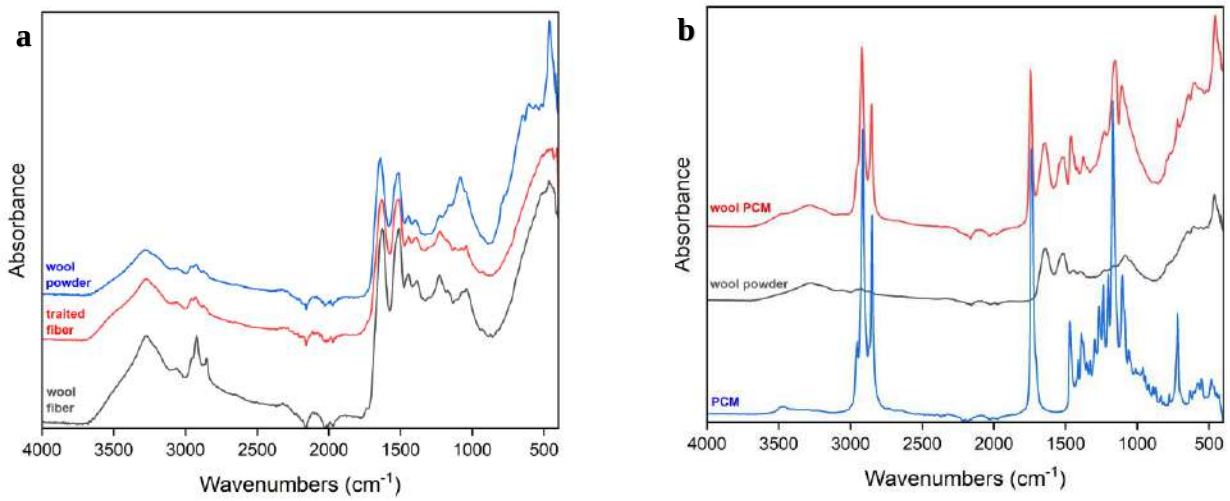

In general, almost all the peaks decrease in each step, wherein the treated fiber exhibits a reduction in absorbance peaks, which is reduced more in the powder profile, except for some peaks that indicate the achievement of the target. The fiber wool is keratin, so the composition assesses the presence of amide groups and amino acids.

The raw fiber configuration displays a broad peak at 3272 cm^{-1} attributed to N–H in amide A (Hameed & Guo, 2010) meanwhile (Wojciechowska et al., n.d.) point out the possibility of including the S–H bond beside N–H, the stretching vibration at 3060 cm^{-1} represents the amide B, the sharp peak at 2922 cm^{-1} exposes the symmetrical stretching vibration of CH3, while the twin small peaks at 2851cm^{-1} reveal the symmetrical stretching vibration of CH2 (Xu et al., 2006)The amide I is identified by C–O bond, while the amide II is recognized by N–H appear at the frequency of 1625 cm^{-1}, also identified by the peak at 1509 $cm^{-1,}$ exposing the bending of N-H (Khosravi & Montazer, 2023) (Hameed & Guo, 2010)The stretching vibration recorded at 1446 cm^{-1} is related to the linked C-N that connects to the amide II (Rather et al., 2015) (Wojciechowska et al., n.d.)The third type of amide III emerges at the vibration 1039 cm^{-1} (Khosravi & Montazer, 2023) and could be recognized by the C–N stretching bond at 1230 cm^{-1}, while (Rather et al., 2015) cited that the range 1300-1220 cm^{-1} is attributed to the amide III.

The disulfide bond is responsible for the wool's stability and could be placed at 1170 cm^{-1} and 1120 cm^{-1} (Wen et al., 2010)Another bond related to S-O appeared at 465 cm^{-1} frequency.

The majority of peaks in the specters of treated and the powder wool shifted towards the higher frequencies, with some exceptions as the stability of the amide II peak and the decrease of the disulfide bond from 1170 cm^{-1} in raw to 1121 cm^{-1} in the oxidized state and rise again to 1162 cm^{-1} in the final product. (Xu et al., 2004) allude to the proportional relation of the S-C intensity bond at 1084 cm^{-1} and the polarization degree, while (J. Fan & Yu, 2012) assumed the intensities at 1162 cm^{-1} and 1084 cm^{-1} refer to the S=O bond of the oxidized cystine.

The broad SO bond in fiber deconvoluted to 477 cm^{-1} and 439 cm^{-1} in treated wool and was clearer in the powder profile with a range of bonds vibrated in weak intensity at 648 cm^{-1}, 603 cm^{-1}, 555 cm^{-1}, while a strong sharp peak emerges at 462 cm^{-1} (˙bieta Wojciechowska et al., n.d.)The emergence of peaks cascade ensures the oxidation of wool fiber into small fragments.

The infrared profiles of wool powder and PCM, and the blended wool/PCM, were executed to distinguish the successful sequestration of the absorbed PCM inside the wool and discover the compatibility of the two compounds. It is obvious from (Figure 27. b) that the spectrum of the wool/PCM is the convolution of the primary precursors, in other words, presenting the sum of

the profiles, wool and PCM. Despite the majority of the peaks being a slight shift as a consequence of the blending process as CH2, CH3, and C=O bonds in the PCM, a considerable shift toward high frequencies was recognized at 1524 cm^{-1} related to amide II combined by a reduction in the vibration at 1379 cm^{-1}, 1151cm^{-1}, 454 cm^{-1}, while the bond at 603 cm^{-1} exhibit a strong sharp peak, as well as the PCM, the peak at 719 cm^{-1} barely appears, based on aforementioned, which strongly confirmed the interaction between the wool powder and the PCM.

4.4 Thermal enhancement investigation of wool powder

The thermal stability is an important characterization to identify the material improvement or to localize the defect of the generated or hybrid element. (Figure 28. a) shows the produced particles by the powder obtained at different levels of immersion that express the progression of the chemical treatment, which is responsible for the degree of wool powderization.

Figure 28. TGA of, a. WPA at different treatment levels, b. wool particles at different methodologies.

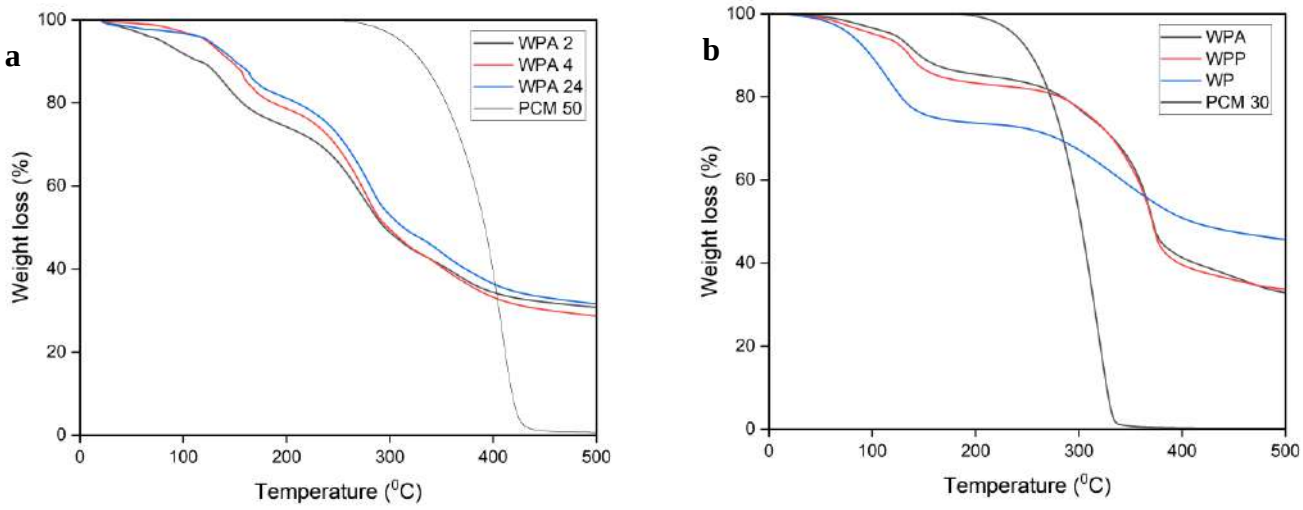

The selected samples are according to 2, 4, and 24 days of oxidation. The particles have the same attitude of degradation and consist of three phases, the first begins at room temperature to 150°C, this kind of loss is recognized as the dehydration process where the excessive water evaporates, the particles of 4 and 24 days have similar behavior which different to the treated sample of 2 days, the loss of weight of the two mentioned specimens was lower than the other, where is approximate to 10 and 15 respectively, the second slope is started earlier concerning the WPA 2, and fellows by WPA 4 and tracked by WPA 24 after 1°C, this stage emphasizes

the evaporation of the PCM 30 and decomposition of the wool and the polymeric matrix, and the last stage include further pyrolysis of the decomposed materials, the residues from the pyrolysis is around 30 %, referring to the wool fire retardancy potential, which indicates that

The intrinsic properties of wool aren't affected during the chemical treatment or the milling process even after 24 days. It is evident, that the shape-stabilized wool enhanced the PCM stability by delaying the decomposition temperature, indicating the immobilization of PCM.

(Figure 28.b) illustrate the profiles of different methodologies that were tracked to discover the best trajectory to fabricate an optimum shape-stabilized wool. The profile labeled WAP is saturated wool stabilized by alginate polymer, WPPA is saturated wool stabilized by PVA/ALG polymer, and the last WP is PCM blended into a wool matrix. The comparison of the three specters reveals that the WAP and WPPA have sensibly the same trend, while WP shows less stability in front of the two other samples, In general, the thermal performance has two degradation steps, the first occurred when the water was eliminated, the WP demonstrate loss of 25 % and 10 % for the rest specimens, the second pyrolysis includes the degradation of the polymer and the PCM in the three particles, while the WP destabilized earlier and display a lower loss compared to the other particles, this outcome indicates that the methodology isn’t effective as the two trajectories, considering the identical conditions especially the amount of the PCM which highlight the behavior of WP to leak the PCM more than WAP and WPPA and that be clear in its TGA results.

4.5 Performance study of the wool matrix

(Figure 29) illustrated the DSC thermographs of shape-stabilized wool particles and (Table 6) resumes the analytical information of the melting and recrystallization cycles, emphasizing the enthalpies, the onset temperatures that explained the lowest value that triggered the transition of phases, the peak temperatures that revealed the temperature at which the transition of the entire material occurred, and the results of the encapsulation efficiency go with PCM ratio. It should be pointed out that the polymers, including the alginate, the PVA, and the wool, don’t show any transition combined with an energetic effect in the examined temperature interval, referring to the energetic recorded behavior exposing the PCM potential.

Depending on the illustrated DSC curves, the PCM's ability to absorb and release energy is much higher than the shape-stabilized wool particles, referring to the alteration made by the

modeled material, which affects the energetic behavior of the PCM, the melting enthalpy exposes the required energy to achieve a complete transition of the PCM from the solid state to

Figure 29. DSC of, a. wool/PCM, b. various polymer.

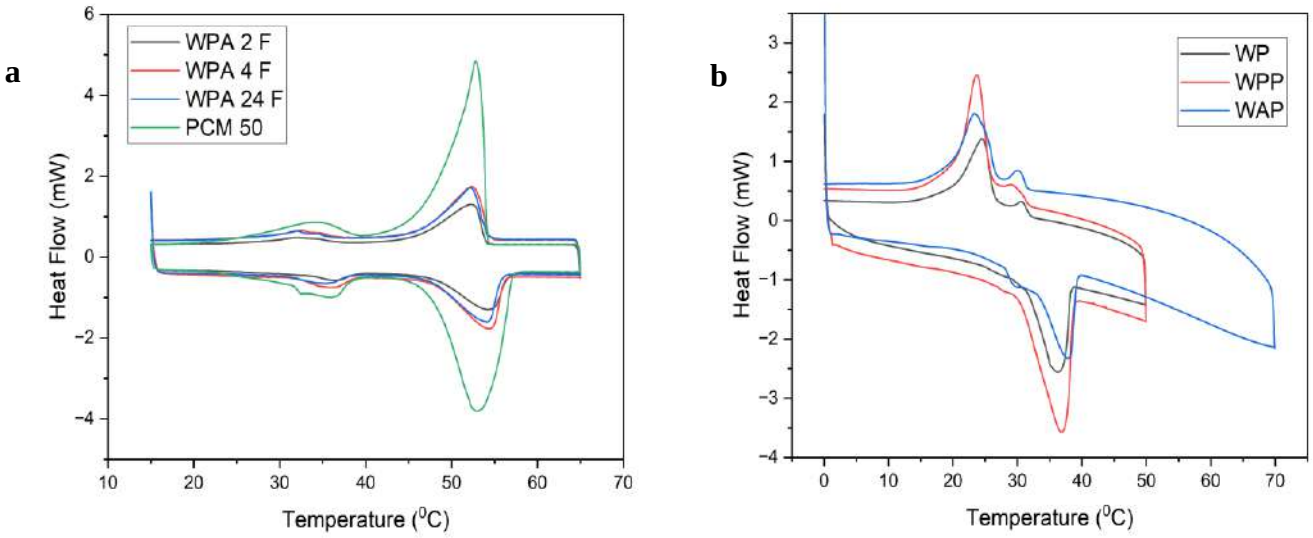

the liquid under heat treatment, the same concept applies to the recrystallization enthalpy but in the inversed approach where the PCM recuperates the initial state by releasing the absorbed energy, the understanding of the PCM principle alludes to conceiving the change in the energy might refer to the low PCM fraction in the particles.

Depending on (Table 6) and (Figure 29. a), the WPA 2 and the WPA 4 samples delayed the melting temperature of the embedded PCM by 1, 20 ℃, and 1℃ respectively while the WPA 24 enhanced the transition and declined towards the low temperature by 0.23 ℃, in the relax phase the record results is sensitively similar, The WP4 improve the crystallization of the PCM by 0.14 ℃ meanwhile the WPA24 and the WPA 2 samples relate the solidification of the core by 0.07 and 0.28 ℃ respectively. Alternatively, the WPA 4 shows a higher absorbance capacity in the three samples by 38.09 j/g while the PCM ability is found to be 138.62 j/g, contradictory to the WPA 2 which releases more energy compared to the studied specimen at 41.81 j/g and the PCM exhibit 141.84 j/g, in term of PCM ratio the WPA 4 retain more extent comprise 27.47 % but the encapsulation efficiency arises to 28.27 % in the WPA 2. Despite the modification being chaotic, especially in the transition range of temperatures and including the variation of the enthalpies, it nevertheless still gives a concept of the microscopic interaction and the overlapping of characteristics of each other.

The energetic performance of the different methodologies was investigated and illustrated in (Figure 29. b) and (Table 6. DSC analysis of shape-stabilized wool particles., the WAP and the WP samples elevate the transformation temperature towards 0.39 ℃ and 0.71 ℃ in order, while the WPPA acts differently and accelerates the PCM change by 2.08 ℃, concerning the crystallization process the WP and the WPP have a similar trend to intensify the solidification process, inverse progression note by the WAP where the decrease in the realized absorbed energy was 0.85 ℃ versus the intrinsic PCM temperature. The PCM used in the formulation of the samples has a melting enthalpy of around 138.62 j/g and 78.53 j/g according to the crystallization enthalpy, the enthalpies comparison of the three specimens elucidates the prevalence of the WPPA by 30.69 j/g in the case of the absorbed energy, however, the WAP showed the maximum capacity to release the previously absorbed energy quantify by 24.64 j/g.

Sample	**Melting phase**			**Crystallization phase**			**R**	**E**
	T_{onset} (℃)	T_{peak} (℃)	ΔH_m (W/m.k)	T_{onset} (℃)	T_{peak} (℃)	ΔH_s (W/m.k)	(%)	(%)
PCM 50	47.87	52.83	138.62	54.12	52.93	141.84	/	/
WPA 2	48.26	54.26	37.49	53.94	52.29	41.81	27.04	28.27
WPA 4	48.01	54.26	38.09	54.26	52.40	39.28	27.47	27.58
WPA 24	47.64	54.07	34.81	54.05	52.25	35	25.11	25.14
WAP	33.16	36.5	35.10	24.4	24.90	24.64	26.59	29.52
WP	33.48	38	16.88	26.42	23.2	21.3	12.78	18.87
WPPA	30.69	36.8	35.40	25.78	23.70	24.56	26.81	29.63

Table 6. DSC analysis of shape-stabilized wool particles.

A translation of disproportion results is dependent on the first position on the interaction of the materials and the fabrication methodology, the delay in the transition temperature of the PCM in WPA 2 and WPA 4 is probably due to the fraction of the crystal and amorphous structure affected by oxidation process while the reduce of the temperature recorded at WPA 24 revealed the strong interaction between the wool and the PCM since the excessive chemical process, however, the energetic performance is proportional to the fraction of the PCM in the sample which directly related to the fabrication methodology, the WPA 4 expose the higher ratio

around 27 %, despite the first fraction of 22 % the WPA 24 exhibit adequate portion compared to the other samples this outcome reinforces the interaction hypothesis.

Concerning the optimum methodology, the polymer consolidates the wool particle and improves the energetic efficiency, while no considerable impact between the alginate polymer and the matrix of the alginate and the PVA.

4.6 Thermal conductivity analysis

The wool sheep fiber is widely used and integrated into fields that require minimizing the heat absorbance or delaying the heat transfer rate. In this section, a thermal conductivity investigation of the wool powder is effectuated to discover the effect of the chemical and mechanical treatment on the thermal performance of wool. The steady-state technique is applied to measure the conductivity through a thermal conductivity apparatus. The principles and the equations are described in the previous alginate chapter.

Based on cascade heater geometry, the matrix wool is fabricated to maintain the diffusion of the heat flux transmission by adjusting the superficial contact between the apparatus and the samples. Besides the PCM matrix, which is modeled to have a high extent of PCM, near saturation state as mentioned before, two other categories were executed to better understand the performance of the specimens. The first category was carried out to distinguish the influence of extending the chemical treatment on thermal properties, the fraction of wool powder in the matrix is given as follows, the powders collected after treatment of 1, 2, 4, 7, 9, 14, and 24 days were integrated to designed matrix in a fraction of 25 %, 29 %, 26 %, 25 %, 25 %, 27 %, and 24 %.

The AWP matrix is modeled at a fraction of 36 % while the WP is integrated at a fraction of 34 %. To take into account, the WAP and WP samples were fabricated using the modified wool after 7 days.

The second group includes the shape-stabilized wool particles fabricated through a different method, The AWP is the shape-stabilized wool using alginate as background, and the WP.

Figure 30. thermal conductivity of, a. wool powder, b. wool particles.

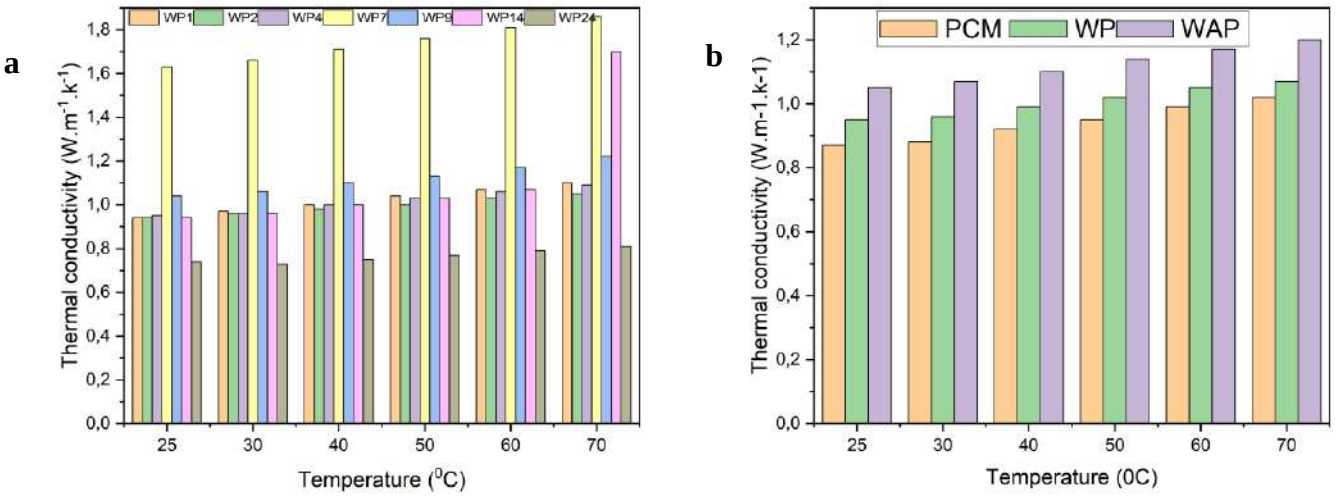

The thermal conductivity of the powder wool matrix is illustrated in (Figure 30. a). The measure was accomplished under a gradual rise in temperature to distinguish the behavior of the powdered wool in different environments. The plotted thermal conductivity gradually increases with the escalation of the temperature. On surroundings 25 °C, the samples could be classified into three stages. The matrix WPA 1, WPA 2, and WPA 4 approximately have the same tendency exposing a conductivity around 0.96 ($w.m^{-1}.k^{-1}$), the second stage endorses the enhancement of the powder conductivity and recording the highest value the wool could achieve, which reached after 7 days of treatment WPA 7 and exposing a value of 1.66 ($w.m^{-1}.k^{-1}$), the last stage includes a variety of reading but the common factor is the decline of the conductivity with extending the chemical treatment, the WPA 9 reveal a transfer of 1.06 ($w.m^{-1}.k^{-1}$) and by the prolongation of the oxidation process the transfer decreases around 0.96 ($w.m^{-1}.k^{-1}$) in WPA 14 to be equal to the first stage, meanwhile the WPA 24 that expose 24 days of treatment shows the lowest transfer behavior in all samples by 0.73 ($w.m^{-1}.k^{-1}$). As a consequence of temperature progression, all the matrix tends to have a similar profile, as the temperature increases, the conductivity is enhanced. At 30°C, the WPA 2 sample exhibits a different regime compared to the samples of the first stage, and this decline continuous until 70 °C revealing the low transfer rate versus the other matrix, nevertheless all the matrix shows enhancement in the rate of transfer with increase the temperature meanwhile the highest conductivity intensification was at 70 °C for WPA 14 which escalate from 1.07 ($w.m^{-1}.k^{-1}$) at

60 °C to 1.7 ($w.m^{-1}.k^{-1}$) at 70 °C. From the aforementioned, the WPA 7 has the highest thermal conductivity, which could be enhanced by the increase in temperature, while the WPA 24 exhibits the lowest conductivity, even with an increase in temperature. Depending on this outcome, the thermal conductivity is proportional to the chemical treatment in the first 7 days of immersion, which is intensified on the last day (7), meanwhile, the excessive treatment affects this property and declines the conductivity to be inversely proportional to the oxidation process.

The (Figure 30. b) illustrates the plot of the variation in the thermal conductivity according to the rise in temperature. The WPA matrix was investigated in two ways: the impact of the wool addition and the effect of the PCM on the matrix behavior. At room temperature of 25 °C, the PCM exhibits the lowest conductivity of 0.41($w.m^{-1}.k^{-1}$), followed by the WPA conductivity of 0.95 ($w.m^{-1}.k^{-1}$) and the highest value related to the WP by 1.05 ($w.m^{-1}.k^{-1}$). As found before the thermal conductivity increases with increasing temperature, identical behavior is distinguished in this experiment, despite the PCM having sensible enhancement as a consequence of its weak thermal conductivity and for the state transition that occurs based on absorbing the heat until the melting all the extent of the PCM, the WPA, and WP show a slight shift in conductivity which alters to be remarkable after 40 °C, Based on the mentioned before the PCM in the WPA and WP matrix melted at 40 °C which hinders the heat transfer before melting and is allowed when the process is complete. The delay in the thermal transfer of the PCM extent in the matrix. On the other hand, the WPA demonstrates a lower thermal conductivity compared to the WP matrix, the dissimilarity is attributed to two factors, the low conductivity of the alginate incorporated in the WPA sample, also related to the high PCM fraction, these two factors induce the bulk thermal conductivity and decrease it to be a lower than WP matrix.

4.7 Results and Discussion

The wool sheep are classified as α-keratin protein, which is mainly composed of amino acids and peptides as linkage, the three-dimensional structure of wool involves a combination of liaison, as hydrogen bond, ionic bond, and disulfide bond, the latter is the strong bond and it is responsible of the mechanical stability of the wool which makes it resistible to grind, the disulfide bond is a link between the different chains and in the same chain, so the destruction of this bond weakens the robust fiber structure, several methods were designed to disrupt the stability of S-S bond, (J. Fan & Yu, 2012) used the oxidation method to cleavage the disulfide

bond by peracetic acid at 1.6 % in 2h ultrasonic irradiation, (Hameed & Guo, 2010) coagulate the wool using the BIMIMCl under heat treatment, (Cheng et al., 2007) Combining the oxidation method with mechanical treatment, the raw fibers were soaked in hydrogen peroxide at 15-30% for 5 min and then cut to facilitate the final grinding step. The same technique was used by (Xu et al., 2004) in this study instead of hydrogen peroxide, a treatment by sodium hypochlorite at 0.5%, followed by several pulverization steps to obtain a fine powder. An identical procedure was designed to drive a fine powder. from the image, the collected powder after 7 days is yellowish; this outcome is the impact of the slow alkali treatment and might be due to the applied heat from the milling process. Even so, the final product tends to be fibrous. It is widely known that the fiber in a simple model is a cortical enriched with α-helix conformation surrounded by a cuticle sheath with a β-sheet and disorder (Wen et al., 2010), from the FTIR results, the mode of amide I am accord to the β sheet, at the same time the broad peak at 1084 cm^{-1} that confirmed the destruction of the disulfide bond and according to the intensification in the absorbance of the amide I as well as the shift to higher frequency confirmed the powder stat, a logical explanation is the excessive oxidation may affect the crystallinity of the samples and exhibit the β sheet mode, (Xu et al., 2004) mentioned that the crystallinity decreases with decrease in the particles size referring the impact of the milling process in the destruction of large scale crystals, (Xu et al., 2006) assumed that the crystal is sensible to the high thermal impact or mechanical action and allude to the humidity effect onto the reduce of the crystallinity of wool powder. (Wojciechowska et al., n.d.) Ascribed the damage of expanding the pretreatment period or the oxidation process on the crystallinity prosperity of the fabricated powder, which is related to enhancing the amorphous β configuration. (J. Fan & Yu, 2012).

The wool powder mechanism, started by immersing the wool fiber in hypochlorite to ensure the weakening of the disulfide bond and facilitate the mechanical grind, the chlorine attacks the sulfur bond at the cuticle sheath, precisely the cystine acid at the end of the process a fragment produced mainly cortical intact a cause de destruction of the outer fiber the core appeared, the cortical particles have a high crystallinity ascribed to the α-helix conformation, this particles cystine acid, in the case of delaying the oxidation process the chlorine target the cortical and converted into cystic acid (Harris & Smith, 1936) (J. Fan & Yu, 2012) according to (J. Fan & Yu, 2012) a macrofibrils structure distinguished throughout the cystine oxidation, the second decomposition phase triggers the amorphous structure and affects the bulk crystallinity of the fiber, the fragile fiber is then induced to the mechanical treatment to fabricate a fine powder,

and this process damages the remaining order structure under the executed pressure and the heat produced during the grinding process.

The PCM impregnated into wool demonstrates interaction as described in FTIR, besides the shifting and reduction of the 719 cm^{-1} peak on PCM, the intensities of the amide I, the peaks at 1086 cm^{-1}, 1446 cm^{-1}, 454 cm^{-1} in the specter PCM wool increase in front of the wool powder this outcome supports the absorb and the adsorb of the PCM into the wool, the adsorption into wool powder occur as cause of the high surface area and to the negative charge of cystic acid, (Khosravi & Montazer, 2023)assumed the free disulfide bonds have a high affinity to rebuild to recuperate the stable state, ascribed to the interaction between the wool powder and the fatty acid. (Wen et al., 2010) explained the ability of the wool powder to react and bind in any environment, acidic or alkaline, depending on the IEP (isoelectric point) referring to the carboxylate group and hydroxyl side, concluding to the wool powder's adsorption and absorption potential.

As mentioned before to the alteration of the intrinsic nature of the wool under high temperatures and according to the TGA and the DSC of the wool powder, a polymeric matrix was crucial to enhance the thermal stability and to maintain the absorbance ability, concern the shape stabilized wool by alginate polymer, a prosperous fabrication assesses indispensable conditions, and an optimum portion is essential to modulate a spherical bead and facilitate the squeezing of the mixture, and to prevent the inherent of the saturated wool particle and ensure the dispersity. At the crosslinking stage, the saturated wool powder is sequestrated into the alginate network during the reticulation of the polymer by calcium chloride, as demonstrated in the alginate chapter. The ionic crosslinking process of alginate is rapid, but in the case of integrating the wool, the mechanism is quite lent.

The decrease of the entanglement of ALG-wool, the wool's tendency to absorb water, affects the stability, and as a consequence, its intrinsic affinity, a loss of absorbed PCM occurs, especially after the enhancement of hydrophilicity and the rise in absorbance rate in the powder state (Golafshan et al., 2017). a new formulation is generated to reduce the absorbance of water and prevent the PCM exchange, PVA-ALG-Wool fabricated in the same procedure (Figure 31), the pebble of the mixture is hardened by the diffusion of the boric acid and calcium chloride into the globule striking the proper polymer, the calcium chloride reacts with the alginate forming the egg-box structure and the boric acid interact to the PVA through hydrogen bond, the two mechanisms occurred in concomitant rhythm, large studies used the polymer

mixture as support or as shell, (Zain et al., 2011) delve into reducing the self-interaction of the PVA chains between the fabricated beads by introducing it to a boric acid solution,

Figure 31. Fabrication mechanism of shape stabilized wool particles.

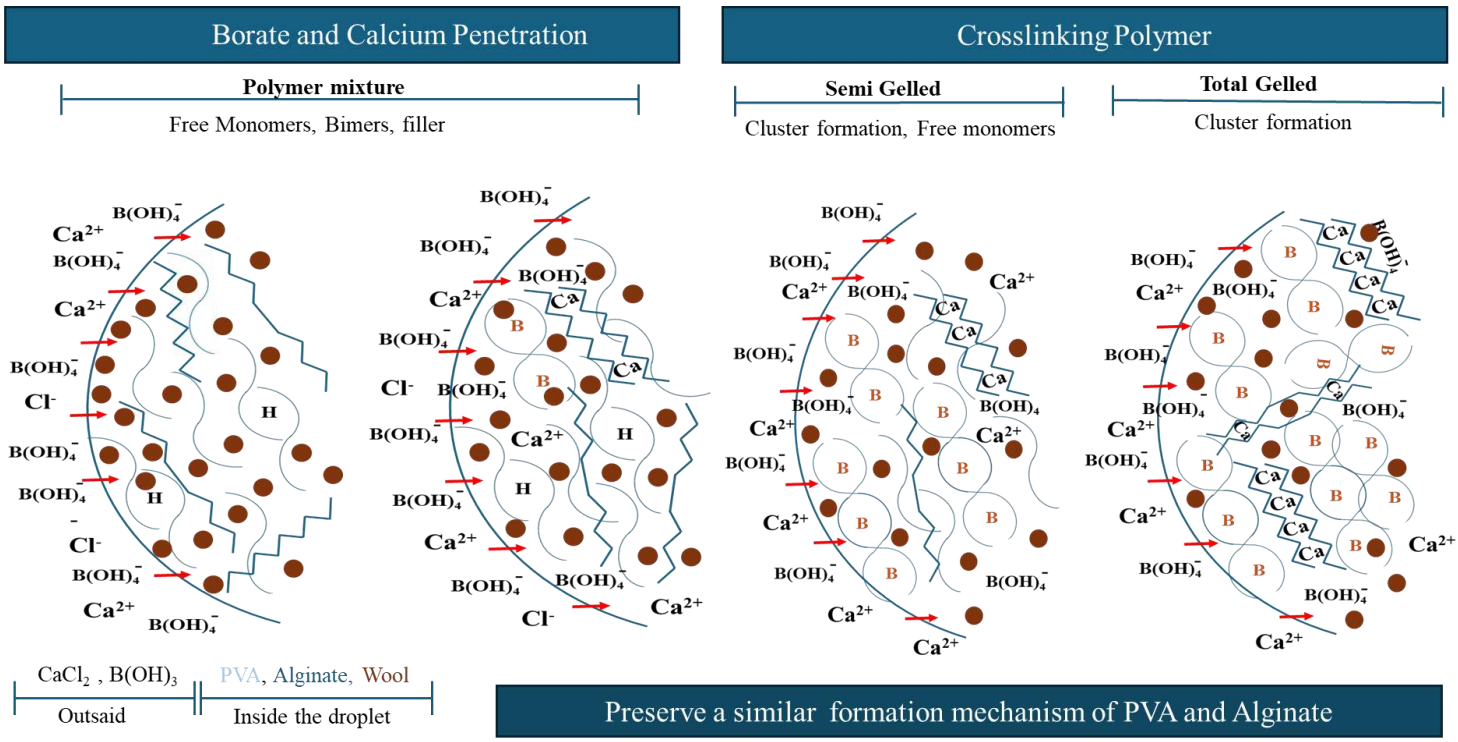

The replacement of the crosslinking to sodium sulfate shows a bit of difference, while the addition of the alginate improves the dispersity of the preformed beads. (Golafshan et al., 2017) enhanced the intermolecular interaction of the PVA to affect the intramolecular forces by raising the extent of the alginate in the mixture, both studies confirm the consolidation of the beads by the hydrogen bond between the alginate and the PVA.

In this study, the PVA was used to reduce the water penetration while the alginate accelerated the fabrication period, depending on the TGA and the DSC results the alteration made by the incorporation of the PVA is insufficient according to the long imperative condensation time which almost 24 h, the pristine alginate polymer was selected as wool stabilizer.

In the TGA analysis, and according to the saturated wool profile, the powder affects the stability of shape-stabilized particles depending on the oxidation treatment, the particles of 24 days WPA24 are slightly sable compared to WPA 4 that incorporates the collected wool after 4 days while the WPA2 exhibits the lowest stability, these results confirmed by the thermal

conductivity analysis wherein the saturated wool (WP) display a higher conductivity in front of shape stabilized wool particles (AWP), meanwhile, the thermal conductivity of powder performed at a different level of chemical treatment expose tree behavior phases, in the initial stage the four first days expose a slight enhance in their thermal conductivity during the treatment exhibit the maintain of an intrinsic property of the fiber proving the endurance of the cuticle while intensification recorded on the seventh day pronouncing the interference of a difference compounds indicate the destruction of the fiber sheath and expose the inner structure, at the third stage as much as the oxidation occurs the decrease in the feedback conductivity observed wherein the lowest value measured after 24 days exposing the minimal record in the study even after day 1. As mentioned before the sheath fiber is mainly composed of an amorphous structure as a wide fraction and a slight crystalline constituent so the destruction of the outer shell increases the amorphous region in the early oxidation while the increase of the time the oxidant penetrates the fiber that already weakened and strike the disulfide bond in the cortical and exposit and as a consequence of the high crystallinity of cortical the conductivity of the bulk material improve while in the excessive treatment the chlorine attack the cortical and dissociated which increase the amorphous structure that alters the conductivity and rise it even more than the first stage.

Chapter 5. APPLICATION STUDY OF THE PERFORMED SAMPLES

5.1 Alginate matrix performance

In the investigation of the performance of the prepared alginate capsules, the one-step incorporation method was selected, the panels were designed by impregnating the alginate microcapsules in the gypsum matrix, and the procedure involved the dry mixture to ensure the dispersity of the samples followed by water blending, the hydration process respects the wastegate fraction of 0.6 to preserve the intrinsic properties of the gypsum and facilitate the modeling, four types of panels were designed, gypsum panel labeled gyp as a control panel to distinguish the proper impact of capsules, microcapsule alginate panel labeled as MA or MAgyp, prepared by incorporating the alginate in a fraction of 7.5 %, the last is MACSi which fabricate in the fraction of 7.5 %, another panel was designed by integrating the pristine PCM in fraction of 1.48%.

The prepared panels were investigated in two different environments, in the laboratory as a controlled situation, and on the outside in the real environment. The measures of temperature variation were detected by a K-type sensor, and the progression results were recorded by a data logger (PCT T 1200 model).

Figure 32. Temperature acqusition methodologies.

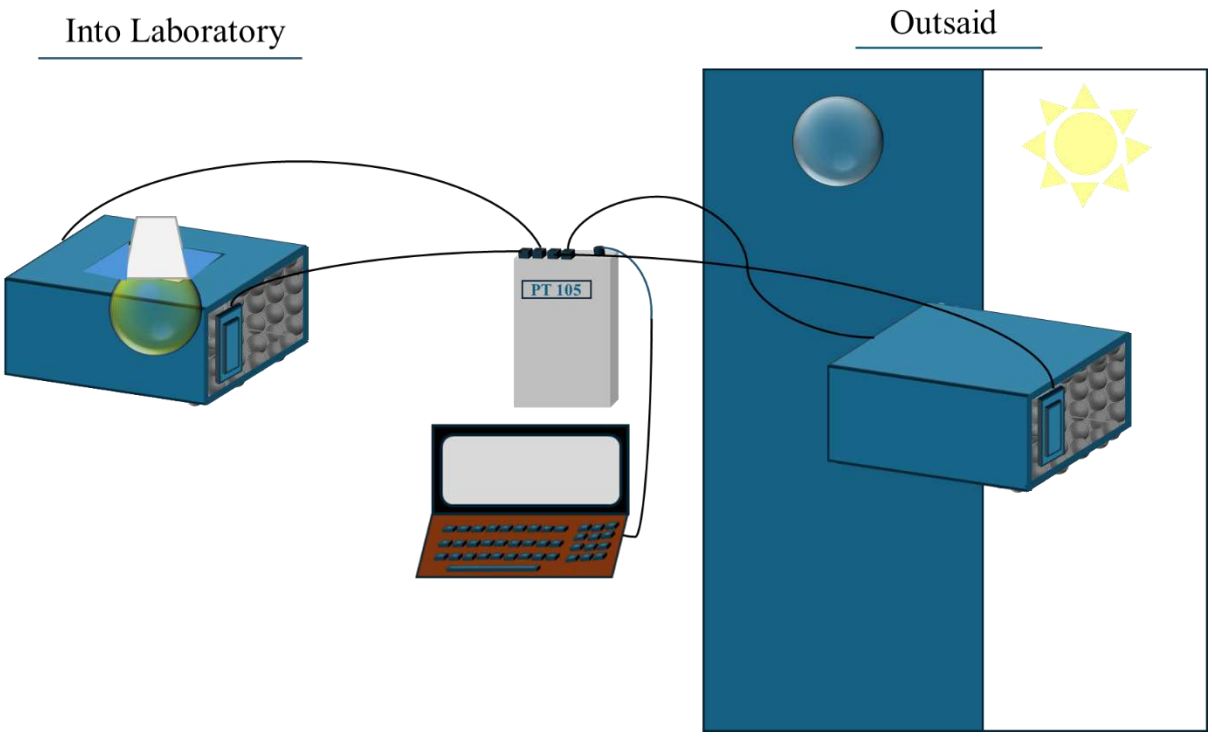

5.1.1 The laboratory acquisition

(Figure 33) present the temperature acquisition in the laboratory, the experience occurred for 5 hours to investigate the panel endurance under long thermal treatment.

The approach was based on a heating-cooling cycle; the alginate and the control panels were subjected to a direct heat flux source for 325 minutes, followed by a natural cooling process after segregating the source heat.

Depending on the displayed results, it is possible to bifurcate the profile into three stages, the heat stage identified in the range of 0-50 minutes, exposes the required time to heat the panel and reach the stable state at which no remarkable progression is recorded, gyp panel achieves this point earlier than the MA gyp localized at 40 ℃, in this regard the PCM act as a barrier and accumulate the absorbed energy that affects the inherent matrix property and hinders the

Figure 33. Temperature gain in the laboratory of MA-gypsum and gypsum

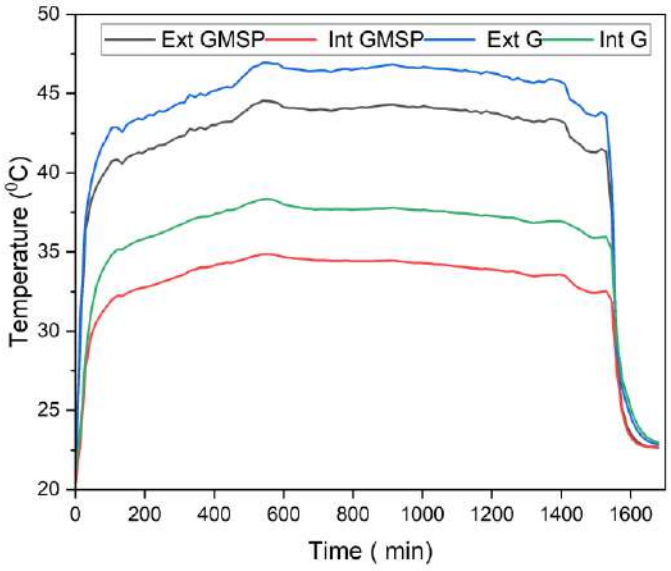

temperature progression, which delayed the heat process to 50 min. The estimated gain is an average of 2 ℃ for the gyp matrix and approximately 4 ℃ in the MA gyp panel.

In the second stage, a stable behavior is dominant along with time, comprising a range of 50-325 ℃, this attitude reveals that the surface reached the energy transmitted by the heat source, which permeates to investigate the material integrity to preserve the energy in the form of heat. The gain in this stage is around 1-1.5 ℃ for gyp and arrives at 2-3 ℃ for the MA gyp. At 206 minutes even though the panels were subjected to the source, the decrease in the ambient

temperature overlapped the heat flux and converted the sides at which the exterior presented the lowest temperature while the interior face exposed the highest, in this situation the PCM had a crucial role to postpone the adaptation of the new circumstance due to the release of the absorbance energy followed by inversing the sides at 295 minutes.

In the cooling stage, at the moment the heat source was segregated, a sharp decline was observed.

5.1.2 The acquisition of outdoor

In the outdoor investigation, the matrix was placed out to undergo the real environment; in this regard, two experiences were established as described below.

(Figure 34. a) present the temperature profiles of the interior surface of the gyp, MA gyp, and PCM gyp, the latter panel was programmed to distinguish the impact of the sheath, for this purpose, the fabricated matrix based on the estimation of the PCM fraction inside the integrated alginate microcapsules panel was effectuated to moderate the issues and ensure an effective comparison.

The placed out panels were subjected to the day for 10 hours, the profiles exhibit the mode of oscillation as a consequence of the instantaneous alteration of the recorded temperature which imitates the reel behavior of the samples in the bare environment without insulation wherein they submitted to be affected by several factors as the disruption of the wind that acts in place of the cooling process. From the figure below the temperature, the configuration could be divided into two stages, the sunlight period localized in the range of 0-400 minutes, at this stage the oscillation mode is dominant, and the MA gyp and PCM gyp show the lowest temperature compared to gyp panel, unpredictable behavior expose by PCM in front of the MA gyp, according to its capacity to absorb the heat during the transition phase from solid to liquid including its low thermal conductivity, the result should be more enhanced, the logical explanation of this behavior related to the low incorporated fraction of PCM, while the MA capsules have a higher fraction which composed of the PCM that already present in the PCM panel and in addition the fraction of the shell that impacts the matrix as a consequence of its low conductivity.

The higher acquisition was registered at 40 °C after 50 minutes, indicating that the samples were exposed to a hot environment.

The second stage is attributed to the sunset period, in this phase the low temperature affected the thermal behavior of the panels and reflected an identical trend recognized by a profile superposition.

The gain that occurred from incorporated microcapsules was estimated to be around 1-2 ℃, a similar outcome found in the laboratory experiment when effectuating a subtraction between the profiles of MA gyps and gyp.

Figure 34. Temperature gain of, a. outside MA gypsum PCM gypsum, b. outside MA MACSi.

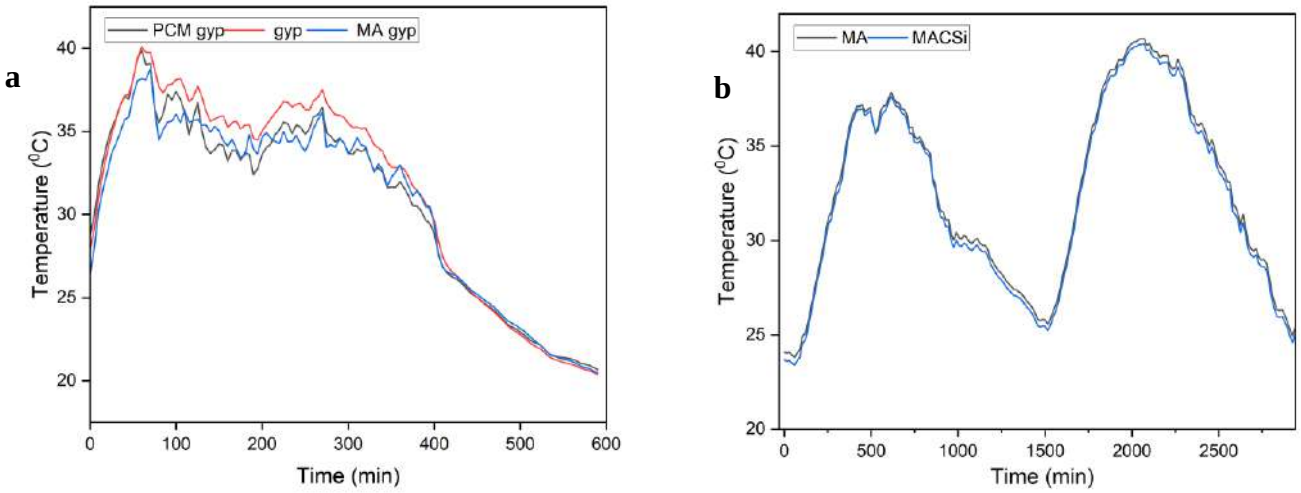

In the investigation of the thermal performance of the PVA microspheres, a prototype was designed to imitate an outdoor indoor model (Figure 35), in this purpose two hollow cubes with dimensions of 5*5*0.5 cm were manufactured by maintaining a fraction of 15 % of microspheres. The preformed prototype labeled according to the impregnated samples, GMSP for the microspheres PVA and GMSPTi 2 ascribed to the modified microspheres by 2% of titanium dioxide, a control prototype fabricated in the same dimension to distinguish the reel enhancement.

The fabrication procedure followed the one-step incorporation method, the microspheres were mixed with the gypsum powder in dry form to establish a homogenous mixture by ensuring the

Figure 35. Prototype realisation steps.

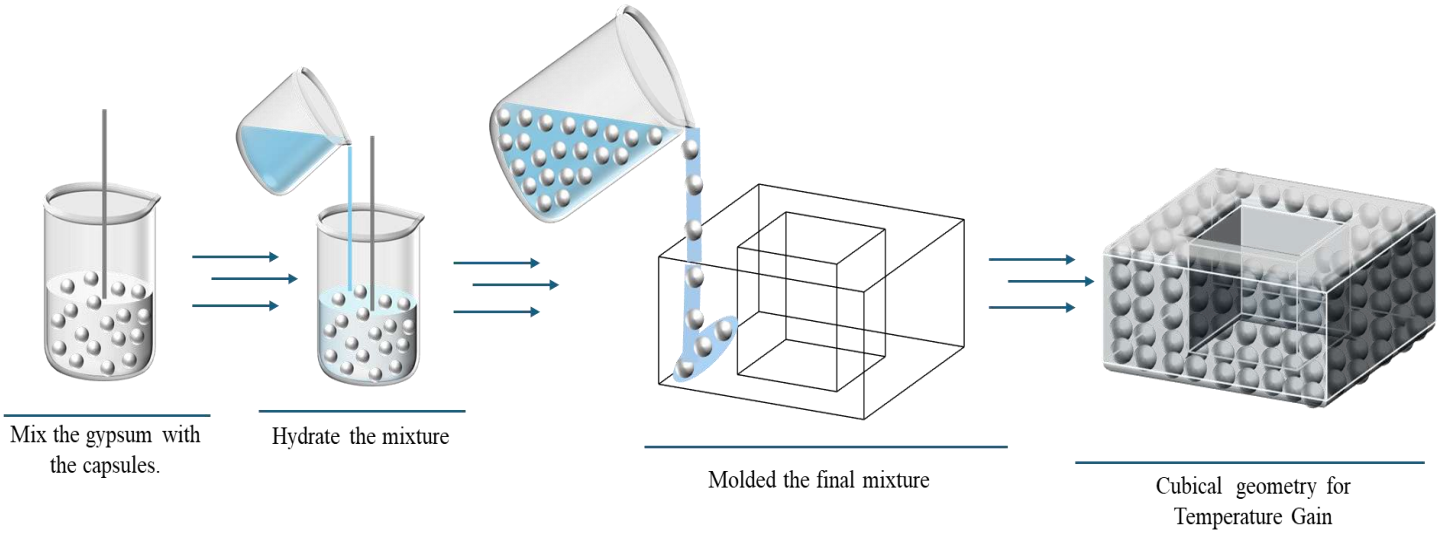

dispersity of microspheres. at this state, the blending process was effectuated by adding the water according to a wastage fraction of 0.6 %, to preserve the inherent properties of the gypsum and produce a compact prototype. The acquisition was registered through a data logger (PCT T 1200 model) by using K-type sensors with an accuracy of +/-0. 1°C.

5.2.1 The acquisition in the laboratory

(Figure 36. a) illustrate the recorded temperature of the interior and exterior faces of the prototype in PVA(GMSP) and in the control G, the prototypes were subjected to a direct heat flux for more than 26 hours. The extent of the process was intentional to investigate the endurance of the microspheres.

The investigation triggers the heating-cooling cycle, the prototypes were subjected to a direct heat flux source for 26 hours where the cooling process was due to the surrounding climate when switching off the heat source.

Based on the acquisition temperature, the profiles could be divided into three stages,

the heat stage located in the range of 0-46 minutes, established by the heat absorption that necessitated maintaining a steady behavior wherein identified by change in the temperature profile from continuous uplift to stable attitude, the g model reached a stable behavior at 31 ℃, while the GMSP extend the process to 46 ℃, as mentioned before this phenomenon is ascribed

to the PCM attitude under heat treatment, the delay is related in the first place to the fraction of the PCM also the surrounded material that affect the transfer of the heat flux.

Figure 36. temperature gain, a. GMSP, b. GMSP and GMSPTi 2.

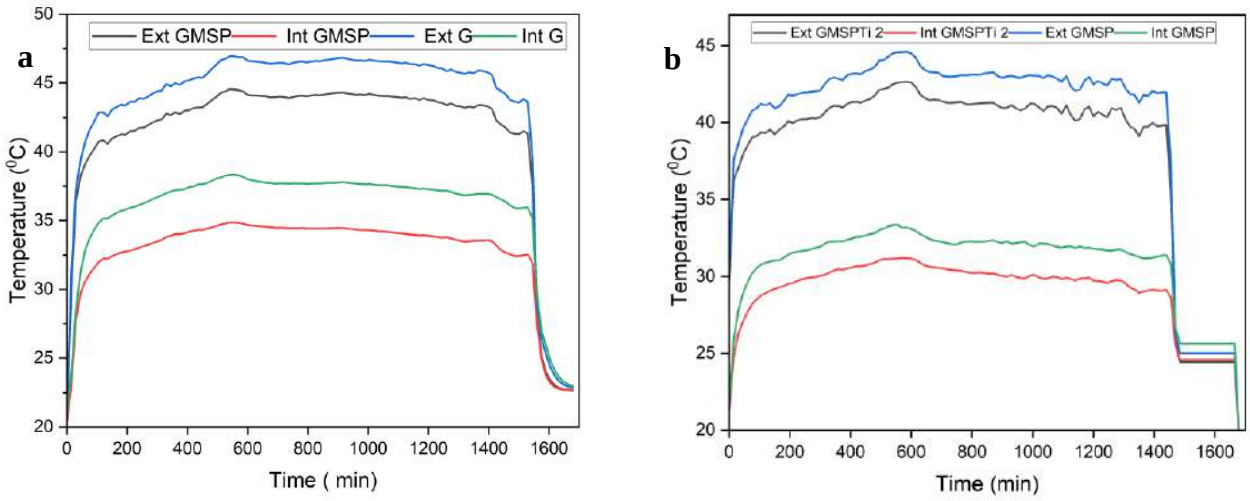

have similar behavior, as mentioned before the three stages were eventually distinguished reflecting the behavior of the prototypes under the heat treatment, according to curves of the prototypes have identical gain around 4°C to 3°C for GMSP and GMSPTi respectively.

5.2.2 The acquisition of outdoor

The investigation required placing the matrix on the outside, in this regard two experiences were carried out to estimate the difference between the control, the pristine, and the modified sample.

The (Figure 37. a) presents the profiles of the temperature of the GMSP and the GMSPTi,

the prototypes were subjected to the day-night cycle where the day is ascribed to the heat process and the night exposes the cooling process, the prototypes exhibit the mode peak, and the highest temperature is around 40 °C. The temperature profile could be separated into two

Figure 37. temperature gain, a. GMSP outside, b.GMSP AND GMSPTi 2.

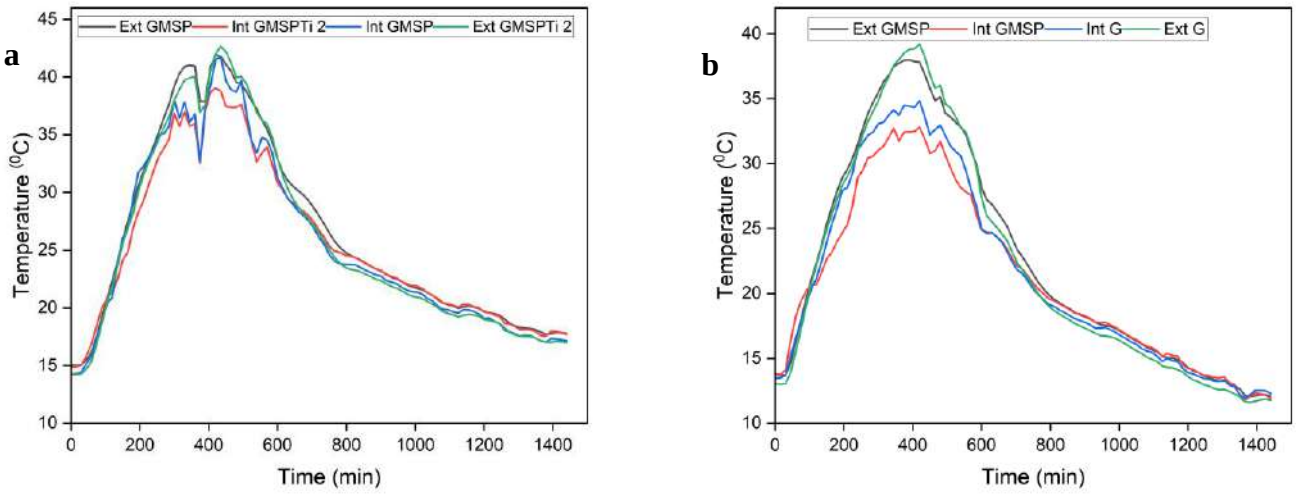

stages, the sunlight period wherein the curves display a continuous progression with time imitating the heat provided by the sun from the sunrise to the middle of the day this phenomenon occurs until reaching the peak state which appears after 500 minutes combined by the peaky temperature at 40 ℃, while the samples change their regime imitates the sunset period, and exhibit a gradual decline according to the decrease in ambient temperature that accompanied the screen of the sun. The comparison of the curves shows a slight change in front of the laboratory experiment, the recorded gain is around 3 ℃ and 2 ℃, ascribed to GMSP and GMSPTi 2, respectively.

(Figure 37.b) presents the temperature variation of the GMSP and the G, the same procedure was adapted to investigate the effect of the real environment on the temperature profiles.

The prototypes were induced to the day-night cycle for 1 day. The temperature regime could be divided into two stages, the first phase is a continuous progression from the dawn to the middle of the day attributed to 400 minutes of exposure by reaching the peak temperature of 39 ℃, the samples change their behavior after 400 minutes according to the surrounding climate and decline gradually as a consequence of natural cooling. The subtraction of the curves shows that the highest value that could be reached is about 6℃ and 4 ℃ for GMSP and G, respectively.

5.3 The wool matrix performance

The wool performance was investigated by subjecting the gypsum wool matrix to heat treatment. The approach used in this study is one-step incorporation. The fabricated procedure used the dry technique to provide a homogenous mixture through the good dispersion of the incorporated material at the designed fraction. In this regard, the blending of the homogeneous mixture respects the hydration fraction of 0.6%.

To distinguish the alteration provided by powdering the fiber, a cascade of panels with a different fraction was effectuated, the fiber panels were manufactured to obtain fractions at 1 %, 1.5 %, and 2.33%, while the powder panels were designed at fractions of 1.5 %, and 2.5 %, and control panel. All the experiment is effectuated in the laboratory by inducing the panels to a direct heat flux.

The (Figure 38.a) demonstrates the gain variation of fiber panels under heat treatment for 27 hours, the panel's ambient temperature in the samples of 2.5 and 2.33 show slight enhancement compared to the other samples, in general, the dominant behavior was the increase in the gain with increasing the treatment period or rising the heat flux, the panel of fraction 1.5 show the highest gain in front of the rest of samples, depending on panels attitude the panel of 1% show the lowest gain compared to other samples explains that the gain is related to the fraction of fiber, as much the incorporated fiber as much the gain is important, in the other hand, the gain shows proportional behavior with expanding the treatment period indicating that the fiber could endure the long period and enhance its ability to improve the insulation range, this outcome is confirmed by the gypsum behavior which is an oscillation mode in intervals of 3 °C while the rest panels expose an enhancement GWF 1 %, GWF 1.5%, depending on previous explanation the GWF 2.33 % display low gain in front of the integrated fiber GWF 2.33 revels the lowest value, the logical explanation is the samples don’t absorbed enough energy to reflected to gain which means that the heating is very lent and isn’t sufficient to interfere inside the sample to

Figure 38. the temperature gain, a. wool fiber, b. comparison wool fiber and powder.

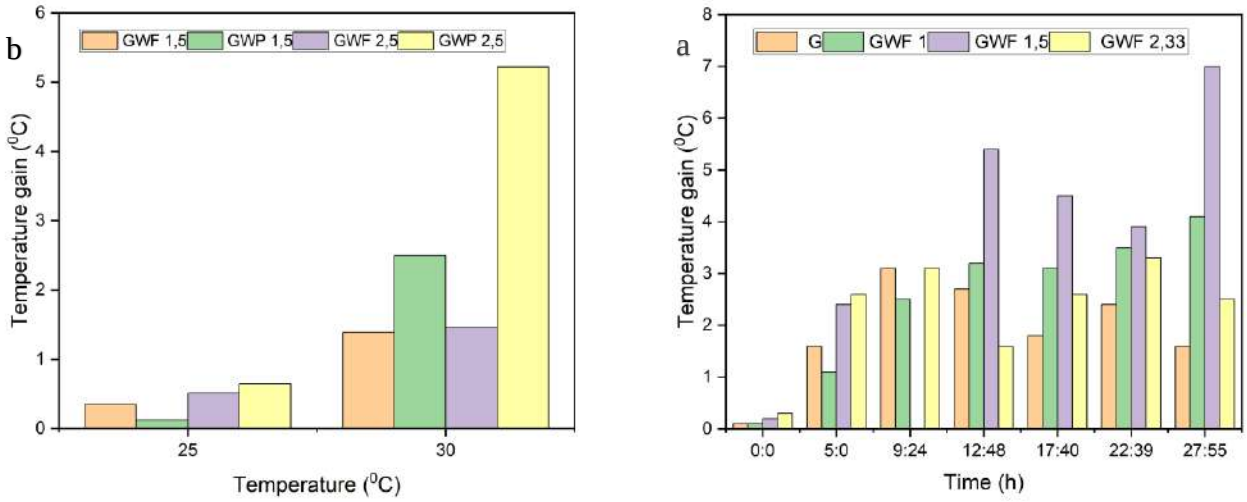

reach the other side (interior) as mentioned before the GWF 2.33 is still in the first stage. according to the aforementioned the rise in the fraction enhance the gain.

(Figure 38.b) illustrate the comparison between the raw material and the powder, at 25 ℃ the panels of 1.5 % fiber show a higher gain of 0.35 compared to the powder sample 0.11 while at a fraction of 2.5 %, the powder sample exhibits a slight gain of 0.65 in front of the fiber panel 0.50 wherein they enhance the gain that displays on 1% incorporation. At 30 ℃, the panels rise intensified the gain to a different level, wherein the powder panels reveal a high gain compared to the raw material samples, the GWP 2.5 % exhibits a higher gain around 5.21 ℃ followed by GWP 1.5 that exposes insulation by 2.5 ℃ while the fibers give an enhancement around 1.45 ℃, 1.39 ℃ attributed to GWF 2.5 % and GWF 1.5 % respectively. Based on the obtained results, the powders show rapid adaptation to the new circumstance compared to the fibers. Despite the high potential of raw material, the lent reflection is an issue that could be rectified by powderization.

(Figure 39) demonstrate the behavior of the powder panel under the heat treatment for 5 hours, effectuating two successive cycles. In the heating cycle, the panels were subjected to heat flux and then cooled naturally by the surrounding climate after switching off the heat source.

Depending on displayed curves, the powder panel exhibits lent reflection exposed by delaying heat absorbance compared to the control sample, in this experiment the heat cycle was carried out to simulate the effect of natural heat behavior, in this purpose the elimination of the heat source was before reaching the sample's capacity of absorbing the energy, at this regard the

peak reached after 65 min while delayed slightly to 69 min, in the cooling process the exterior was decline sharply to a certain level as a consequence of eliminating the heat source than broadly based on its intrinsic properties, the cycle complete at 128 minutes, while the G and GWP 1.5 % decline broadly while the cycle obstructed to 135 minutes. In the first cycle, the GWP 1.5% gained 2 ℃ and the control gained 1 ℃. The second cycle commences after 1 hour of cooling, and the heat continues to reach 29 ℃ after 185 minutes the cooling is triggered by segregating the heat source

identical behavior recorded as cycle 1, the gain obtained from the second cycle in the control panel was estimated by 0.04 ℃, while the powder panel in a fraction of 1.5 % reached 1.5 ℃; these outcomes indicate the rapid reflection of the gypsum in front of the matrix of the gypsum wool.

Figure 39. the gain temperature of wool powder matrix.

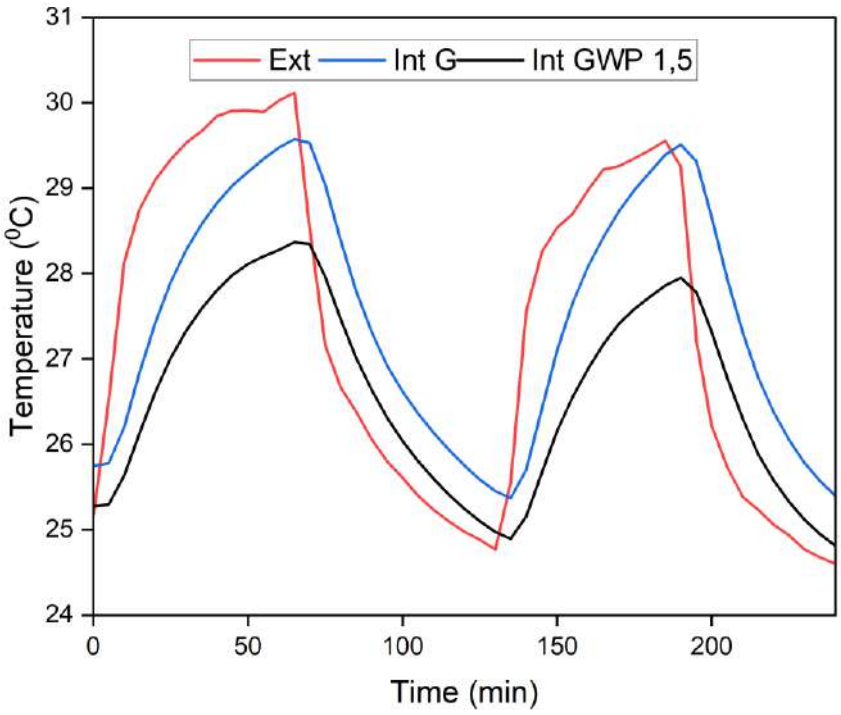

CONCLUSION

In this study, we developed a thermal energy storage microcapsule suitable for thermal applications, using various fabrication technologies. The design of the new energetic microparticles, incorporating phase change materials (PCMs), involves several factors, with selection based on essential characteristics such as bioresource availability and non-toxicity.

Alginate-PCM microcapsules were successfully fabricated using a microfluidic system, producing mononuclear capsules, while the in-situ polymerization technique was employed to create alginate-PCM microspheres. The thermal stability of the alginate microcapsules was enhanced by adding calcium carbonate and calcium silicate through an in-situ method within the alginate polymer. FTIR and TGA analyses confirm the crystal growth within the alginate polymer.

On the other hand, PVA-PCM microspheres were fabricated using the in-situ polymerization technique, and enhanced microspheres were obtained by incorporating titanium dioxide nanoparticles through an ex-situ technique. FTIR and TGA analyses confirm the confinement of the added nanoparticles within the PVA polymer.

Shape-stabilized wool was obtained by powdering sheep wool fibers treated with various methods. The wool was then integrated into a polymeric matrix. In this context, alginate polymer and a mixture of alginate and PVA were used to create the matrix, and FTIR and TGA investigations confirm the successful fabrication of the matrix.

Thermoregulatory samples were examined using dynamic scanning calorimetry to ascertain the sequestration of the integrated PCM, while thermal conductivity measurements were used to assess thermal transfer.

REFERENCES

˙bieta Wojciechowska, E., Włochowicz, A., Wysocki, M., Pielesz, A., & Wesełucha-Birczyn´skabirczyn´ska, A. (n.d.). *The application of Fourier-transform infrared (FTIR) and Raman spectroscopy (FTR) to the evaluation of structural changes in wool fibre keratin after deuterium exchange and modification by the orthosilicic acid*. www.elsevier.com/locate/molstruc

Ahmad, J., Deshmukh, K., Habib, M., & Hägg, M. B. (2014). Influence of TiO2 Nanoparticles on the Morphological, Thermal and Solution Properties of PVA/TiO2 Nanocomposite Membranes. *Arabian Journal for Science and Engineering*, *39*(10), 6805–6814. https://doi.org/10.1007/s13369-014-1287-0

Ahmad, J., Deshmukh, K., & Hägg, M. B. (2013). Influence of TiO2 on the Chemical, Mechanical, and Gas Separation Properties of Polyvinyl Alcohol-Titanium Dioxide (PVA-TiO2) Nanocomposite Membranes. *International Journal of Polymer Analysis and Characterization*, *18*(4), 287–296. https://doi.org/10.1080/1023666X.2013.767080

Aslani, P., & Kennedy, R. A. (1996). controlled release Studies on diffusion in alginate gels. I. Effect of cross-linking with calcium or zinc ions on diffusion of acetaminophen. In *Journal of Controlled Release* (Vol. 42).

Ayarza, J., Coello, Y., & Nakamatsu, J. (2017a). SEM–EDS study of ionically cross-linked alginate and alginic acid bead formation. *International Journal of Polymer Analysis and Characterization*, *22*(1), 1–10. https://doi.org/10.1080/1023666X.2016.1219834

Ayarza, J., Coello, Y., & Nakamatsu, J. (2017b). SEM–EDS study of ionically cross-linked alginate and alginic acid bead formation. *International Journal of Polymer Analysis and Characterization*, *22*(1), 1–10. https://doi.org/10.1080/1023666X.2016.1219834

Bajpai, S. K., & Sharma, S. (2004). Investigation of swelling/degradation behaviour of alginate beads crosslinked with Ca2+ and Ba2+ ions. *Reactive and Functional Polymers*, *59*(2), 129–140. https://doi.org/10.1016/j.reactfunctpolym.2004.01.002

Barbut, S., & Harper, A. (n.d.-a). INFLUENCE OF RELATIVE HUMIDITY ON DRIED CA ++-ALGINATE FILMS AND COMPOSITES MADE WITH SOY AND PECTIN. In *Ital. J. Food Sci* (Vol. 32).

Barbut, S., & Harper, A. (n.d.-b). INFLUENCE OF RELATIVE HUMIDITY ON DRIED CA ++-ALGINATE FILMS AND COMPOSITES MADE WITH SOY AND PECTIN. In *Ital. J. Food Sci* (Vol. 32).

Bienaimé, C., Barbotin, J.-N., & Nava-Saucedo, J.-E. (2003). *How to build an adapted and bioactive cell microenvironment? A chemical interaction study of the structure of Ca-alginate matrices and their repercussion on confined cells*. http://rsb.info.nih.gov/nih-im-

Cao, L., Li, J., Parakhonskiy, B., & Skirtach, A. G. (2024). Intestinal-specific oral delivery of lactoferrin with alginate-based composite and hybrid CaCO3-hydrogel beads. *Food Chemistry*, *451*. https://doi.org/10.1016/j.foodchem.2024.139205

Chan, E. S. (2011). Preparation of Ca-alginate beads containing high oil content: Influence of process variables on encapsulation efficiency and bead properties. *Carbohydrate Polymers*, *84*(4), 1267–1275. https://doi.org/10.1016/j.carbpol.2011.01.015

Chen, X. W., Dong, S. M., Kan, Y. M., Zhou, H. J., Hu, J. B., & Ding, Y. S. (2016). Effect of glycerine addition on the synthesis of boron carbide from condensed boric acid-polyvinyl alcohol precursor. *RSC Advances*, *6*(11), 9338–9343. https://doi.org/10.1039/c5ra23303h

Cheng, Y. F., Yuen, C. W. M., Li, Y., Ku, S. K. A., Kan, C. W., & Hu, J. Y. (2007). Characterization of nanoscale wool particles. *Journal of Applied Polymer Science*, *104*(2), 803–808. https://doi.org/10.1002/app.25631

Choe, S., You, S., Park, K., Kim, Y., Park, J., Cho, Y., Seo, J., Yang, H., & Myung, J. (2024). Boric acid-crosslinked poly(vinyl alcohol): biodegradable, biocompatible, robust, and high-barrier paper coating. *Green Chemistry*, *26*(14), 8230–8241. https://doi.org/10.1039/d4gc00618f

Davarcı, F., Turan, D., Ozcelik, B., & Poncelet, D. (2017). The influence of solution viscosities and surface tension on calcium-alginate microbead formation using dripping technique. *Food Hydrocolloids*, *62*, 119–127. https://doi.org/10.1016/j.foodhyd.2016.06.029

De Rosa, C., Auriemma, F., & Di Girolamo, R. (2014). Kinetic analysis of cryotropic gelation of poly(Vinyl Alcohol)/water solutions by small-angle neutron scattering. *Advances in Polymer Science*, *263*, 159–197. https://doi.org/10.1007/978-3-319-05846-7_4

Dodda, J. M., Bělský, P., Chmelař, J., Remiš, T., Smolná, K., Tomáš, M., Kullová, L., & Kadlec, J. (2015). Comparative study of PVA/SiO2 and PVA/SiO2/glutaraldehyde (GA) n

anocomposite membranes prepared by single-step solution casting method. *Journal of Materials Science*, *50*(19), 6477–6490. https://doi.org/10.1007/s10853-015-9206-7

Fan, J., & Yu, W. dong. (2012). High yield preparation of keratin powder from wool fiber. *Fibers and Polymers*, *13*(8), 1044–1049. https://doi.org/10.1007/s12221-012-1044-5

Fan, Q., Xue, W., Wei, Z., Chen, X., Liu, Y., Chen, J., Wu, H., & Province Engineering, J. (n.d.). *Enlarging Calcium Alginate Liquid-Core Capsules: Manufacturing, 2 Microstructure, and Beverage Packaging Applications Education on Food Synthetic Biotechnology*. https://ssrn.com/abstract=4782165

Filippo, E., Carlucci, C., Capodilupo, A. L., Perulli, P., Conciauro, F., Corrente, G. A., Gigli, G., & Ciccarella, G. (2015). Facile preparation of TiO2-polyvinyl alcohol hybrid nanoparticles with improved visible light photocatalytic activity. *Applied Surface Science*, *331*, 292–298. https://doi.org/10.1016/j.apsusc.2014.12.112

Fu, X., Liang, Y., Wu, R., Shen, J., Chen, Z., Chen, Y., Wang, Y., & Xia, Y. (2019). Conductive core-sheath calcium alginate/graphene composite fibers with polymeric ionic liquids as an intermediate. *Carbohydrate Polymers*, *206*, 328–335. https://doi.org/10.1016/j.carbpol.2018.11.021

Fundueanu, G., Esposito, E., Mihai, D., Carpov, A., Desbrieres, J., Rinaudo, M., & Nastruzzi, C. (1998). Preparation and characterization of Ca-alginate microspheres by a new emulsification method. In *International Journal of Pharmaceutics* (Vol. 170).

Ghorbel, N., Kallel, A., & Boufi, S. (2019). Molecular dynamics of poly(vinyl alcohol)/cellulose nanofibrils nanocomposites highlighted by dielectric relaxation spectroscopy. In *Composites Part A: Applied Science and Manufacturing* (Vol. 124). Elsevier Ltd. https://doi.org/10.1016/j.compositesa.2019.05.033

Golafshan, N., Rezahasani, R., Tarkesh Esfahani, M., Kharaziha, M., & Khorasani, S. N. (2017). Nanohybrid hydrogels of laponite: PVA-Alginate as a potential wound healing material. *Carbohydrate Polymers*, *176*, 392–401. https://doi.org/10.1016/j.carbpol.2017.08.070

Habiba, U., Joo, T. C., Siddique, T. A., Salleh, A., Ang, B. C., & Afifi, A. M. (2017). Effect of degree of deacetylation of chitosan on adsorption capacity and reusability of chitosan/polyvinyl alcohol/TiO2 nano composite. *International Journal of Biological Macromolecules*, *104*, 1133–1142. https://doi.org/10.1016/j.ijbiomac.2017.07.007

Hameed, N., & Guo, Q. (2010). Blend films of natural wool and cellulose prepared from an ionic liquid. *Cellulose*, *17*(4), 803–813. https://doi.org/10.1007/s10570-010-9411-0

Harris, M., & Smith, A. L. (1936). *OXIDATION OF WOOL: ALKALI~SOLUBILITY TEST FOR DETERMINING THE EXTENT OF OXIDATION 1* (Vol. 17).

Hashimoto, S., & Furukawa, K. (n.d.). *Immobilization of Activated Sludge by PVA-Boric Acid Method*.

Hecht, H., & Srebnik, S. (2016). Structural Characterization of Sodium Alginate and Calcium Alginate. *Biomacromolecules*, *17*(6), 2160–2167. https://doi.org/10.1021/acs.biomac.6b00378

Islan, G. A., Cacicedo, M. L., Bosio, V. E., & Castro, G. R. (2015). Development and characterization of new enzymatic modified hybrid calcium carbonate microparticles to obtain nano-architectured surfaces for enhanced drug loading. *Journal of Colloid and Interface Science*, *439*, 76–87. https://doi.org/10.1016/j.jcis.2014.10.007

Jordan, V., Javornik, U., Plavec, J., Podgornik, A., & Rečnik, A. (2016). Self-assembly of multilevel branched rutile-type TiO 2 structures via oriented lateral and twin attachment. *Scientific Reports*, *6*. https://doi.org/10.1038/srep24216

Kavoosi, G., Derakhshan, M., Salehi, M., & Rahmati, L. (2018). Microencapsulation of zataria essential oil in agar, alginate and carrageenan. *Innovative Food Science and Emerging Technologies*, *45*, 418–425. https://doi.org/10.1016/j.ifset.2017.12.010

KAWANO, M., & KOYAMA, Y. (2024). Polymorphism and morphology of calcium carbonate minerals precipitated in the presence of low-molecular-weight organic acids with different numbers of carboxyl group at 40-80 °C. *Journal of Mineralogical and Petrological Sciences*, *119*(1), n/a. https://doi.org/10.2465/jmps.240216

Khosravi, F., & Montazer, M. (2023). Facile preparation of fatty acids/nano [Al(OH)3/Al2O3]/wool fabric introducing thermal energy management with multifunctional properties. *Journal of Energy Storage*, *64*. https://doi.org/10.1016/j.est.2023.107170

Kim, J. J., & Choi, J. W. (2021). Synthesis of large monolayer titania nanosheets through flux method. *Journal of Asian Ceramic Societies*. https://doi.org/10.1080/21870764.2021.1924979

Kim, S., Jeong, C., Cho, S., & Kim, S. B. (2019). Effects of thermal treatment on the physical properties of edible calcium alginate gel beads: Response surface methodological approach. *Foods*, *8*(11). https://doi.org/10.3390/foods8110578

Kosanović, C., Fermani, S., Falini, G., & Kralj, D. (2017). Crystallization of calcium carbonate in alginate and xanthan hydrogels. *Crystals*, *7*(12). https://doi.org/10.3390/cryst7120355

Kotoky, T., & Dolui, S. K. (2004). Synthesis and Characterisation of Polyvinyl alcohol (PVA)/Silica Hybrid Composites Derived Through the Sol-Gel Method in Aqueous Medium: Effect of Acid Content, Silica Content and Viscosity of PVA on the Dispersion Characteristics of Silica and the Physical Properties of the Composites. In *Journal of Sol-Gel Science and Technology* (Vol. 29).

Koysuren, O., Karaman, M., & Dinc, H. (2012). Preparation and characterization of polyvinyl borate/polyvinyl alcohol (PVB/PVA) blend nanofibers. *Journal of Applied Polymer Science*, *124*(4), 2736–2741. https://doi.org/10.1002/app.35035

Koysuren, O., & Koysuren, H. N. (2018). Photocatalytic activity of polyvinyl borate/titanium dioxide composites for UV light degradation of organic pollutants. *Journal of Macromolecular Science, Part A: Pure and Applied Chemistry*, *55*(5), 401–407. https://doi.org/10.1080/10601325.2018.1453259

Krautwurst, N., Nicoleau, L., Dietzsch, M., Lieberwirth, I., Labbez, C., Fernandez-Martinez, A., Van Driessche, A. E. S., Barton, B., Leukel, S., & Tremel, W. (2018). Two-Step Nucleation Process of Calcium Silicate Hydrate, the Nanobrick of Cement. *Chemistry of Materials*, *30*(9), 2895–2904. https://doi.org/10.1021/acs.chemmater.7b04245

Kusuktham, B., Prasertgul, J., & Srinun, P. (2014). Morphology and Property of Calcium Silicate Encapsulated with Alginate Beads. *Silicon*, *6*(3), 191–197. https://doi.org/10.1007/s12633-013-9173-z

Lambertini, L., Coccarelli, G., Toto, E., Santonicola, M. G., & Laurenzi, S. (2024). Poly(vinyl alcohol) gels cross-linked by boric acid for radiation protection of astronauts. *Acta Astronautica*, *221*, 142–154. https://doi.org/10.1016/j.actaastro.2024.05.020

Lee, J., Hong, J., Park, D. W., & Shim, S. E. (2010). Microencapsulation and characterization of poly(vinyl alcohol)-coated titanium dioxide particles for electrophoretic display. *Optical Materials*, *32*(4), 530–534. https://doi.org/10.1016/j.optmat.2009.11.008

Li, J., Jiang, Z., Wu, H., Long, L., Jiang, Y., & Zhang, L. (2009). Improving the recycling and storage stability of enzyme by encapsulation in mesoporous CaCO3-alginate composite gel. *Composites Science and Technology*, *69*(3–4), 539–544. https://doi.org/10.1016/j.compscitech.2008.11.017

Li, J., Wang, B., Ye, G., Xu, J., & Jiang, M. (2013). Study of synthesizing energy storage microcapsules in PVA spinning solution and thermal regulating fibers prepared by this solution. *Fibers and Polymers*, *14*(4), 537–541. https://doi.org/10.1007/s12221-013-0537-1

Li, L., Xu, X., Liu, L., Song, P., Cao, Q., Xu, Z., Fang, Z., & Wang, H. (2021). Water governs the mechanical properties of poly(vinyl alcohol). *Polymer*, *213*. https://doi.org/10.1016/j.polymer.2020.123330

Li, X., Shen, Q., Su, Y., Tian, F., Zhao, Y., & Wang, D. (2009a). Structure-function relationship of calcium alginate hydrogels: A novel crystal-forming engineering. *Crystal Growth and Design*, *9*(8), 3470–3476. https://doi.org/10.1021/cg900154v

Li, X., Shen, Q., Su, Y., Tian, F., Zhao, Y., & Wang, D. (2009b). Structure-function relationship of calcium alginate hydrogels: A novel crystal-forming engineering. *Crystal Growth and Design*, *9*(8), 3470–3476. https://doi.org/10.1021/cg900154v

Lian, Y., Wu, J., Zhou, D., Wang, H., Huang, D., & Huang, Y. (2011). Preparation and properties of alginate fibre. *Advanced Materials Research*, *335–336*, 419–422. https://doi.org/10.4028/www.scientific.net/AMR.335-336.419

Liu, Y., Sun, D., Askari, S., Patel, J., Macias-Montero, M., Mitra, S., Zhang, R., Lin, W. F., Mariotti, D., & Maguire, P. (2015). Enhanced Dispersion of TiO2 Nanoparticles in a TiO2/PEDOT:PSS Hybrid Nanocomposite via Plasma-Liquid Interactions. *Scientific Reports*, *5*. https://doi.org/10.1038/srep15765

Liu, Y., Zhao, J., Zhang, C., Ji, H., & Zhu, P. (2014). The flame retardancy, thermal properties, and degradation mechanism of zinc alginate films. *Journal of Macromolecular Science, Part B: Physics*, *53*(6), 1074–1089. https://doi.org/10.1080/00222348.2014.891169

Németh, B., Németh, Á. S., Tóth, J., Fodor-Kardos, A., Gyenis, J., & Feczkó, T. (2015). C. *Solar Energy Materials and Solar Cells*, *143*, 397–405. https://doi.org/10.1016/j.solmat.2015.07.029

Németh, B., Németh, Á. S., Ujhidy, A., Tóth, J., Trif, L., Gyenis, J., & Feczkó, T. (2018). Fully bio-originated latent heat storing calcium alginate microcapsules with high coconut oil loading. *Solar Energy*, *170*, 314–322. https://doi.org/10.1016/j.solener.2018.05.066

Olderay, M., Xie, M., Strand, B. L., Flaten, E. M., Sikorski, P., & Andreassen, J. P. (2009). Growth and nucleation of calcium carbonate vaterite crystals in presence of alginate. *Crystal Growth and Design*, *9*(12), 5176–5183. https://doi.org/10.1021/cg9005604

Park, K., Oh, Y., Panda, P. K., & Seo, J. (2022). Effects of an acidic catalyst on the barrier and water resistance properties of crosslinked poly (vinyl alcohol) and boric acid films. *Progress in Organic Coatings*, *173*. https://doi.org/10.1016/j.porgcoat.2022.107186

Pathak, T. S., Yun, J. H., Lee, J., & Paeng, K. J. (2010). Effect of calcium ion (cross-linker) concentration on porosity, surface morphology and thermal behavior of calcium alginates prepared from algae (Undaria pinnatifida). *Carbohydrate Polymers*, *81*(3), 633–639. https://doi.org/10.1016/j.carbpol.2010.03.025

Prosanov, I. Y., Abdulrahman, S. T., Thomas, S., Bulina, N. V., & Gerasimov, K. B. (2018). Complex of polyvinyl alcohol with boric acid: Structure and use. *Materials Today Communications*, *14*, 77–81. https://doi.org/10.1016/j.mtcomm.2017.12.012

Ramdhan, T., Ching, S. H., Prakash, S., & Bhandari, B. (2019). Time dependent gelling properties of cuboid alginate gels made by external gelation method: Effects of alginate-CaCl2 solution ratios and pH. *Food Hydrocolloids*, *90*, 232–240. https://doi.org/10.1016/j.foodhyd.2018.12.022

Rather, L. J., Shahid-ul-Islam, & Mohammad, F. (2015). Study on the application of Acacia nilotica natural dye to wool using fluorescence and FT-IR spectroscopy. *Fibers and Polymers*, *16*(7), 1497–1505. https://doi.org/10.1007/s12221-015-4879-8

Ren, J., Wang, S., Gao, C., Chen, X., Li, W., & Peng, F. (2015). TiO2-containing PVA/xylan composite films with enhanced mechanical properties, high hydrophobicity and UV shielding performance. *Cellulose*, *22*(1), 593–602. https://doi.org/10.1007/s10570-014-0482-1

Sakarkar, S., Muthukumaran, S., & Jegatheesan, V. (2020). Evaluation of polyvinyl alcohol (PVA) loading in the PVA/titanium dioxide (TiO2) thin film coating on polyvinylidene fluoride (PVDF) membrane for the removal of textile dyes. *Chemosphere*, *257*. https://doi.org/10.1016/j.chemosphere.2020.127144

Salimian, S., Montazer, M., Rashidi, A. S., Soleimani, N., & Bashiri Rezaie, A. (2021). PCM nanofibrous composites based on PEG/PVA incorporated by TiO2/Ag nanoparticles for thermal energy management. *Journal of Applied Polymer Science*, *138*(46). https://doi.org/10.1002/app.51357

Serrano-Aroca, Á., Iskandar, L., & Deb, S. (2018). Green synthetic routes to alginate-graphene oxide composite hydrogels with enhanced physical properties for bioengineering applications. *European Polymer Journal*, *103*, 198–206. https://doi.org/10.1016/j.eurpolymj.2018.04.015

Shawgi, N., Xi Li, S., Wang, S., Wang, Z., & Nan Nie, Y. (2017). Synthesis of nano particles and fiber-like shape boron carbide powder from ploy (vinyl alcohol) and boric acid. *Journal of Sol-Gel Science and Technology*, *82*(2), 450–457. https://doi.org/10.1007/s10971-017-4320-4

Sovova, S., Abalymov, A., Pekar, M., Skirtach, A. G., & Parakhonskiy, B. (2021). Calcium carbonate particles: synthesis, temperature and time influence on the size, shape, phase, and their impact on cell hydroxyapatite formation. *Journal of Materials Chemistry B*, *9*(39), 8308–8320. https://doi.org/10.1039/d1tb01072g

Sriamornsak, P., Nunthanid, J., Luangtana-anan, M., Weerapol, Y., & Puttipipatkhachorn, S. (2008). Alginate-based pellets prepared by extrusion/spheronization: Effect of the amount and type of sodium alginate and calcium salts. *European Journal of Pharmaceutics and Biopharmaceutics*, *69*(1), 274–284. https://doi.org/10.1016/j.ejpb.2007.09.012

Sun, L., Wang, J., Liang, J., & Li, G. (2020). Boric Acid Cross-linked 3D Polyvinyl Alcohol Gel Beads by NaOH-Titration Method as a Suitable Biomass Immobilization Matrix. *Journal of Polymers and the Environment*, *28*(2), 532–541. https://doi.org/10.1007/s10924-019-01610-z

Surkatti, R., van Loosdrecht, M. C. M., Hussein, I. A., & El-Naas, M. H. (2024). PVA-TiO2 Nanocomposite Hydrogel as Immobilization Carrier for Gas-to-Liquid Wastewater Treatment. *Nanomaterials*, *14*(3). https://doi.org/10.3390/nano14030249

Tian, Y., Liu, Y., Zhang, L., Hua, Q., Liu, L., Wang, B., & Tang, J. (2020). Preparation and characterization of gelatin-sodium alginate/paraffin phase change microcapsules. *Colloids and Surfaces A: Physicochemical and Engineering Aspects*, *586*. https://doi.org/10.1016/j.colsurfa.2019.124216

Tomar, P. A., Yadav, S. M., & Gupta, G. R. (2014). The thermal gravimetric studies for polymer samples of polyvinyl chloride (PVC) and polyvinyl alcohol (PVA) obtained by treatment with ionic liquid [bmim]Br. *Polymer Bulletin*, *71*(6), 1349–1358. https://doi.org/10.1007/s00289-014-1126-1

Vargas, P. O., Pereira, N. R., Guimarães, A. O., Waldman, W. R., & Pereira, V. R. (2018). Shrinkage and deformation during convective drying of calcium alginate. *LWT*, *97*, 213–222. https://doi.org/10.1016/j.lwt.2018.06.056

Velings, N. M., & Mestdagh, M. M. (n.d.). *Physico-Chemical Properties of Alginate Gel Beads*.

Wang, D., Chen, J., Wen, X., Fan, S., Zhu, C., Li, X., Fang, F., Yang, W., Fan, W., Zhang, D., & Hou, C. (2024). Self-assembled Chitosan/Polyvinyl alcohol hydrogel film incorporated with

TiO2 with excellent stability, mechanical and antibacterial properties for the preservation of chilled pork. *Food Packaging and Shelf Life*, *45*. https://doi.org/10.1016/j.fpsl.2024.101328

Wang, H., Yuan, M., Wu, J., Wan, P., & Liu, Q. (2022). Self-Healing Properties of Asphalt Concrete with Calcium Alginate Capsules Containing Different Healing Agents. *Materials*, *15*(16). https://doi.org/10.3390/ma15165555

Wang, W., Shen, L., Si, Y., MD Zahidul, I., Abdullaev, A., & Dong, Y. (2024). Calcium alginate film with excellent shape memory effect. *Pigment and Resin Technology*, *53*(2), 133–136. https://doi.org/10.1108/PRT-03-2022-0034

Wei, Q., & Yang, D. (2023). A self-healing polyvinyl alcohol-based composite with high thermal conductivity and excellent mechanical properties. *Composites Communications*, *39*. https://doi.org/10.1016/j.coco.2023.101561

Wen, G., Naik, R., Cookson, P. G., Smith, S. V., Liu, X., & Wang, X. G. (2010). Wool powders used as sorbents to remove Co2+ ions from aqueous solution. *Powder Technology*, *197*(3), 235–240. https://doi.org/10.1016/j.powtec.2009.09.021

Wojciechowska, E., Wl⁄ochowicz, A., & Wesel⁄ucha-Birczyn´skabirczyn´ska, A. (n.d.). *Application of Fourier-transform infrared and Raman spectroscopy to study degradation of the wool fiber keratin*. www.elsevier.nl/locate/molstruc

Wu, C., Fan, W., Gelinsky, M., Xiao, Y., Chang, J., Friis, T., & Cuniberti, G. (2011). In situ preparation and protein delivery of silicate-alginate composite microspheres with core-shell structure. *Journal of the Royal Society Interface*, *8*(65), 1804–1814. https://doi.org/10.1098/rsif.2011.0201

Xie, M., Olderøy, M., Andreassen, J. P., Selbach, S. M., Strand, B. L., & Sikorski, P. (2010). Alginate-controlled formation of nanoscale calcium carbonate and hydroxyapatite mineral phase within hydrogel networks. *Acta Biomaterialia*, *6*(9), 3665–3675. https://doi.org/10.1016/j.actbio.2010.03.034

Xu, W., Cui, W., Li, W., & Guo, W. (2004). Development and characterizations of super-fine wool powder. *Powder Technology*, *140*(1–2), 136–140. https://doi.org/10.1016/j.powtec.2003.12.010

Xu, W., Ke, G., Wu, J., & Wang, X. (2006). Modification of wool fiber using steam explosion. *European Polymer Journal*, *42*(9), 2168–2173. https://doi.org/10.1016/j.eurpolymj.2006.03.026

Yu, S., Wang, X., & Wu, D. (2014). Self-assembly synthesis of microencapsulated n -eicosane phase-change materials with crystalline-phase-controllable calcium carbonate shell. *Energy and Fuels*, *28*(5), 3519–3529. https://doi.org/10.1021/ef5005539

Yuan, L., Ren, L., Tian, X., Huang, Z., Xiao, Y., Wei, S., & Wang, Z. (2016). Investigation on polyvinyl-alcohol-based rapidly gelling hydrogels for containment of hazardous chemicals. *RSC Advances*, *6*(75), 71425–71430. https://doi.org/10.1039/c6ra14032g

Zain, N. A. M., Suhaimi, M. S., & Idris, A. (2011). Development and modification of PVA-alginate as a suitable immobilization matrix. *Process Biochemistry*, *46*(11), 2122–2129. https://doi.org/10.1016/j.procbio.2011.08.010

Zhang, J., Ji, Q., Shen, X., Xia, Y., Tan, L., & Kong, Q. (2011). Pyrolysis products and thermal degradation mechanism of intrinsically flame-retardant calcium alginate fibre. *Polymer Degradation and Stability*, *96*(5), 936–942. https://doi.org/10.1016/j.polymdegradstab.2011.01.029

Zhao, D., Zhuo, R. X., & Cheng, S. X. (2012). Alginate modified nanostructured calcium carbonate with enhanced delivery efficiency for gene and drug delivery. *Molecular BioSystems*, *8*(3), 753–759. https://doi.org/10.1039/c1mb05337j

Zhou, L., Shi, F., Liu, G., Ye, J. P., Han, P. S., & Zhang, G. (2021). Fabrication and characterization of in situ cross-linked electrospun Poly(vinyl alcohol)/phase change material nanofibers. *Solar Energy*, *213*, 339–349. https://doi.org/10.1016/j.solener.2020.11.039

ANNEX I

ALGINATE PROJECT

Fabrication System

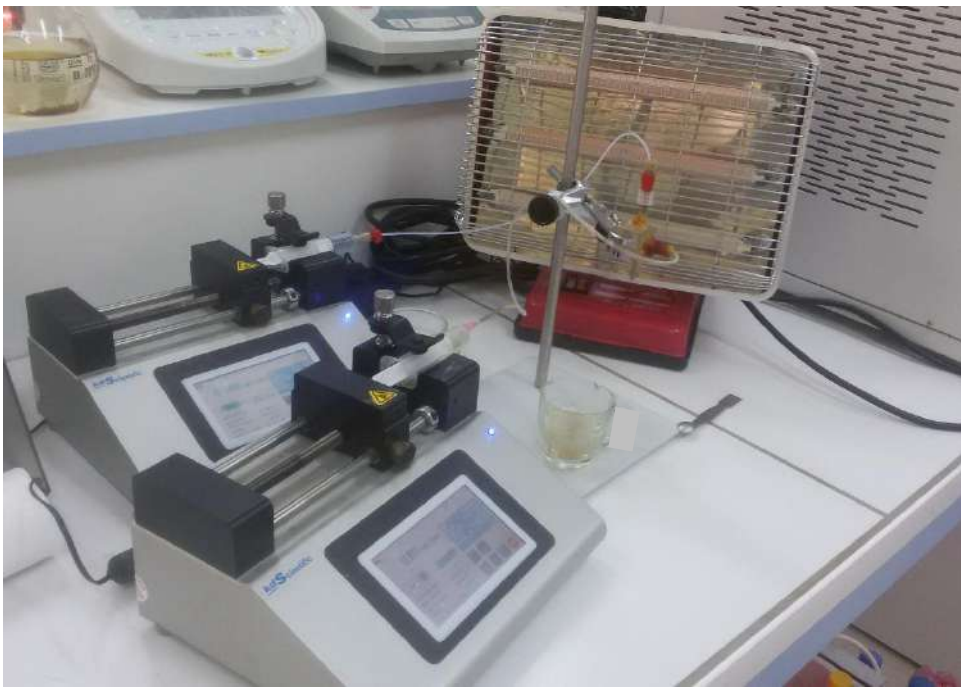

Microfluidic System

Coaxial device

Optical Microscopy

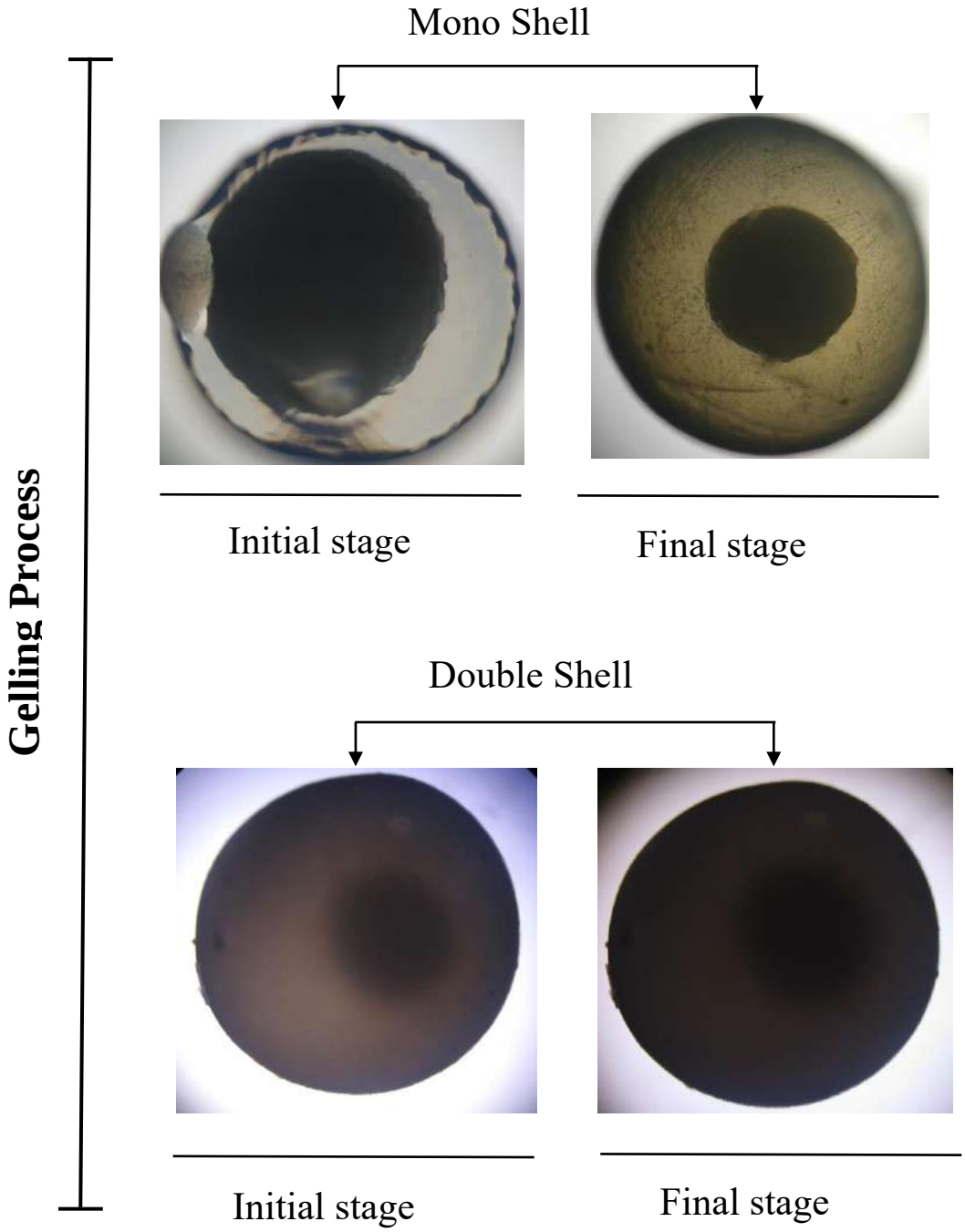

Photograph

Gelling process

Single Shell

Double Shell

Hardening process

Hydrogel

Consolidated particles

Thermal Endurance of Microcapsules

Heated at 100 ℃ for 10 min

In the beginning

In the END

Heated at 150 ℃ for 10 min

Exterior Changes

Cross section

Heated at 200 ℃ for 10 min

Exterior Changes

Cross section

Heated at 250 ℃ for 10 min

Exterior Changes

Cross section

ANNEX II

PVA PROJECT

Photograph

Drying Process

Hydrogel

Consolidated Particles

Prototypes

Matrix PVA Gypsum Matrix Modified PVA

Outsaid Data Acquisition

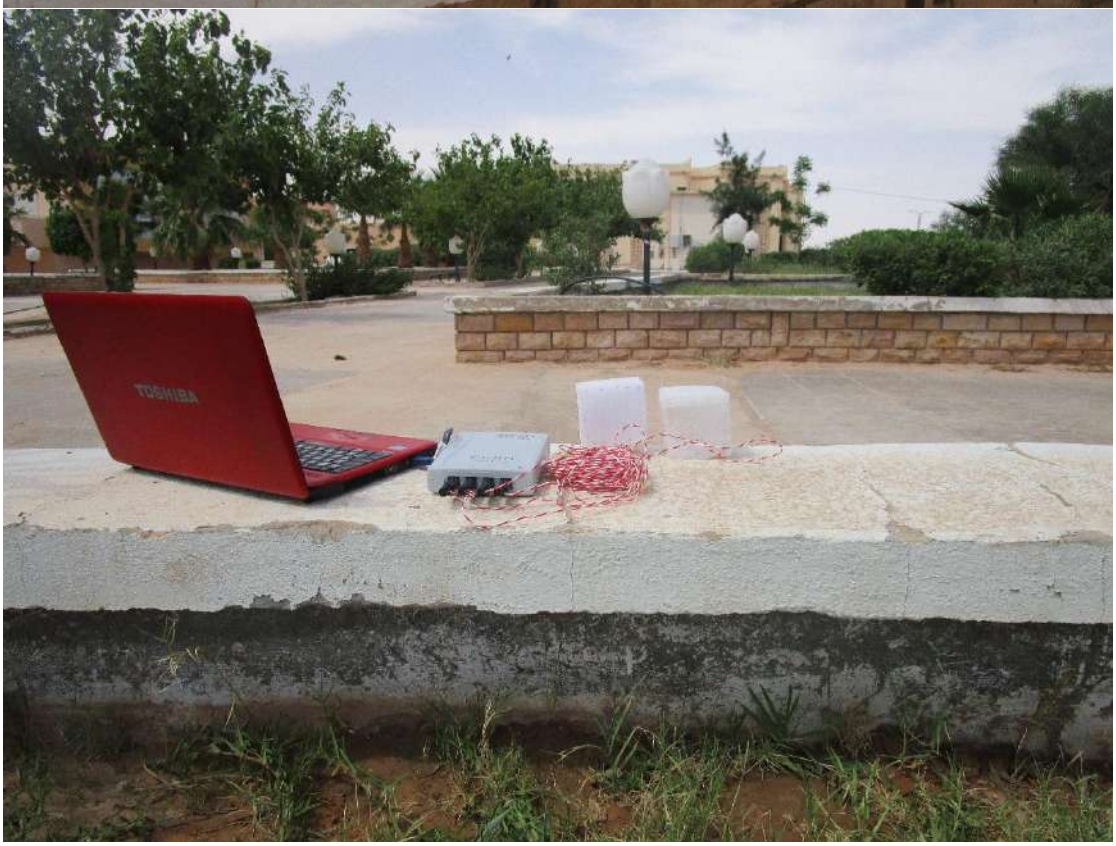

ANNEX III

WOOL PROJECT

Into Laboratory

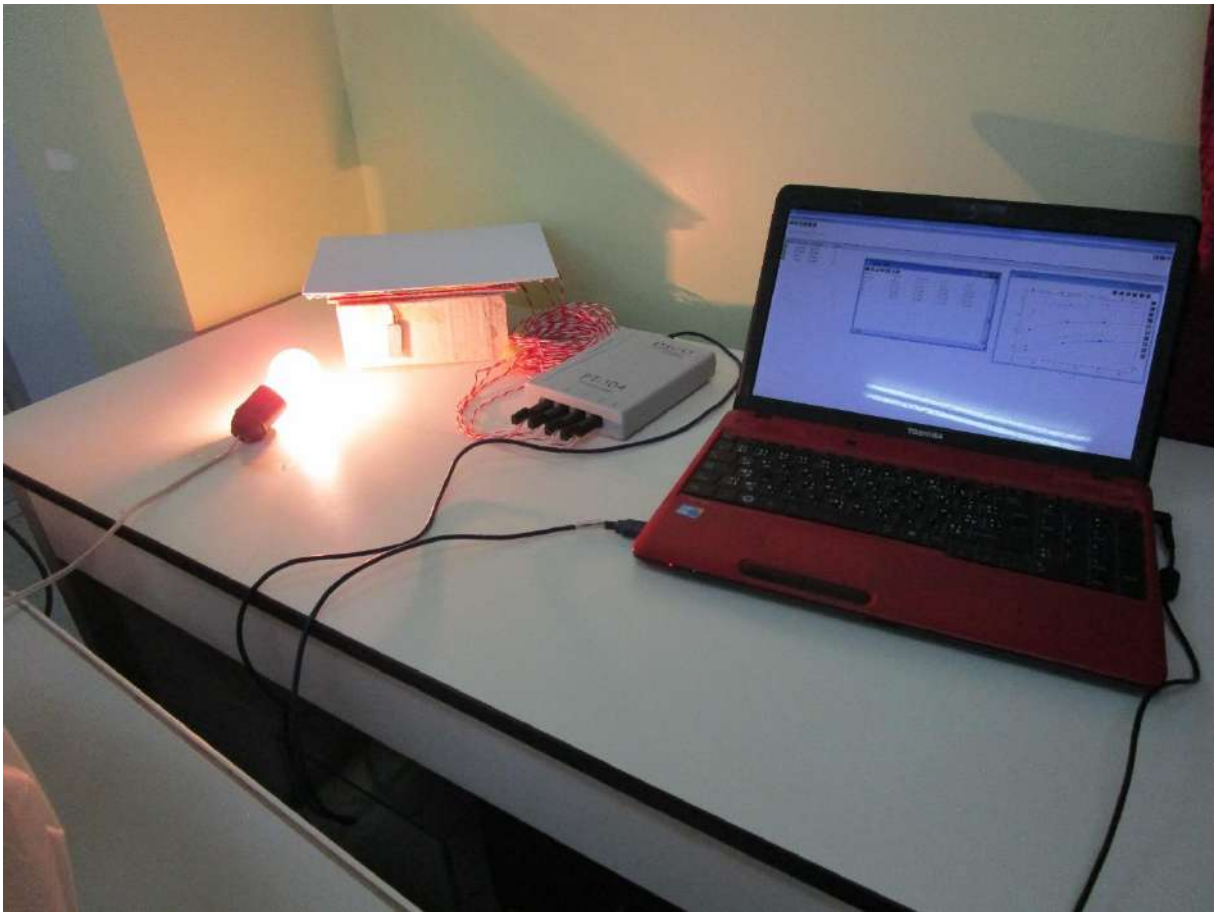

XRD Wool Powder Data

Data after 1 day immersion

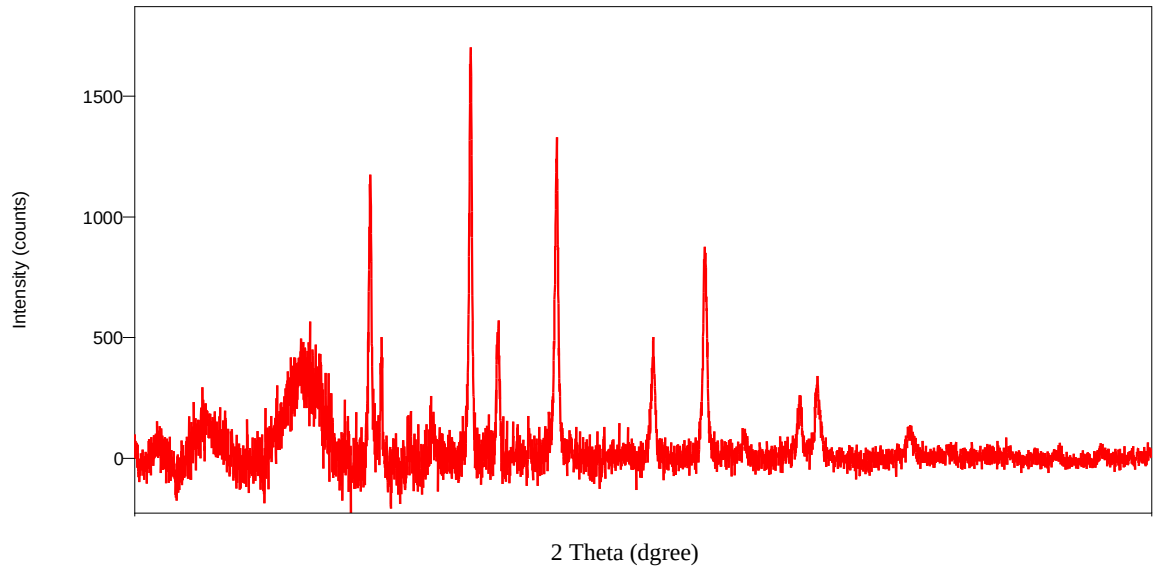

Data after 24 days immersion

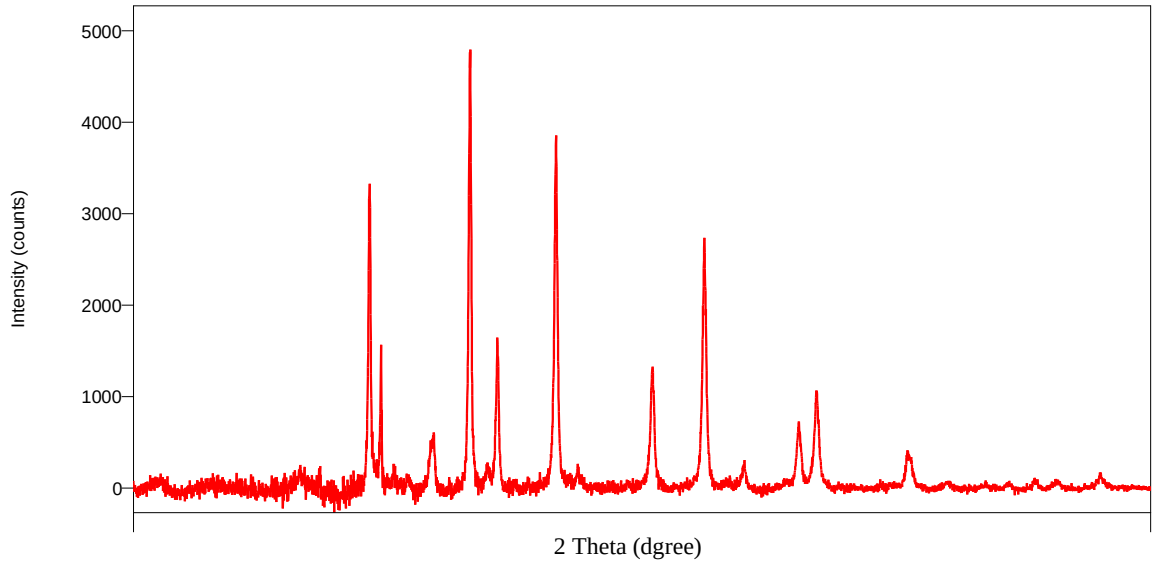

RESUME

On a réussi à produire des microparticules thermorégulatrices et on a choisi trois catégories de polymères, l'alginate, l'alcool polyvinylique et la poudre de laine de mouton, en se basant sur leur provenance naturelle et leur comportement non toxique. Pour évaluer la performance morphologique dans la préservation du matériau face aux changements de phase, diverses techniques ont été employées. La méthode d'encapsulation par le système microfluidique est utilisée pour fabriquer des capsules mononucléaires d'alginate-PCM. La polymérisation par une émulsion traditionnelle est employée pour générer des microsphères d'alginate/PCM et de PVA/PCM. La technique de stabilisation de forme est employée pour générer une matrice homogène entre laine-PVA-alginate/PCM et laine-alginate/PCM.
On obtient une amélioration de la stabilité thermique en incorporant des matériaux extrêmement stables.
Mots clés : PCM, Encapsulation, Stabilité thermiques.